

# Topics in Multiscale Modeling of Metals and Metallic Alloys

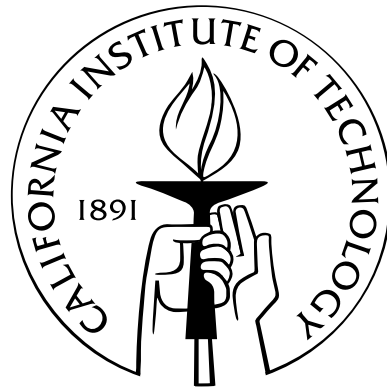
Thesis by

Gabriela N. Venturini

In Partial Fulfillment of the Requirements

for the Degree of

Doctor of Philosophy



California Institute of Technology

Pasadena, California

2011

(Defended October 28, 2010)

© 2011

Gabriela N. Venturini

All Rights Reserved

To the Universidad de Buenos Aires faculty members,  
who taught me how to think



# Acknowledgements

## Thanks so much!

- To my advisor –Professor Michael Ortiz– for pushing me out of my comfort zone (again and again),
- Marta and Lydia for their unconditional support,
- Professor Nadia Lapusta, because your faith in me will continue to expand my horizon.
- Jaime Marian for the things you taught me,
- To Roseanna, for all those cups of coffee, for being my friend and my colleague,
- Vanessa, for the time we spent together,
- Bo Li for all the help over these years,
- my office mates –Luigi and Celia– for the little talks and discussions,
- Luigi (again) for helping me achieve my childhood dream of running a marathon.
- To Lisa for opening her house when I needed a place to stay,
- my parents for their sacrifices,
- my sisters –Ludmila and Maia– for keeping me grounded to my roots,
- Julián and Analía, because your friendship is always a home to come back to,
- Ana (again) for becoming my third sister.
- To Marcial, for the years of happiness and the things I learned.



# Contents

<b>Acknowledgements</b>	<b>v</b>
<b>1 Introduction</b>	<b>1</b>
<b>2 Finite Temperature Atomistic-to-Continuum Reduction through Langevin Dynamics</b>	<b>5</b>
2.1 Theory . . . . .	6
2.1.1 Zero Temperature Quasicontinuum . . . . .	9
2.1.2 The Dynamical Theory . . . . .	11
2.1.3 The Quasiharmonic Approximation in the QC Framework . . . . .	14
2.2 Numerical Results . . . . .	19
2.2.1 Aluminum Results . . . . .	19
2.2.2 Tantalum Results . . . . .	27
2.3 Discussion . . . . .	30
2.4 Appendix I: Derivation of the Free Energy Expression . . . . .	31
2.5 Appendix II: The Embedded Atom Method . . . . .	33
2.5.1 Force Matching Method - Aluminum and Tantalum Potentials . . . . .	34
<b>3 Equilibrium Mean-Field Framework for Alloys at Finite Temperature</b>	<b>39</b>
3.1 General Framework . . . . .	40
3.2 Building a Suitable Probability Distribution . . . . .	42
3.3 Thermodynamic Potentials . . . . .	46

3.3.1	Entropy . . . . .	47
3.3.2	Internal Energy . . . . .	48
3.3.3	Closed Systems and the Helmholtz Free Energy . . . . .	49
3.3.4	Open Systems and the Grand Canonical Potential . . . . .	50
3.4	Interatomic Interactions . . . . .	51
3.5	Systems in Thermal Equilibrium . . . . .	53
3.6	Equilibrium Mean-Field Framework Validation . . . . .	55
3.6.1	Nickel-Palladium Lattice Parameter . . . . .	55
3.6.2	Copper-Nickel Thermal Expansion . . . . .	56
3.6.3	Copper-Nickel Elastic Constants . . . . .	58
3.6.4	Surface Segregation . . . . .	63
3.7	Discussion . . . . .	68
3.8	Appendix I: Numerical Quadrature for Gaussian Functions . . . . .	69
3.9	Appendix II: Johnson's EAM Potentials . . . . .	71
<b>4</b>	<b>Variational Coupling for Non-Equilibrium Mechano-Chemical Problems</b>	<b>73</b>
4.1	Balance Laws . . . . .	74
4.2	Rate Problem . . . . .	75
4.3	Incremental Formulation . . . . .	79
4.4	Numerical Results . . . . .	83
4.5	Discussion . . . . .	85
<b>5</b>	<b>Replica Time Integrators</b>	<b>89</b>
5.1	Introduction . . . . .	90
5.2	One-Dimensional Replica Time Integrators . . . . .	92
5.2.1	A Transmitting Finite-Element Scheme . . . . .	92
5.2.2	Phase-Error Analysis . . . . .	94
5.2.3	Replica Reinterpretation . . . . .	99

5.2.4	Complexity of One-Dimensional RTIs . . . . .	101
5.2.5	Numerical Examples . . . . .	102
5.2.6	A Benchmark Test . . . . .	105
5.3	Extension to Multiple Dimensions . . . . .	105
5.3.1	A Transmitting Time-Integration Scheme . . . . .	108
5.3.2	Phase-Error Analysis . . . . .	110
5.3.3	Replica Reinterpretation . . . . .	114
5.3.4	Complexity of Multi-Dimensional RTIs . . . . .	115
5.4	Finite-Element Reformulation . . . . .	115
5.5	Numerical Tests . . . . .	117
5.5.1	Hookean Material . . . . .	117
5.5.2	Neo-Hookean Material . . . . .	121
5.6	Discussion . . . . .	124
<b>6</b>	<b>Concluding Remarks and Future Work</b>	<b>127</b>
	<b>Bibliography</b>	<b>133</b>



# List of Figures

2.1	Thermal expansion behavior of two finite Al crystals containing 17969 (dimensions: $16_0 \times 16_0 \times 16a_0$ ) and 137313 ( $32a_0 \times 32a_0 \times 32a_0$ ) atoms. The error bars (very small for the $32_0 \times 32_0 \times 32a_0$ system) are associated with volume fluctuations at equilibrium.	20
2.2	Normalized equilibrium volume $V_0$ as a function of the normalized number of representative atoms. Volumes are calculated via conjugate-gradient energy minimizations and are normalized to the relaxed volumes of the atomistic systems. . . . .	21
2.3	Time evolution of the system volume at five different temperatures for the ( $N=137313$ , $N_h=729$ , $r_c=4$ ) system. Measurements start only after steady state has been reached (25 ps). . . . .	22
2.4	Thermal expansion behavior of a $16a_0 \times 16a_0 \times 16a_0$ Al system containing 17989 lattice sites. Four mesh and three cluster sizes were considered. . . . .	22
2.5	Thermal expansion behavior for a $32a_0 \times 32a_0 \times 32a_0$ Al system containing 137313 lattice sites. Four mesh and three cluster sizes were considered. . . . .	23
2.6	Thermal expansion coefficient as a function of the approximate nodal weights. The dashed line is a least-squares fit to the data corresponding to $r_c = 4$ . . . . .	25
2.7	(Left) Free energy vs normalized lattice parameter for fully atomistic Al systems. The minima of the fitted 2 <sup>nd</sup> -order polynomials (marked with a black 'x') are the equilibrium lattice parameter at each temperature, normalized to the bulk $a_0$ of 4.032 Å. (Right) Temperature dependence of the equilibrium lattice parameter. The derivative of the linear fit to the data gives the thermal expansion coefficient $\alpha$ . . . . .	36

2.8	Thermal expansion behavior of Ta. Solid dots correspond to experimental data given by Touloukian et al. [44]. Inverted triangles are periodic MD calculations performed by Li et al. [50]. Solid triangles and open dots correspond to QC dynamic simulations for finite $20a_0 \times 20a_0 \times 20a_0$ and $30a_0 \times 30a_0 \times 30a_0$ systems. Finally, solid lines are third-degree polynomial fits to the data. . . . .	37
2.9	Thermal expansion behavior of the $20a_0 \times 20a_0 \times 20a_0$ system (17261 lattice sites). Three meshes and three cluster sizes were considered. All meshes show negative thermal expansion until approximately 500K, at which point the lattice parameter becomes independent of $T$ ( $\alpha = 0$ ). We recall that $n'_h = N/N_h$ is the <i>effective</i> nodal weight. . .	37
2.10	Thermal expansion behavior of the $30a_0 \times 30a_0 \times 30a_0$ system (56791 lattice sites). Four meshes and three cluster sizes were considered. All meshes show negative thermal expansion until approximately 1000K, after which the lattice parameter becomes independent of $T$ ( $\alpha = 0$ ). . . . .	38
3.1	NiPd lattice parameter versus Pd atomic percentage at two different temperatures. Experimental [70] single crystal results are included for comparison purposes. . . . .	56
3.2	Numerical and experimental [71] results of linear thermal expansion in two single-crystal CuNi alloys as a function of temperature. Color arrows indicate the Debye temperature of the pure alloy components. . . . .	57
3.3	Numerical and experimental results (A: [72], B: [71]) of linear thermal expansion in single crystal copper and nickel as a function of temperature. $T_m$ and $T_D$ denote the melting point and the <i>Debye</i> temperature, respectively. . . . .	58
3.4	Numerical and experimental results [72] of elastic constants in single crystal CuNi alloys as a function of Cu concentration. . . . .	64
3.5	Scheme of the sample used to simulate surface segregation phenomena. . . . .	66
3.6	Numerical and experimental results (A: [80], B: [78], C: [79]) of surface segregation in CuNi alloys for different surface orientations and temperatures. . . . .	67

3.7	Numerical and experimental results (A: [81], B: [82]) of segregation profiles in AgAu alloys for different surface orientations, Ag bulk compositions and temperatures. . . .	68
4.1	Scheme of the sample used to simulate: (a) rigid body diffusion, and (b) semi-rigid body diffusion. The orientation of the system is such that z- and [0 0 1] directions coincide. . . . .	85
4.2	Time evolution of the average layer concentration within a rigid solid. . . . .	86
4.3	Time evolution of the average layer concentration within a semi-rigid solid subjected to uniaxial tensile strain in the z-direction. . . . .	86
5.1	Space-time grid of size $(\Delta x, \Delta t)$ that coarsens at $x = 0$ to a space-time grid of size $(2\Delta x, \Delta t)$ . Elementary signals that must be supported by the algorithm (signals are 1 at black dots, 0 elsewhere). . . . .	93
5.2	Finite-difference stencils that define a finite-difference scheme that transmits elementary signals across the interface in both directions. . . . .	93
5.3	The two states of the solution of the transmitting finite-difference scheme (5.2-5.4) run at the CFL limit (5.5) for an incoming phonon unresolved by the coarse spatial mesh. . . . .	98
5.4	Magnitude of the reflected wave amplitude $ A_R^+ $ , or reflection coefficient, vs. the ratio $n$ of coarse to fine grid size for three different number of points per wavelength, $L/h = L/\Delta x = 2\pi/\Delta x/k^-$ , and Courant numbers $C = 0.05$ (squares), $0.75$ (circles) and $0.99$ (triangles). Lines without symbols correspond to central differences. . . . .	99
5.5	Replica re-interpretation of the time-integration scheme shown in Fig. 5.2. The schematic shows the interface between the fine and coarse spatial grids and the replica ensemble (color-coded) used to represent solutions over the coarse spatial grid. . . . .	100
5.6	Schematic of master-slave relation of overlap implementation of RTIs. The up-down arrows point from master grid points to slave grid points. . . . .	101

- 5.7 One-dimensional grid consisting of two regions of equal length, a fine grid on the left of the interface and a four-fold coarser grid on the right. Four replicas of the coarse grid are used in the solution. a) Snapshot of step wave after the transmission from the fine to the coarse grid. b) Snapshot of step wave after transmission from the coarse to the fine grid. . . . . 102
- 5.8 One-dimensional grid consisting of two regions of equal length, a fine grid on the left of the interface and a four-fold coarser grid on the right. Four replicas of the coarse grid are used in the solution. a) Snapshot of arbitrary wave after the transmission from the fine to the coarse grid. b) Snapshot of arbitrary wave after transmission from the coarse to the fine grid. . . . . 103
- 5.9 One-dimensional grid consisting of two regions of equal length, a fine grid on the left of the interface and a hundred-fold coarser grid on the right. A hundred replicas of the coarse grid are used in the solution. Histograms of signal values on all points of the fine and coarse grids after transmission of the signal transmission across the interface. a) Normally distributed random signal. b) Uniformly distributed random signal. . . . 104
- 5.10 One-dimensional benchmark test of Belytschko et al. [91], consisting of a fine grid on the left of the domain attached to a two-fold coarser grid on the right and subjected to harmonic excitation at the left boundary. a) RTI solution. b) and c) Individual replica components of the RTI solution. . . . . 106
- 5.11 One-dimensional benchmark test of Belytschko et al. [91], consisting of a fine grid on the left of the domain attached to a two-fold coarser grid on the right and subjected to harmonic excitation at the left boundary. Central differences solution. . . . . 107
- 5.12 Finite-difference stencils defining a finite-difference scheme that transmits elementary signals across a mesh interface in both directions. Coarsening ratio  $n = 2$ . . . . . 110
- 5.13 Magnitude of the reflected wave amplitude  $|A_R^+|$ , or reflection coefficient, vs. the ratio  $n$  of coarse to fine grid size for three number of points per wavelength,  $L/h = L/\Delta x = 2\pi/\Delta x/k^-$ , and Courant numbers  $C = 0.05$  (squares),  $0.75$  (circles) and  $0.99$  (triangles). 113

5.14	Schematics of the RTI implementation using finite elements. $h_{fine}$ and $h_R$ refer to the characteristic element size for fine and coarse meshes, respectively ( $n = 2$ for this particular case). . . . .	116
5.15	Finite element implementation of RTI ( $n = 2$ for this particular case). . . . .	117
5.16	Linear elastic step wave propagating through the thickness of an infinite linear-elastic plate. On left, finite-element mesh with transverse mesh-size doubling interface. On right, contour plot of z-displacements as a function of time. . . . .	118
5.17	Step wave through linear-elastic plate, normal fine-coarse coupling. RTI and uniform-fine scheme (UFS) solutions. a) Material point trajectories through several reverberations of the wave. b) Corresponding time evolution of the total energy. . . . .	119
5.18	Linear elastic step wave propagating through the thickness of an infinite linear-elastic plate. On left, finite-element mesh with longitudinal mesh-size doubling interface. On right, contour plot of z-displacements as a function of time. . . . .	120
5.19	Step wave through linear-elastic plate, longitudinal fine-coarse coupling. RTI and uniform-fine scheme (UFS) solutions. a) Material point trajectories through several reverberations of the wave. b) Corresponding time evolution of the total energy. . . .	121
5.20	Nonlinear elastic step wave propagating through the thickness of an infinite compressible neo-Hookean elastic plate. Initial configuration and three subsequent deformed configurations. Displacements shown to scale. a) Transverse mesh interface. b) Longitudinal mesh interface. . . . .	122
5.21	Step wave through compressible neo-Hookean elastic plate, normal fine-coarse coupling. RTI and uniform-fine scheme (UFS) solutions. a) Material point trajectories through several reverberations of the wave. b) Corresponding time evolution of the total energy. 123	
5.22	Step wave through compressible neo-Hookean elastic plate, longitudinal fine-coarse coupling. RTI and uniform-fine scheme (UFS) solutions. a) Material point trajectories through several reverberations of the wave. b) Corresponding time evolution of the total energy. . . . .	123

6.1 Numerical and experimental results (A: [124], B: [125]) of equilibrium vacancy concentration in copper as a function of temperature. . . . . 131

# List of Tables

2.1	Time step and characteristic damping time for perfect crystal Al and Ta. . . . .	14
2.2	Coefficients of the third degree polynomials $V(T)/V_0 = aT^3 + bT^2 + cT + d$ plotted in Fig. 2.1. From eq. (2.41), $\alpha(T) = \frac{1}{3}(3aT^2 + 2bT + c)$ . Since at $T = 0$ , $V(0) = V_0$ ; $d$ is set equal to one. . . . .	21
2.3	Compilation of thermal expansion coefficients $\alpha$ (in $K^{-1}$ ) for the $16a_0 \times 16a_0 \times 16a_0$ and the $32a_0 \times 32a_0 \times 32a_0$ Al systems –17989 and 137313 lattice sites, respectively. Results were obtained from dynamic simulations. Atomistic systems yield $\alpha = 1.72 \times 10^{-5}$ and $1.70 \times 10^{-5} K^{-1}$ , respectively. . . . .	24
2.4	Thermal expansion coefficients (in $K^{-1}$ ) calculated within the quasiharmonic approximation for the systems considered in Table 2.3. ‘-’ symbols indicate that the diagonalization of the corresponding dynamical matrices was beyond our computational capabilities. . . . .	27
2.5	Coefficients of third degree polynomial $[a(T)/a(298 K) - 1] = aT^3 + bT^2 + cT + d$ fits to dynamic QC simulations plotted in Fig. 2.8. The linear thermal expansion coefficient is calculated as: $\alpha(T) = 3aT^2 + 2bT + c$ . . . . .	28
3.1	Elastic Constants calculation . . . . .	63
3.2	EAM parameters . . . . .	72
5.1	Step wave through linear-elastic plate, normal fine-coarse coupling. Summary of mesh sizes and time steps used in RTI and uniform-fine scheme (UFS) calculations. . . . .	118



# Chapter 1

## Introduction

In a number of areas of application, the behavior of systems depends sensitively on properties that pertain to the atomistic scale, i. e., the angstrom and femtosecond scales. Specifically, atomistic details are important where material response is highly non-linear, e. g., near crack tips and other stress concentrators, or around atomic scale defects such as dislocations and grain boundaries [1]. However, generally the behaviors of interest are macroscopic and are characterized by slow evolution on the scale of meters and years. A case in point is degradation in nuclear reactor materials, which stems from a combination of heat, irradiation, stress and corrosion exposure for extended periods of time (20+ years), see [2] and references therein. This broad disparity of length and time scales places extraordinary challenges in computational material science.

Molecular Dynamics (MD) and Monte Carlo methods (MC) are powerful techniques to study deformation and diffusion mechanisms in a system of particles, but they are limited to time windows of microseconds at best [3]. No methods are available to study phenomena on time scales of the order of seconds to years while retaining an atomic description of the material.

The overarching objective of this dissertation is to address the problem of multiple space and time scales in atomistic systems undergoing slow macroscopic evolution while retaining full atomistic detail. The main limitations of existing atomistic –or atomistic-to-continuum models– and our approach to overcome them may be summarized as follows:

- I. The issue of accounting for finite temperature in coarse grained systems has not been solved entirely. For finite temperature systems at equilibrium, constructing an effective free energy

in terms of a reduced set of atomic degrees of freedom is still an open area of research. In particular, the thermal vibrations of the missing degrees of freedom need to be accounted for. This is specially important if the aim of the simulation is to determine the dynamic properties of a system, or to allow the transmission of dynamic information between regions of different spatial discretization. To this end, in Chapter 2 we introduce a framework to simulate (spatially) coarse dynamic systems using the Quasicontinuum method (QC). The equations of motion are strictly derived from dissipative Lagrangian mechanics, which provides a classical Langevin implementation where the characteristic time is governed by the vibrations of the finest length scale in the computational cell. In order to assess the framework's ability to transmit information across scales, we study the phonon impoverish spectra in coarse regions and the resulting underestimation of thermal equilibrium properties.

II. Atomistic simulations have been employed for the past thirty years to determine structural and thermodynamic (equilibrium) properties of solids and their defects over a wide range of temperatures and pressures. The traditional Monte Carlo (MC) and Molecular Dynamics (MD) methods, while ideally suited to these calculations, require appreciable computational resources in order to calculate the long-time averages from which properties are obtained. In order to permit a reasonably quick, but accurate determination of the equilibrium properties of interest, in Chapter 3 we present an extension of the *maximum entropy* method of Kulkarni et al. [4] to build effective alloy potentials while avoiding the treatment of all the system's atomic degrees of freedom. By restricting ourselves to the study of multi-species crystalline materials at finite temperature, the idea is to account for the energy contained in thermal oscillations and for the contribution of different components without the knowledge of the instantaneous velocity of such vibrations or the specific identity of each atom within the lattice. We assess the validity of the model by testing its ability to reproduce experimental measurements.

III. Based upon the effective potentials derived in Chapter 3, in Chapter 4 we present a numerical framework capable of following the time evolution of atomistic systems over time windows currently beyond the scope of traditional atomistic methods such as Molecular Dynamics (MD)

or Monte Carlo (MC). This is accomplished while retaining the underlying atomistic description of the material. Following the work by Yang et al. [5], we formulate a discrete variational setting in which the simulation of time-dependent phenomena is reduced to a sequence of incremental problems, each characterized by a variational principle. In this fashion we are able to study the interplay between deformation and diffusion using time steps or strain rates that are orders of magnitude larger or smaller than their MD|MC counterparts. In addition, the variational structure determines the coupling between mechanics and diffusion in a unique way, without additional constitutive equations to relate the chemical potential of the diffusing impurity with its concentration or the state of stress of the system.

IV. Smooth information transfer across interfaces of nonuniform spatial resolution presents a number of open questions. Typically, short wavelength waves generated in atomistic regions and representing the thermal motion of the atoms cannot be transmitted into coarse grained regions and are reflected back. The result is a build-up of energy in the atomically refined region, which amounts to a localized, non-physical heating of the crystal. This unphysical reflection of waves due to mesh inhomogeneities is the main problem to solve in order to properly account for the dynamics of coarse-grained systems. In Chapter 5 we address this problem by formulating time-integration schemes capable of transmitting waves across mesh interfaces. To this end, we formulate a new class of *Replica Time Integrators* (RTIs) that allows for the two-way transmission of thermal phonons across mesh interfaces. This two-way transmission is accomplished by representing the state of the coarse region by a collection of identical copies or *replicas* of itself. Each replica runs at its own slow time step and is out-of-phase with respect to the others by one fast time step. Then, each replica is capable of absorbing from the fine region the elementary signal that is in phase with the replica. Conversely, each replica is capable of supporting –and transmitting to the fine region– an elementary signal of a certain phase. Since fine and coarse regions evolve asynchronously in time, RTIs permit both spatial and temporal coarse graining of the system of interest. Using a combination of phase-error analysis and numerical testing we find that RTIs are convergent, and allow step waves and

thermal phonons to cross mesh interfaces in *both* directions losslessly. In addition, the replica ensemble structure of RTIs renders them ideally suited for parallel computing. In dimension  $d$  RTIs afford an  $O(n^d)$  speed-up factor in sequential mode, and  $O(n^{d+1})$  in parallel, over regions that are coarsened  $n$ -fold.

In closing, the range and limitations of the present schemes and the outlook for future work are discussed in Chapter 6.

## Chapter 2

# Finite Temperature Atomistic-to-Continuum Reduction through Langevin Dynamics

The philosophy behind recent multiscale methods is to start with a system entirely modeled at the atomic scale, i. e., described by a potential energy that depends on the position of all the atoms in the system, and to construct an effective potential energy that depends on a reduced set of atomic positions. The system is then often said coarse grained.

The issue of accounting for finite temperature in coarse grained systems has not been solved entirely. Two types of simulations may be performed: finite temperature systems at equilibrium or dynamic systems driven out-of-equilibrium. In the first case, constructing an effective free energy in terms of the above reduced set of atomic degrees of freedom is still an open area of research. In the second case, the unphysical reflection of waves due to mesh inhomogeneities is the main problem to solve in order to properly account for the dynamics of coarse-grained systems [6]. Said in practical words, short wavelength waves generated in atomistic regions and representing the thermal motion of the atoms cannot be transmitted into regions of low representative atom density and are reflected back. The result is a build-up of energy in the atomically refined region, which amounts to a localized, non-physical heating of the crystal.

Here we develop an approach similar to that of Qu et al. [7] within the Quasicontinuum (QC) framework [8, 9]. We take advantage of the seamless bridging of length scales furnished by the QC formulation to write the equations of motion in terms of dissipative Lagrangian mechanics,

with a viscous term that expends the thermal energy introduced by a Langevin thermostat through a suitable random force at the nodal level. Unlike Qu et al., however, the equations of motion have the same form across the entire domain. In this fashion, phonons not transmitted across mesh boundaries are dampened in accordance with the imposed thermostat so as to sample stable canonical ensemble trajectories. Our method is fully anharmonic and can be used to study non-equilibrium, thermally-activated processes directly. However, impoverished phonon spectra in coarse regions result in an underestimation of thermal properties such as thermal expansion, specific heat capacities, etc. It is important to understand and quantify this loss of entropy stemming from length scale inhomogeneities.

Quantifying the loss of information due to coarsening is generally done in terms of reflection coefficients [10,11]. A more direct method computes entropic losses via the Debye-Grüneisen model (quasiharmonic approximation) [12–14] or some other thermodynamic integration method [15]. We will use the thermal expansion coefficient  $\alpha$  as a metric to measure entropy loss, as all frequencies participate in thermal expansion, especially those most sensitive to volume changes. Next we study the thermal expansion behavior of two metallic systems, one face-centered cubic (fcc) —aluminum (Al)— and one body-centered cubic (bcc) —tantalum (Ta)— using standard embedded-atom method (EAM) potentials. We quantify entropic losses in coarse meshes and express  $\alpha$  using QC’s critical parameters. We rationalize the results in terms of the Debye-Grüneisen model and propose rescaling strategies for coarse systems.

This chapter is organized as follows: Section 2.1 provides a concise review of QC and the general framework for dissipative Lagrangian mechanics. Section 2.2 contains all the dynamic results for both Al and Ta and their interpretation within the quasiharmonic approximation. Finally, Section 2.3 presents a discussion of the results obtained in Section 2.2.

## 2.1 Theory

Molecular dynamics (MD) provides a straightforward way to simulate thermally activated processes and field gradient-driven effects, including heat and mass transport. However, the characteristic

time of MD is that of atomic vibrations, which limits the time and length scales accessible by direct simulation. Alternatively, when fields are smoothly varying, the configurational space can be discretized into finite elements (FE), where the reduced set of degrees of freedom is the ensemble of element vertices and the material laws are continuum in nature. This nodal representation reduces the computational overhead and allows to sample larger time and space scales.

In the presence of abrupt gradients, the FE method takes recourse to mesh refinement to improve the discrete representation of the elastic energy integrals for a continuous medium. However, when the mesh size approaches the atomistic limit, the constitutive relations are no longer valid, for they fail to capture the localized nature of the elastic energy functional. To circumvent this difficulty, combined atomistic/continuum approaches have been developed [16, 17]. These approaches use atomistic material descriptions where fields are non-linear (such as near lattice defects) while maintaining a coarse description elsewhere. In this fashion, the computational power is harnessed according to the complexity of the material laws, resulting in an optimal compromise between numerical accuracy and computational overhead. Compared to direct atomistics, these techniques have the potential to produce significant time and length scale gains by treating smoothly-varying regions of the configurational space collectively.

However, the existence of unstructured meshes during dynamic simulations gives rise to coupled domain boundaries separating portions of the configurational space with different resolutions. In such cases, interfaces may become non-compliant from a thermodynamic point of view, which results from the fact that continuum thermodynamics is formulated as a length scale-free theory, and cannot account for the discreteness associated with meshes of varying coarseness. As a consequence, time-dependent information may not be seamlessly transmitted, and the dynamic behavior across both sides of an interface is governed by the reflection of waves not supported by the domain of coarser description (and the transmission of those that are). While they may not generally be important at low temperatures for smoothly-discretized meshes, these effects are accentuated at resolutions that approach the atomistic scale at finite temperatures, a common occurrence in many situations of interest. This can lead to spurious thermodynamic behavior, with thermal gradients and other

artifacts originating from inhomogeneous boundaries. The most important effect is the unphysical heating of domains suffering reflections [10, 17, 18], which stems from the development of impedance discontinuities across coupled-domain boundaries. This is inherent to space discretization methods, and has not been strictly solved even in FE [19, 20]. Therefore, rules of thumb are used to determine how fast the element size can be increased during mesh transition, and viscous damping is employed in methods such as finite elements and finite differences [21].

Atomistic/continuum techniques that address this limitation have been developed by Cai et al. [11], and E & Zhongyi [22] using memory kernel functions and modified boundary Hamiltonians, respectively. However, both approaches have proven exceedingly demanding computationally, and have not been applied beyond simple proof-of-concept cases. Recently, more computationally-benign methods that minimize transmission impedances have been proposed. For example, Park et al. [23] have derived more compact time-history kernels for 2D simulations, resulting in 'bidirectional' dynamics that filter lattice waves automatically. Another noteworthy technique is the coarse-grained molecular dynamics (CGMD) method of Rudd and Broughton [10], which provides a consistent treatment of the short wavelength missing from the coarse finite element mesh. In CGMD, these short wavelength modes are taken to be in thermal equilibrium, and their average contribution is included in the dynamics of the system. Others, such as [24] and [25], have proposed techniques to model thermal flow across heterogeneous boundaries, whereby all impinging waves contribute to the temperature field of boundary nodes, which is then smoothly transmitted to the finite-element region. However, phonons do reflect at mesh interfaces, which in certain temperature ranges could lead to unphysical heating. Methods that take into account the lost entropy from the missing degrees of freedom in atomistic/continuum representations have been proposed for equilibrium thermodynamics simulations [14, 26–29]. These approaches succeed in computing full thermodynamic averages across domains although they suppress local thermal fluctuations and cannot be applied to compute transport phenomena.

### 2.1.1 Zero Temperature Quasicontinuum

To provide the background for subsequent developments, we briefly review the static Quasicontinuum (QC) theory developed by Tadmor et al. [8] and its adaptation by Knap and Ortiz [9]. We consider a set of  $N$  atoms occupying a subset of a simple 3-dimensional Bravais lattice. The coordinates of the atoms are denoted by  $\mathbf{Q}_i$ ,  $i = 1, \dots, N$  in the reference configuration, and by  $\mathbf{q}_i$ ,  $i = 1, \dots, N$  in the current (deformed) configuration. The energy of the crystal is assumed to be expressible as a function of the atomic coordinates,  $E(\mathbf{q})$ . Moreover, any applied loads are considered conservative and derived from an external potential  $\Phi^{\text{ext}}(\mathbf{q})$ . Therefore, the total potential energy of the crystal is:

$$V(\mathbf{q}) = E(\mathbf{q}) + \Phi^{\text{ext}}(\mathbf{q}) = \sum_i^N V_i \quad (2.1)$$

where an additive decomposition of the energy has been assumed. The stable equilibrium configurations of interest are the minimizers of this function, i. e., the solutions to the variational problem:

$$\inf_{\mathbf{q}} V(\mathbf{q}) \quad (2.2)$$

The essence of the QC method is to replace eq. (2.2) by a constrained minimization of  $V(\mathbf{q})$  over a suitably chosen subset  $\mathbf{q}_\alpha$ ,  $\alpha = 1, \dots, N_h$ . To define  $\{\mathbf{q}_h\}$  we begin by selecting a reduced set containing  $N_h < N$  *representative* atoms<sup>1</sup>. Additionally, let  $\mathcal{T}_h$  be a triangulation that supports a collection of continuous and piecewise linear shape functions  $\{\varphi(\mathbf{Q})\}$ . Shape functions have—in general—compact support, i. e., they are identically zero in all elements that don't contain the representative atom for which they were defined—let's call it  $\alpha$ . Moreover they have the property that  $\varphi_\alpha(\mathbf{Q}_\beta) = \delta_{\alpha\beta}$ . Then the position of any atom can be determined by interpolation of the representative ones  $\{\mathbf{q}_h\}$ :

$$\mathbf{q}_i = \sum_{\alpha}^{N_h} \varphi_{\alpha}(\mathbf{Q}_i) \mathbf{q}_{\alpha} \quad \forall i = 1, \dots, N \quad (2.3)$$

---

<sup>1</sup>Or *repatoms* for short

The reduced counterpart of eq. (2.2) then becomes:

$$\inf_{\mathbf{q}_h} V(\mathbf{q}) \quad (2.4)$$

The minimizers of the reduced problem follow from the reduced equations of equilibrium:

$$\mathbf{f}_\alpha = -\frac{\partial V}{\partial \mathbf{q}_\alpha} = -\sum_i^N \sum_j^N \frac{\partial V_i}{\partial \mathbf{q}_j} \varphi_\alpha(\mathbf{Q}_j) = \mathbf{0} \quad \forall \alpha = 1, \dots, N_h \quad (2.5)$$

The next key approximation is that each representative atom characterizes the energetics of some spatial neighborhood within the body. Therefore,

$$V = \sum_i^N V_i \approx \sum_\beta^{N_h} n_\beta V_\beta \quad (2.6)$$

where the weight  $n_\beta$  may be physically interpreted as the number of lattice sites *represented* by representative atom  $\beta$ . In addition, the practicality of the method hinges on the application of lattice summation rules in order to avoid the calculation of the full atomistic force array  $\mathbf{f}$  [8]. Specifically, the energy of each representative atom can be suitably approximated by visiting only a small subset of all atoms within the system [9]. A cluster of sampling points is defined around each repatom and the forces (eq. 2.5) are then approximated as

$$\mathbf{f}_\alpha \approx -\sum_\beta^{N_h} n_\beta \left[ \sum_{j \in \mathcal{C}_\beta} \frac{\partial V_\beta}{\partial \mathbf{q}_j} \varphi_\alpha(\mathbf{Q}_j) \right] \quad (2.7)$$

where the optimal cluster size is a trade-off between computational efficiency and accuracy, and is of the order of first or second neighbor shells according to Knap and Ortiz [9].

The calculation of effective forces in eq. (2.7) is of complexity  $O(N_h N_c)$  where  $N_c$  is the number of lattice sites in a cluster of radius  $r_c$ . Further details on the implementation and an analysis of the accuracy and convergence of the method may be found in [9]. The QC method has been successfully applied to a number of cases involving localized deformation and long-range fields, such

as nanoindentation [30], nanovoid deformation [31, 32], and nanopillar compression [33].

### 2.1.2 The Dynamical Theory

We start from Lagrange's equation for dissipative systems [34]:

$$\frac{d}{dt} \left( \frac{\partial L}{\partial \dot{\mathbf{q}}} \right) = \frac{\partial L}{\partial \mathbf{q}} - \frac{\partial \mathcal{F}}{\partial \dot{\mathbf{q}}} \quad (2.8)$$

where  $L(\mathbf{q}, \dot{\mathbf{q}}, t) = K - V$  is the Lagrangian, and  $K = \frac{1}{2} m \dot{\mathbf{q}} \dot{\mathbf{q}}^T$  and  $V(\mathbf{q})$  are the kinetic and potential energies of the system, respectively<sup>2</sup>. In addition,

$$\mathcal{F} = \frac{1}{2} \dot{\mathbf{q}}^T \mathbf{\Gamma} \dot{\mathbf{q}} \quad (2.9)$$

is known as Rayleigh's dissipation function and represents the rate at which mechanical energy is converted to heat during a viscous process,  $\dot{E} = -\dot{\mathbf{q}}^T \mathbf{\Gamma} \dot{\mathbf{q}}$ . In the last equation  $\mathbf{\Gamma}$  is a symmetric and positive-definite matrix whose components are the *damping* coefficients of the system. For homogeneous atomic systems, the viscosity matrix  $\mathbf{\Gamma}$  can be written as:

$$\mathbf{\Gamma} = \hat{m} \tau^{-1} \mathbf{I} \quad (2.10)$$

where  $\hat{m}$  is an appropriate particle mass,  $\tau$  is the characteristic damping time and  $\mathbf{I}$  is the identity matrix.

We now express the systems Lagrangian in reduced QC coordinates by recourse to expression (2.3),

$$L(\mathbf{q}, \dot{\mathbf{q}}) = \frac{1}{2} \sum_i^N m_i \left[ \sum_{\alpha}^{N_h} \dot{\mathbf{q}}_{\alpha} \varphi_{\alpha}(\mathbf{Q}_i) \right] \left[ \sum_{\beta}^{N_h} \dot{\mathbf{q}}_{\beta} \varphi_{\beta}(\mathbf{Q}_i) \right] - \sum_{\beta}^{N_h} V_{\beta} \left( \sum_{\alpha}^{N_h} \mathbf{q}_{\alpha} \varphi_{\alpha}(\mathbf{Q}_1), \dots, \sum_{\alpha}^{N_h} \mathbf{q}_{\alpha} \varphi_{\alpha}(\mathbf{Q}_Z) \right) \quad (2.11)$$

where  $Z$  is the number of lattice sites within the cluster around reatom  $\beta$ . Similarly, Rayleigh's

<sup>2</sup>For simplicity, hereafter we omit the explicit dependence of  $L$ ,  $K$  and  $V$  on time  $t$ .

dissipation function takes the form:

$$\mathcal{F}(\dot{\mathbf{q}}) = \frac{1}{2} \sum_i^N m_i \tau^{-1} \left[ \sum_{\alpha}^{N_h} \dot{\mathbf{q}}_{\alpha} \varphi_{\alpha}(\mathbf{Q}_i) \right] \left[ \sum_{\beta}^{N_h} \dot{\mathbf{q}}_{\beta} \varphi_{\beta}(\mathbf{Q}_i) \right] \quad (2.12)$$

Inserting eqs. (2.11) and (2.12) into eq. (2.8), the reduced problem becomes:

$$\sum_i^N \sum_{\beta}^{N_h} m_i \varphi_{\alpha} \varphi_{\beta} \ddot{\mathbf{q}}_{\beta} = - \sum_j^Z \sum_{\beta}^{N_h} n_{\beta} \varphi_{\alpha} \frac{\partial V_{\beta}}{\partial \mathbf{q}_j} - \sum_i^N \sum_{\beta}^{N_h} m_i \tau^{-1} \varphi_{\alpha} \varphi_{\beta} \dot{\mathbf{q}}_{\beta} \quad \forall \alpha = 1, \dots, N_h \quad (2.13)$$

By recourse to eq. (2.7) the equations of motion –in matrix notation– can be written as:

$$\mathbf{M}_h \ddot{\mathbf{q}}_h + \mathbf{\Gamma}_h \dot{\mathbf{q}}_h = \mathbf{f}_h(\mathbf{q}_h) \quad (2.14)$$

where

$$M_{\alpha\beta} = \sum_i^N m_i \varphi_{\alpha}(\mathbf{Q}_i) \varphi_{\beta}(\mathbf{Q}_i) \quad (2.15)$$

are the components of the *consistent* mass matrix  $\mathbf{M}_h$ , which is commonly replaced by a (diagonal) lumped mass matrix for computational convenience. In QC we utilize:

$$M_{\alpha\beta} = m_{\alpha} \delta_{\alpha\beta} = m n_{\alpha} \delta_{\alpha\beta} \quad (2.16)$$

where  $m$  is the material's atomic mass.

In order to solve eq. (2.14) we regard the reduced set of representative atoms  $\{\mathbf{q}_h\}$  as an ensemble of nodes suspended in a *medium* that characterizes the neglected degrees of freedom, a behavior typically described by Langevin dynamics. The effect of this medium may be approximated by a frictional drag on the set  $\{\mathbf{q}_h\}$  as well as random fluctuations from the thermal motion of solvent particles. Mapping eq. (2.14) to a Langevin equation requires  $\mathbf{f}$  to be decomposed in two parts:  $\mathbf{f} = \hat{\mathbf{f}} + \mathbf{R}(t)$ , where  $\hat{\mathbf{f}}$  are the body forces from eq. (2.7), and  $\mathbf{R}$  is an instantaneous random force.

The equations of motion then become,

$$\mathbf{M}_h \ddot{\mathbf{q}}_h + \tau^{-1} \mathbf{M}_h \dot{\mathbf{q}}_h = \hat{\mathbf{f}} + \mathbf{R}(t) \quad (2.17)$$

When the characteristic damping time  $\tau$  is much larger than the relaxation time scale associated with the fluctuations of the random force, equation (2.17) is the ordinary Langevin equation of a so-called *Markovian* system. Under such approximation  $\mathbf{R}$  can be taken as a stationary Gaussian random variable whose first and second moments are:

$$\begin{aligned} \langle \mathbf{R}(t) \rangle &= \mathbf{0} \\ \langle \mathbf{R}(t) \otimes \mathbf{R}_h(t') \rangle &= \frac{2mk_b T}{\tau \Delta t} \mathbf{I} \end{aligned} \quad (2.18)$$

where the first expression refers to the time average of the random force, the second gives the covariance matrix [35]; and  $k_b$  and  $T$  are the Boltzmann's constant and the absolute temperature, respectively.

For the examples to be presented in the next section, we solve eq. (2.17) at the nodal level, with each representative atom  $\alpha$  being immersed in a thermal bath represented by  $\mathbf{R}_\alpha(t)$ . The temperature of the system is maintained via eq. (2.18).

We integrate in time eq. (2.17) using a ( $\beta = 0$ ,  $\gamma = 0.5$ ) version of the Newmark method. As any other *explicit* method, it's only conditionally stable. Conditionality is removed from the stability criterion by ensuring that the time step  $\Delta t$  is less than the characteristic time of the system  $\tau$  [36]. However, the specific choice of time step and damping time is problem and material dependent. After an extensive number of numerical tests, the values of  $\Delta t$  and  $\tau$  that produce stable trajectories while maximizing time advancement are given in Table 2.1.

Finally, instantaneous values of  $\mathbf{R}_\alpha$  are generated by sampling from a normal distribution using the Box-Muller transformation [37]. Thus, if  $u_1$  and  $u_2$  are independent random variables uniformly distributed in the interval  $(0, 1]$  then:  $z_1 = (-2 \ln u_1)^{\frac{1}{2}} \cos(2\pi u_2)$  and  $z_2 = (-2 \ln u_1)^{\frac{1}{2}} \sin(2\pi u_2)$  are independent, normally-distributed variables with zero mean and unit variance. We discard one of

these values at random and trivially convert the other to a normal distribution of mean  $\mu = 0$  and variance  $\sigma^2 = 2mk_bT/(\tau\Delta t)$  as

$$R_{\alpha,i} = \mu + \sigma z \quad i = x, y, z \quad (2.19)$$

Further details can be found in [38].

Table 2.1: Time step and characteristic damping time for perfect crystal Al and Ta.

Material	$\Delta t$ (fs)	$\tau$ (fs)
Al	5.29	70.55
Ta	0.66	8.82

### 2.1.3 The Quasiharmonic Approximation in the QC Framework

The (Langevin-based) dynamic QC method presented previously is fully anharmonic. We now introduce a quasiharmonic approximation of the QC framework to rationalize the results of dynamic QC in sections to come.

Consider the special case where the potential function  $V$  admits a harmonic representation, this is:

$$V(\mathbf{q}_h) = V(\mathbf{q}_{h,0}) + \frac{1}{2} (\mathbf{q}_h - \mathbf{q}_{h,0})^T \mathbf{K}(\mathbf{q}_{h,0}) (\mathbf{q}_h - \mathbf{q}_{h,0}) \quad (2.20)$$

where  $\mathbf{q}_{h,0}$  represents an equilibrium configuration of the system and  $\mathbf{K}$  is the *Hessian* of  $V$ . Without loss of generality, we will assume that  $\mathbf{q}_{h,0}$  is the reference configuration ( $\mathbf{q}_{h,0} = \mathbf{Q}_h$ ), i. e., a particular solution of eq. (2.4) that satisfies the equilibrium conditions (2.5) when  $\Phi^{\text{ext}} = 0$ . On the other hand, the components of  $\mathbf{K}$  are:

$$K_{ij}(\mathbf{Q}_\alpha, \mathbf{Q}_\beta) = \left. \frac{\partial^2 E}{\partial q_{\alpha,i} \partial q_{\beta,j}} \right|_{\mathbf{q}_\alpha = \mathbf{Q}_\alpha, \mathbf{q}_\beta = \mathbf{Q}_\beta} \quad (2.21)$$

where  $K_{ij}(\mathbf{Q}_\alpha, \mathbf{Q}_\beta)$  are known as *force constants* and give the reaction along  $j$  of node  $\mathbf{Q}_\beta$  when node  $\mathbf{Q}_\alpha$  is infinitesimally displaced along  $i$ . Notice that these quantities are mesh and cluster size

dependent.

The equations of motion for the reduced QC system interacting via a harmonic potential of the form given in (2.20) are:

$$\mathbf{M}_h \ddot{\mathbf{q}}_h = \mathbf{K} (\mathbf{q}_h - \mathbf{Q}_h) \quad (2.22)$$

or alternatively,

$$\ddot{\mathbf{u}}_h = \mathbf{D} \mathbf{u}_h \quad (2.23)$$

where  $\mathbf{u}_h = \mathbf{M}_h^{-\frac{1}{2}} (\mathbf{q}_h - \mathbf{Q}_h)$  are the *mass-weighted displacements*, and  $\mathbf{D} = \mathbf{M}_h^{-\frac{1}{2}} \mathbf{K} \mathbf{M}_h^{-\frac{1}{2}}$  is the *dynamical* matrix.  $\mathbf{D}$  is usually Hermitian, and by virtue of the geometric symmetries of cubic metals it is real as well, and hence symmetric. For eq. (2.23) it is customary to seek solutions of the type [39]:

$$\mathbf{u}_h(\mathbf{q}_h) = \mathbf{y}_h \exp[-i(\omega t - \mathbf{k} \cdot \mathbf{q}_h)] \quad (2.24)$$

where  $\mathbf{y}_h$  is a polarization direction,  $\omega$  is a vibration frequency, and  $\mathbf{k}$  is a wave vector. Then, eq. (2.23) becomes:

$$\mathbf{D} \mathbf{y}_h = \omega^2 \mathbf{y}_h \quad (2.25)$$

Solving this eigenvalue problem<sup>3</sup> yields the  $3N_h$  normal modes of vibration  $\omega$  and the eigenvectors  $\mathbf{y}_h$  of the reduced QC system.

Now, combining the definition of the dynamical matrix with eq. (2.16), its components can be written as

$$D_{ij}(\mathbf{Q}_\alpha, \mathbf{Q}_\beta) = \frac{K_{ij}(\mathbf{Q}_\alpha, \mathbf{Q}_\beta)}{m \sqrt{n_\alpha n_\beta}} \quad (2.26)$$

In the atomistic limit, all the nodal weights  $n$  are equal to unity and eq. (2.26) takes the standard microscopic form [39]. When that's not the case, we make use of the expressions derived by Knap

---

<sup>3</sup>Since  $\mathbf{D}$  is real and symmetric, it can always be diagonalized.

and Ortiz [9] to define the nodal weights in the context of cluster-based summation rules<sup>4</sup>:

$$n_\alpha = \frac{\sum_i^N \varphi_\alpha(\mathbf{Q}_i)}{\sum_\beta^{N_h} \sum_{j \in \mathcal{C}_\beta} \varphi_\beta(\mathbf{Q}_j)} \quad (2.27)$$

The numerator in eq. (2.27) adds to the total number of atoms in the system  $N$ . The denominator –on the other hand– can be approximated for structured meshes (all simplices in  $\mathcal{T}_h$  equal) as  $N_c N_h$ , which gives:

$$n_\alpha \approx \frac{N}{N_c N_h} \quad \forall \alpha = 1, \dots, N_h \quad (2.28)$$

Introducing this simplified form of  $n_h$  in eq. (2.26):

$$D_{ij}(\mathbf{Q}_\alpha, \mathbf{Q}_\beta) \approx \frac{N_c N_h}{m_N} K_{ij}(\mathbf{Q}_\alpha, \mathbf{Q}_\beta) \quad (2.29)$$

The number of lattice sites  $N_c$  in a cluster of radius  $r_c$  is  $N_c = \frac{4\pi}{3} r_c^3 \rho$ , where  $\rho = N/V$  is the atomic density of the undeformed configuration. Similarly, the ratio  $N/N_h$  gives the number of atoms per simplex in structured meshes. Assuming a tetrahedral triangulation with characteristic element size  $h$ :

$$\frac{N}{N_h} \approx \rho c h^3 \quad (2.30)$$

where  $c$  is geometric constant ( $c = \frac{1}{\sqrt{72}}$  for regular tetrahedra). It then follows from eq. (2.29) that:

$$D_{ij}(\mathbf{Q}_\alpha, \mathbf{Q}_\beta) \approx \frac{4\pi}{3mc} \left(\frac{r_c}{h}\right)^3 K_{ij}(\mathbf{Q}_\alpha, \mathbf{Q}_\beta) \quad (2.31)$$

Noting that  $\omega \propto \sqrt{D}$  we have:

$$\omega \propto \left(\frac{r_c}{h}\right)^{\frac{3}{2}} \sqrt{K_{ij}(\mathbf{Q}_\alpha, \mathbf{Q}_\beta)} \quad (2.32)$$

Eq. (2.32) contains length scale dependencies of fundamental importance in the Quasicontinuum context and will be used to rationalize entropy depletion in sections to come.

To link the vibrational properties of QC systems with fundamental crystal properties such as

---

<sup>4</sup>In Section 3.2 of their paper.

the thermal expansion coefficient –which will become the metric to quantify entropy depletion– we assume the reduced system to be governed by a Hamiltonian of the form:

$$\mathcal{H}_h(\mathbf{q}_h, \mathbf{p}_h, \theta) = \sum_{\alpha}^{N_h} \frac{\mathbf{p}_{\alpha}^2}{2m_{\alpha}} + V(\mathbf{q}_h, \theta) \quad (2.33)$$

where  $\mathbf{p}_{\alpha} = m_{\alpha} \dot{\mathbf{q}}_{\alpha}$  are the momenta of repatom  $\alpha$ . In addition we just consider cubic crystals (for which thermal expansion is isotropic) and thus we only take into account a dependence on the volumetric strain  $\theta = \Delta V/V$  in eq. (2.33). The partition function for the system of *distinguishable* particles associated with this Hamiltonian is [40]:

$$Z_h(\theta, T) = \frac{1}{h^{3N_h}} \int \exp \left[ -\frac{\mathcal{H}_h(\mathbf{q}_h, \mathbf{p}_h, \theta)}{k_b T} \right] d\mathbf{q}_h d\mathbf{p}_h \quad (2.34)$$

where  $h$  is Planck's constant. Since the potential function  $V$  admits a harmonic form, the free energy  $F_h$  takes the form:

$$\begin{aligned} F_h(\theta, T) &= -k_b T \ln Z_h(\theta, T) \\ &= V(\mathbf{0}, \theta) - k_b T \left( \frac{3N_h}{2} \ln \left[ \frac{(2\pi)^2 m k_b^2 T^2}{h^2} \right] - \sum_i^{3N_h} \ln(\omega_i(\theta)) \right) \end{aligned} \quad (2.35)$$

where again  $\omega_i(\theta)$  are the eigenfrequencies of  $\mathbf{K}$ . The full derivation of this expression can be found in Appendix I.

Now, in the limit of small deformations, the volumetric expansion coefficient  $\beta$  for isotropic media is given by the following thermodynamic relation:

$$\begin{aligned} \beta = 3\alpha &= \frac{1}{V_0} \left. \frac{\partial V}{\partial T} \right|_p \\ &= \frac{1}{(1-\theta)^2} \left. \frac{\partial \theta}{\partial T} \right|_p = \frac{1}{(1-\theta)^2} \left. \frac{\partial \theta}{\partial p} \right|_T \left. \frac{\partial p}{\partial T} \right|_V = -\frac{1}{B(1-\theta)} \left. \frac{\partial p}{\partial T} \right|_V \end{aligned} \quad (2.36)$$

where  $\alpha$ ,  $p$  and  $B = -V \left. \frac{\partial p}{\partial V} \right|_T$  are, respectively, the linear expansion coefficient, the pressure and the (isothermal) bulk modulus. The term  $(1-\theta)^{-1}$  is simply the ratio  $V/V_0$ , where  $V_0$  is a reference

volume usually taken as that of the undeformed configuration at 0 K. The pressure can be directly obtained as

$$p = - \left. \frac{\partial F}{\partial V} \right|_T = \frac{1}{V} \frac{\partial F}{\partial \{\ln(1 - \theta)\}} \quad (2.37)$$

and therefore:

$$\alpha = - \frac{1}{3BV_0} \frac{\partial^2 F}{\partial T \partial \{\ln(1 - \theta)\}} \quad (2.38)$$

Inserting eq. (2.35) into (2.38), the *reduced* thermal expansion coefficient evaluates to:

$$\alpha = - \frac{k_b}{3BV_0} \sum_{i=1}^{3N_h} \frac{\partial \{\ln \omega_i(\theta)\}}{\partial \{\ln(1 - \theta)\}} \quad (2.39)$$

where the term inside the sum is known as the *individual Grüneisen* parameter of each normal mode and measures the variation of  $\omega_i$  with deformation [41,42]. Thus, within the quasiharmonic approximation, it is assumed that Grüneisen parameters are independent of temperature, which gives rise to constant thermal expansion coefficients in the entire temperature range [43]. This is generally acceptable for transition metals, although notable exceptions exist, as we shall see. A more in-depth discussion on the validity of the quasiharmonic approximation for thermal expansion calculations can be found in Srivastava [43], Touloukian et al. [44] and Ho and Taylor [45].

The last two terms on the r.h.s. of eq. (2.35) give an idea of the entropy loss in the reduced QC system. Limiting the sums at  $N_h$  rather than  $N$  particles will intrinsically result in lower entropic contributions to the total free energy. In addition to fewer available eigenstates, equation (2.32) shows that these are modulated by the *weight factor*  $(r_c/h)^{3/2}$  (which typically  $< 1$ ). Then for a fixed  $N_h$  the entropy will be further diminished by mesh effects. According to eq. (2.39) both effects impact directly the thermal expansion coefficient  $\alpha$ .

In calculations, we obtain the free energy  $F$  from eq. (2.35) and  $\alpha$  from eq. (2.39). The term  $V(\mathbf{0}, \theta)$  and the eigenfrequencies  $\omega(\theta)$  are calculated statically with QC. The thermal expansion coefficients computed in this fashion can then be compared with the *dynamic* values of  $\alpha$ .

## 2.2 Numerical Results

In this section we study the dynamic behavior of Al and Ta as a function of three critical QC parameters: system size  $N$ , mesh size  $N_h$ , and cluster size  $r_c$ . The objective is to assert the effect of each on the thermal expansion coefficient  $\alpha$  of both material systems.

### 2.2.1 Aluminum Results

#### 2.2.1.1 Thermal Expansion from Dynamic Simulations

To measure  $\alpha$  directly from canonical QC runs, we perform a series of simulations for a given configuration  $(N, N_h, r_c)$  at several temperatures, using the parameters of Table 2.1. When the system reaches steady state, we perform a time average of the observed volume as:

$$\langle V \rangle_T = \frac{1}{n_t} \sum_{i=1}^{n_t} V_i(N, N_h, r_c)|_T \quad (2.40)$$

where  $n_t$  is a sufficiently high number of time steps post-steady state ( $i = 1$ ) and  $V_i$  is the instantaneous system volume at time  $t_i = i\Delta t$ .  $V_i$  is computed directly by adding all tetrahedral element volumes in  $\mathcal{T}_h$ . Then, the thermal expansion coefficient is obtained as:

$$\alpha(N, N_h, r_c) = \frac{1}{3V_0} \frac{d\langle V \rangle_T}{dT} \quad (2.41)$$

where  $V_0(N, N_h, r_c)$  is the equilibrium volume of the system obtained via static relaxation. As is customary [44, 46], the thermal expansion coefficient is evaluated at room temperature (298 K) from a third-degree polynomial fit to the data.

For simplicity, hereafter we refer to cluster sizes in terms of the maximum nearest-neighbor shell they encompass. For fcc crystals, cluster sizes of 2, 3 and 4 indicate  $r_c \approx a_0$ ,  $1.225a_0$ , and  $1.414a_0$ , and contain 18, 42 and 54 lattice points, respectively. In addition, and for a number of reasons not related to this work [9], our test samples are always finite cubic systems. This introduces the need to monitor surface effects and capillary forces –nonexistent in periodic systems– on volume expansion.

These effects are not expected to be important for sufficiently large systems.

Fcc Al is modeled using the glue potential developed by Ercolessi and Adams [47], which has been fitted using the experimental lattice constant  $a_0 = 4.032 \text{ \AA}$  and the three cubic elastic moduli. One salient feature of this potential is that it has excellent surface and thermal properties [48], something of particular importance in our case, since we only simulate finite systems.

QC contains full atomistics and continuum elasticity as special limits. As such, the natural limit of our finite-temperature QC at the finest scale is MD. Ercolessi and Adams give a thermal expansion coefficient of  $\alpha_{\text{MD}} = 1.79 \times 10^{-5} \text{ K}^{-1}$  at room temperature for a periodic Al system containing 10752 particles [47]<sup>5</sup>. To establish the atomistic baseline we first perform dynamic QC simulations using  $16a_0 \times 16a_0 \times 16a_0$  and  $32a_0 \times 32a_0 \times 32a_0$  finite Al crystals containing 17969 and 137313 atoms, respectively. For these systems  $V_0$  is  $2.662 \times 10^5$  and  $2.138 \times 10^6 \text{ \AA}^3$ . Figure 2.1 shows the temperature dependence of the systems' volume. Third-degree polynomial fits to the data yield  $\alpha_{\text{at}} = 1.72 \times 10^{-5}$  and  $1.70 \times 10^{-5} \text{ K}^{-1}$  at 298 K for the 17969 and 137313-atom systems. The polynomial coefficients are given in Table 2.2. The small discrepancy ( $\approx 4\%$ ) between the periodic MD sample considered by Ercolessi and Adams and our finite systems suggests that the associated surface effects are small.

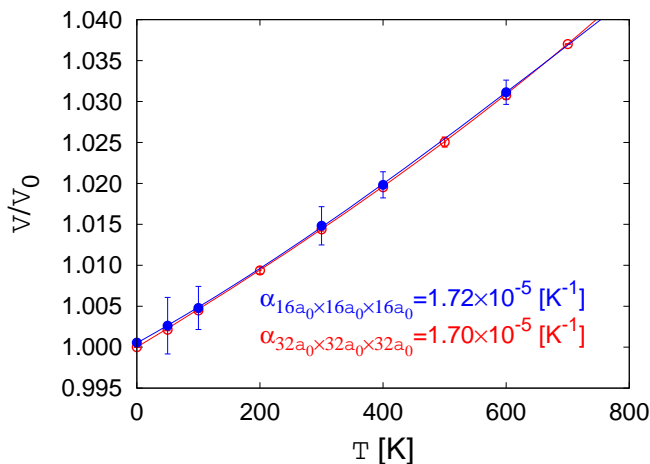


Figure 2.1: Thermal expansion behavior of two finite Al crystals containing 17969 (dimensions:  $16_0 \times 16_0 \times 16a_0$ ) and 137313 ( $32a_0 \times 32a_0 \times 32a_0$ ) atoms. The error bars (very small for the  $32_0 \times 32_0 \times 32a_0$  system) are associated with volume fluctuations at equilibrium.

<sup>5</sup>Pearson gives an experimental value of  $2.36 \times 10^{-5} \text{ K}^{-1}$  [49].

Table 2.2: Coefficients of the third degree polynomials  $V(T)/V_0 = aT^3 + bT^2 + cT + d$  plotted in Fig. 2.1. From eq. (2.41),  $\alpha(T) = \frac{1}{3}(3aT^2 + 2bT + c)$ . Since at  $T = 0$ ,  $V(0) = V_0$ ;  $d$  is set equal to one.

Sample size	a	b	c	d
$16a_0 \times 16a_0 \times 16a_0$	$-8.53 \times 10^{-12}$	$2.06 \times 10^{-8}$	$4.17 \times 10^{-5}$	1.00
$32a_0 \times 32a_0 \times 32a_0$	$6.10 \times 10^{-12}$	$6.18 \times 10^{-9}$	$4.56 \times 10^{-5}$	1.00

Next we study cluster and mesh size effects on  $V_0$ , see eq. (2.41). For this analysis, we conveniently express the mesh size in terms of the total number of represented atoms  $n'_h = N/N_h$ , which can be regarded as a first-order measure of the nodal weight. Alternatively, the inverse of  $n'_h$  acts as the  $N$ -normalized number of representative atoms. We have considered two types of meshes, simple cubic (sc) and face-centered cubic (fcc)<sup>6</sup>. The variation of  $V_0$  as a function of  $1/n'_h$  and  $r_c$  is displayed in Fig. 2.2. Results are normalized to the fully-atomistic relaxed volumes given in the previous paragraph. For small numbers of  $N_h$ , both parameters have a noticeable influence on the value of  $V_0$ . However, at  $1/n'_h \approx 0.14$ ,  $V_0$  converges to the atomistic volume.

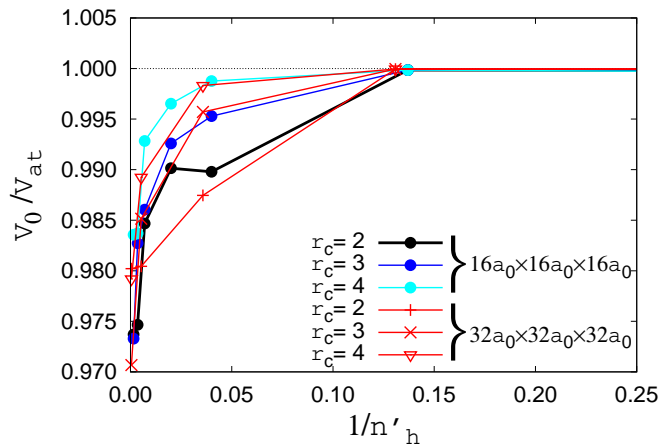


Figure 2.2: Normalized equilibrium volume  $V_0$  as a function of the normalized number of representative atoms. Volumes are calculated via conjugate-gradient energy minimizations and are normalized to the relaxed volumes of the atomistic systems.

To ascertain the effect of mesh ( $N_h$ ) and cluster size ( $r_c$ ) on the thermal expansion coefficient  $\alpha$ , we have carried out simulations with different coarseness and cluster sizes. By way of example, Fig. 2.3 shows the time evolution of the system's volume for different temperatures in the ( $N=137313$ ,

<sup>6</sup>Note that the underlying atomistic structure for Al is always fcc, even if the constructed triangulation is sc.

$N_h=729$ ,  $r_c=4$ ) system.  $\langle V \rangle_T$  is obtained from eq. (2.40) based on measurements taken during  $\sim 30$  to  $50$  ps after steady state. The behavior of any system is qualitatively similar to that shown in Fig. 2.3, with larger fluctuations occurring for a given temperature as  $N_h$  decreases.

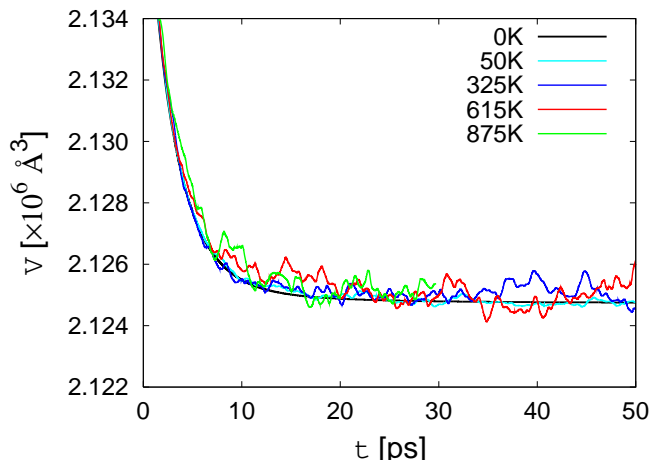


Figure 2.3: Time evolution of the system volume at five different temperatures for the ( $N=137313$ ,  $N_h=729$ ,  $r_c=4$ ) system. Measurements start only after steady state has been reached (25 ps).

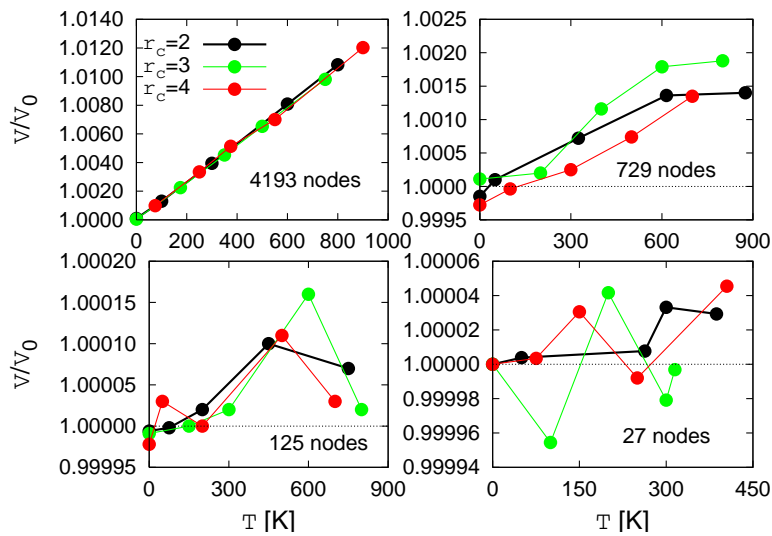


Figure 2.4: Thermal expansion behavior of a  $16a_0 \times 16a_0 \times 16a_0$  Al system containing 17989 lattice sites. Four mesh and three cluster sizes were considered.

Results for four representative configurations are shown in Figs. 2.4 and 2.5. Since the structure displayed by each curve (each mesh) is not necessarily related to the  $V$ - $T$  behavior, using third-degree polynomial fits would be inadequate in these cases. Hence, for this specific analysis we

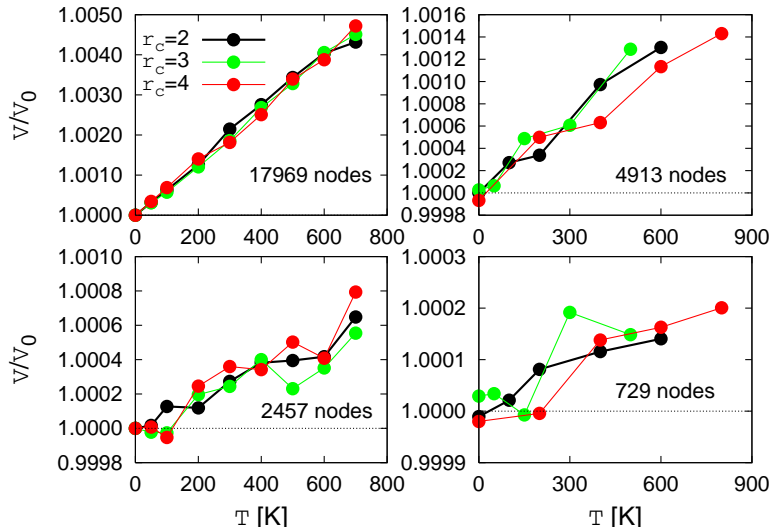


Figure 2.5: Thermal expansion behavior for a  $32a_0 \times 32a_0 \times 32a_0$  Al system containing 137313 lattice sites. Four mesh and three cluster sizes were considered.

assume constant thermal expansion and simply fit the data to a linear equation of the form:

$$V_{\text{eq}}(T) = cT + V_0 \quad (2.42)$$

where –naturally–  $\alpha = c/3V_0$ . Results are compiled in Table 2.3. Based on this Table and Figs. 2.4 and 2.5, two general assertions can be made. First, the dominant linear behavior of the  $V$ - $T$  relation is gradually lost with mesh coarsening. Indeed, for the 729-node case, the system’s volume shows no clear temperature dependence and only uncorrelated excursions about  $V/V_0 = 1$  are observed. The slope of the curves (directly proportional to the thermal expansion coefficient  $\alpha$ ) also diminishes with increasing mesh size. Second, cluster size has little or no effect on the temperature behavior of the system’s volume.

The values of  $\alpha$  compiled in Table 2.3 are plotted in Figure 2.6 as a function of the average number of lattice sites represented per node  $n'_h$ . Clearly, for low values of  $n'_h$  ( $\leq 50$ ), the cluster size dependence is practically nonexistent. For larger values (or coarser meshes) some uncorrelated variability appears.

Intuitively one would expect the expansion coefficient  $\alpha$  to vanish when the normalized number

Table 2.3: Compilation of thermal expansion coefficients  $\alpha$  (in  $K^{-1}$ ) for the  $16a_0 \times 16a_0 \times 16a_0$  and the  $32a_0 \times 32a_0 \times 32a_0$  Al systems –17989 and 137313 lattice sites, respectively. Results were obtained from dynamic simulations. Atomistic systems yield  $\alpha = 1.72 \times 10^{-5}$  and  $1.70 \times 10^{-5} K^{-1}$ , respectively.

	Mesh size		Cluster size		
	$N_h$	$N/N_h$	2	3	4
$16a_0 \times 16a_0 \times 16a_0$	27	666.3	$2.60 \times 10^{-8}$	$7.61 \times 10^{-9}$	$2.90 \times 10^{-8}$
	125	143.9	$4.19 \times 10^{-8}$	$3.53 \times 10^{-8}$	$3.21 \times 10^{-8}$
	365	49.3	$2.76 \times 10^{-7}$	$1.37 \times 10^{-7}$	$3.64 \times 10^{-7}$
	729	24.7	$6.12 \times 10^{-7}$	$8.55 \times 10^{-7}$	$7.51 \times 10^{-7}$
	2457	7.3	$2.29 \times 10^{-6}$	$2.12 \times 10^{-6}$	$2.14 \times 10^{-6}$
	4913	3.7	$4.49 \times 10^{-6}$	$4.35 \times 10^{-6}$	$4.42 \times 10^{-6}$
$32a_0 \times 32a_0 \times 32a_0$	729	188.4	$7.24 \times 10^{-8}$	$6.61 \times 10^{-8}$	$8.53 \times 10^{-8}$
	2457	55.9	$2.80 \times 10^{-7}$	$2.48 \times 10^{-7}$	$3.44 \times 10^{-7}$
	4913	27.9	$7.41 \times 10^{-7}$	$8.25 \times 10^{-7}$	$6.05 \times 10^{-7}$
	17969	7.6	$2.17 \times 10^{-6}$	$2.22 \times 10^{-6}$	$2.20 \times 10^{-6}$
	35937	3.8	$4.10 \times 10^{-6}$	–	–

of representative atoms  $N_h/N = 1/n'_h$  goes to zero. Additionally, in the atomistic limit ( $n'_h = 1$ ), the thermal expansion coefficient should be equal to that calculated in Fig. 2.1. Consequently we fit the calculated values to a function of the form  $\alpha(n'_h) = a/n'_h{}^b$ , where  $a$  and  $b$  are constants. From the previous discussion  $a \equiv \alpha(1) \equiv \alpha_{\text{at}}$ . It is not clear *a priori* what the value of  $b$  should be, although  $b = 1$  would suffice to meet the above conditions. In any case, after considering the subset of data corresponding to  $r_c = 4$  (including both sample sizes), the least-squares fitting results in  $\alpha(n'_h) = 1.53 \times 10^{-5} n'_h{}^{-0.97}$ . The obtained  $a$  and  $b$  are in excellent agreement with their rationalized values. Adding any other subset to the fitting procedure only results in small deviations on the value of  $a$  and  $b$ . It is worth noting, however, that the  $16a_0 \times 16a_0 \times 16a_0$  results appear to indicate the existence of two regimes, both characterized by the same exponent  $b \approx 1$  but with slightly different prefactors. The one below  $n'_h \approx 50$  yields the previous value of  $a$ , whereas the one above is about 10% lower. On the basis of the results shown in Figs. 2.4 and 2.5 –where for coarser meshes the linear behavior of  $\alpha$  is poorly established– we simply attribute this effect to noise in the thermal expansion measurements and assume that all the data follow the same physical behavior with sporadic excursions due to numerical error.

We emphasize that for  $n'_h = 1$  we recover the atomistic thermal expansion coefficient from a

data set that includes meshes of varying coarseness but not the fully atomistic configuration. This is an important and encouraging result, for it implies that the thermal expansion limit is naturally recovered from dynamic QC simulations, and that  $\alpha$  is inversely proportional to the *weight* of the representative atoms. Evidently, in the limit of an infinitely coarse mesh  $\alpha$  tends to zero, as there are no vibrational DOF to support any volumetric expansion. It is hence verified that,  $\forall n'_h \in [1, \infty)$ :

$$\lim_{n'_h \rightarrow 1} \alpha(n'_h) = \alpha_{at} \quad (2.43)$$

and

$$\lim_{n'_h \rightarrow \infty} \alpha(n'_h) = 0 \quad (2.44)$$

The behavior of  $\alpha$  shown in Fig. 2.6 also suggests that it does not depend on the total system size. This implies that our  $16a_0 \times 16a_0 \times 16a_0$  and  $32a_0 \times 32a_0 \times 32a_0$  samples are big enough for surface effects to be negligible.

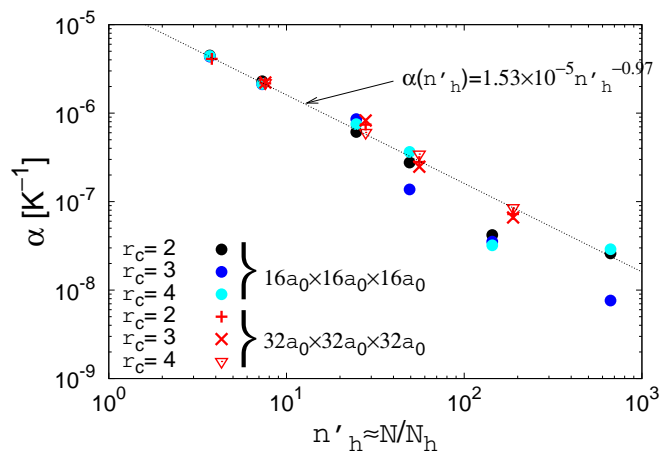


Figure 2.6: Thermal expansion coefficient as a function of the approximate nodal weights. The dashed line is a least-squares fit to the data corresponding to  $r_c = 4$ .

### 2.2.1.2 Thermal Expansion within the Quasiharmonic Approximation

In this section we rationalize the results obtained via direct dynamic QC simulations within the framework derived in Section 2.1.3. Our objective is to recover the thermal expansion coefficient

attendant to each  $(N, N_h, r_c)$  system from fundamental crystal properties.

To evaluate the volume derivatives in eq. (2.39) we first compute  $F_h$ - $\theta$  curves using eq. (2.35) at several temperatures. We sample a sufficient number of points in order the equilibrium volume to be enclosed in the volume range explored. As shown in Section 2.1.3, within the quasiharmonic approximation  $V$  is linear in  $T$ , so we simply fit the *locus* of temperature-dependent equilibrium volumes to eq. (2.42). In this fashion, the Grüneisen parameter is calculated indirectly and the thermal expansion coefficient can be readily obtained. This approach requires to obtain –for each  $(N, N_h, r_c)$  system– both the internal energy,  $V(\mathbf{0}, \theta)$  in eq. (2.35), and the normal modes of vibration (via eq. 2.25) for different volumes.

To test the validity of this approximation, we first calculate the atomistic thermal expansion coefficient and compare it to the value of  $\alpha_{\text{at}} = 1.79 \times 10^{-5} \text{ K}^{-1}$  given by Ercolessi and Adams [47]. We calculate  $F_h(T, a/a_0)$  as a function of the linear dimensional change  $a/a_0$ <sup>7</sup> for a periodic 4000-atom system and plot it in Fig. 2.7(a) for different temperatures. From second-order polynomial fits to the data we obtain the equilibrium lattice constant  $a$  at each temperature. The temperature dependence of these equilibrium lattice parameters gives a linear expansion coefficient  $\alpha = 1.79 \times 10^{-5} \text{ K}^{-1}$ , in perfect agreement with the value obtained by Ercolessi and Adams from MD simulations.

This result confirms the validity of the quasiharmonic approximation for Al and allows us to undertake the coarse-mesh calculations with confidence. However, for further verification, we now repeat this calculation for a  $10a_0 \times 10a_0 \times 10a_0$  finite system (4631 atoms) with free boundaries, akin to those used in QC simulations. The quasiharmonic analysis is shown in Fig. 2.7(b). This time, the calculation yields  $\alpha = 1.71 \times 10^{-5} \text{ K}^{-1}$ , which is in excellent agreement with the value of  $\alpha = 1.70 - 1.72 \times 10^{-5} \text{ K}^{-1}$  obtained directly from QC dynamical simulations in Fig. 2.1. Even though we are concerned with systems containing 17969 and 137313 atoms, the size of the dynamical matrices  $\mathbf{D} \in \mathbb{R}^{3N_h \times 3N_h}$  that can be diagonalized is restricted to  $\approx 13500 \times 13500$ . However, as for the simulations carried out in Section 2.2.1.1, the good agreement between the calculation for the  $10a_0 \times 10a_0 \times 10a_0$  sample and the results obtained for both the  $16a_0 \times 16a_0 \times 16a_0$  and the

---

<sup>7</sup>Note that  $V/V_0 \approx 3a/a_0$ , and  $\theta = \Delta V/V_0 \approx 3\Delta a/a_0$ .

$32a_0 \times 32a_0 \times 32a_0$  systems suggests that we are beyond the limit where surface effects depend on length scale. Thus, the value of  $\approx 1.71 \times 10^{-5} \text{ K}^{-1}$  constitutes our reference baseline against which all the coarse systems to be studied subsequently are benchmarked.

Having confirmed the validity of the approach described in Section 2.1.3, we now study mesh and cluster size effects. We compute  $\alpha$  using the procedure described in Fig. 2.7. The thermal expansion coefficients associated with these meshes are given in Table 2.4. The number of cases for the  $32a_0 \times 32a_0 \times 32a_0$  system is again limited by the size of the dynamical matrices that can be diagonalized.

Table 2.4: Thermal expansion coefficients (in  $K^{-1}$ ) calculated within the quasiharmonic approximation for the systems considered in Table 2.3. ‘-’ symbols indicate that the diagonalization of the corresponding dynamical matrices was beyond our computational capabilities.

	Mesh size		Cluster size		
	$N_h$	$n'_h$	2	3	4
$16a_0 \times 16a_0 \times 16a_0$	27	666.3	$7.28 \times 10^{-8}$	$4.33 \times 10^{-8}$	$4.88 \times 10^{-8}$
	125	143.9	$1.81 \times 10^{-7}$	$2.09 \times 10^{-7}$	$1.55 \times 10^{-7}$
	365	49.3	$4.06 \times 10^{-7}$	$3.77 \times 10^{-7}$	$3.52 \times 10^{-7}$
	729	24.7	$8.92 \times 10^{-7}$	$8.30 \times 10^{-7}$	$8.11 \times 10^{-7}$
	2457	7.3	$2.50 \times 10^{-6}$	$2.35 \times 10^{-6}$	$2.35 \times 10^{-6}$
	4913	3.7	-	-	-
$32a_0 \times 32a_0 \times 32a_0$	729	188.4	$1.27 \times 10^{-7}$	$1.19 \times 10^{-7}$	$1.21 \times 10^{-7}$
	2457	55.9	$3.71 \times 10^{-7}$	$3.46 \times 10^{-7}$	$1.03 \times 10^{-6}$
	4913	27.9	-	-	-
	17969	7.6	-	-	-
	35937	3.8	-	-	-

The results obtained thus far suggest that cluster size has a negligible impact on the thermal expansion behavior of coarse Al samples (cf. Figs. 2.4, 2.5 and 2.6). In fact, cluster size seems important only in the context of static energy minimizations, see Fig. 2.2.

## 2.2.2 Tantalum Results

### 2.2.2.1 Thermal Expansion from Dynamic Simulations

Bcc Ta is modeled using the EAM potential developed by Li et al. [50], which has been fitted to an experimental equation of state that includes data at 10% compression. Figure 2.8 shows the

temperature dependence of Ta lattice parameter  $a$  obtained for a periodic system using MD [50]. In addition, it also depicts experimental data taken from Touloukian et al. [44]. The atomistic data show inverse thermal expansion below 298 K, which is an artifact of the interatomic potential [50]. According to a third-degree polynomial fit (see Table 2.5), the thermal expansion coefficient displays a strong temperature dependence. Between 500 and 1500K –where a reasonably linear dependence exists– Touloukian et al. give a value of  $\alpha = 7.79 \times 10^{-6} K^{-1}$ , whereas the MD results suggest a value of  $6.02 \times 10^{-6} K^{-1}$ . As  $T$  increases, however, the differences become more pronounced.

For the dynamic QC study, we have analyzed  $20a_0 \times 20a_0 \times 20a_0$  (17261 atoms) and  $30a_0 \times 30a_0 \times 30a_0$  (56791 atoms) finite systems. As was the case for Al, we start by obtaining the corresponding atomistic thermal expansion behavior. Results are also shown in Fig. 2.8, where several features are noteworthy. First, thermal expansion in finite systems is considerably suppressed with respect to periodic (infinite) samples. Second, both curves reproduce the artificial negative thermal expansion coefficient below room temperature. Additionally, at high temperatures, the behavior of both  $20a_0 \times 20a_0 \times 20a_0$  and  $30a_0 \times 30a_0 \times 30a_0$  systems gradually diverges. Polynomial fits to the QC data are given in Table 2.5. The average thermal expansion coefficient in the  $1000 < T < 2000 K$  interval is, respectively,  $4.14 \times 10^{-6}$  and  $2.36 \times 10^{-6} K^{-1}$ . These now constitute our reference values for the coarse QC simulations.

Table 2.5: Coefficients of third degree polynomial  $[a(T)/a(298 K) - 1] = aT^3 + bT^2 + cT + d$  fits to dynamic QC simulations plotted in Fig. 2.8. The linear thermal expansion coefficient is calculated as:  $\alpha(T) = 3aT^2 + 2bT + c$ .

Sample size	a	b	c	d
$20a_0 \times 20a_0 \times 20a_0$	$-6.52 \times 10^{-13}$	$3.67 \times 10^{-9}$	$-3.59 \times 10^{-6}$	$1.28 \times 10^{-3}$
$30a_0 \times 30a_0 \times 30a_0$	$-3.37 \times 10^{-13}$	$2.09 \times 10^{-9}$	$-2.07 \times 10^{-6}$	$5.23 \times 10^{-4}$

The discrepancies observed between finite and periodic systems could indicate that surface effects are non-negligible in this case. This is further substantiated by the difference between the  $20a_0 \times 20a_0 \times 20a_0$  and  $30a_0 \times 30a_0 \times 30a_0$  systems themselves.

Next, we examine the thermal expansion behavior of gradually coarser meshes. Figures 2.9 and 2.10 show the results obtained using three cluster sizes. For bcc lattices,  $r_c = 2, 3, 4$  correspond

to nearest neighbor shells within a distance of  $a_0$ ,  $1.414a_0$  and  $1.658a_0$ ; and contain 14, 26 and 50 atoms, respectively.

The following observations can be extracted from both figures:

- All meshes display negative thermal expansion behavior up to temperatures of approximately  $500\text{ K}$  ( $20a_0 \times 20a_0 \times 20a_0$ ) or  $1000\text{ K}$  ( $30a_0 \times 30a_0 \times 30a_0$ ).
- From that temperature onwards, all meshes remain insensitive to temperature, resulting in zero thermal expansion coefficients  $\alpha$ .
- Increasing coarsening results in a more pronounced thermal contraction. Cluster size has little or no effect for low values of  $n'_h$ , while large variations appear for coarse meshes. However, these variations seem uncorrelated with the cluster size.

In other words, the thermal expansion behavior of coarse EAM Ta only likens that of atomistic systems for temperatures below 300K (where the interatomic potential is known to be incorrect). At higher temperatures, the  $a_0$ - $T$  simulations display very little structure and give zero thermal expansion coefficients. Thus, there is no basis to carry out an analysis such as the one presented in Fig. 2.6 for Al.

### 2.2.2.2 Thermal Expansion within the Quasiharmonic Approximation

For consistency, we next calculate the thermal expansion coefficients  $\alpha_{\text{PBC}}$  and  $\alpha_{\text{FS}}$  for periodic and finite atomistic crystals within the quasiharmonic approximation. We study a periodic (infinite)  $7a_0 \times 7a_0 \times 7a_0$  crystal containing 686 atoms, and a  $12a_0 \times 12a_0 \times 12a_0$  finite crystal containing 3925 atoms, which yields the largest possible diagonalizable dynamical matrix.

As in Section 2.2.1.2, from these data we calculate  $\alpha$  for Ta within the quasiharmonic approximation. This gives rise to constant thermal expansion coefficients of  $\alpha_{\text{PBC}} = 7.30 \times 10^{-7}$  and  $\alpha_{\text{FS}} = -2.42 \times 10^{-7}\text{ K}^{-1}$ , respectively. These coefficients are substantially different from those corresponding to periodic-MD and finite QC-dynamic calculations. In fact,  $\alpha_{\text{PBC}}$  corresponds to a temperature of  $364\text{ K}$  for the MD system in Fig. 2.8, while  $\alpha_{\text{FS}}$  corresponds to temperatures of

531  $K$  and 497  $K$  for the 17261 and 56791-atom systems, respectively (both within the anomalous temperature region of the potential). This suggests that the quasiharmonic approximation is not satisfactory for EAM Ta. Indeed, MacDonald and Shukla had already noted the difficulties of replicating the thermal expansion behavior of refractory metals such as Ta using atomistic calculations with central force potentials [51].

A quasiharmonic analysis of mesh and cluster effects in Ta, such as that performed for Al, is therefore not warranted in this case, since not even the atomistic behavior is captured. We simply conclude that the thermal expansion behavior of EAM Ta displays a complex temperature dependence and that the quasiharmonic approximation is only valid in the low temperature regime, where EAM Ta behaves anomalously in any event. Of course, we do not discount other potentials for Ta (perhaps including angular terms [52], or fitted to thermal expansion data [53]) from offering a more satisfactory behavior for coarse meshes. However, an analysis of different interatomic potentials is not the subject of this work and we leave this comparison for future studies.

## 2.3 Discussion

The objective of this chapter was the study of non-equilibrium, thermally-activated processes such as heat transfer. To this end, we have proposed a (fully anharmonic) dynamic version of the Quasicontinuum method based on Brownian dynamics and modeled via a Langevin equation. In order to assess the prospective capabilities of this framework in terms of information transmission across scales, we have studied the phonon impoverished spectra in coarse regions and the resulting underestimation of thermal equilibrium properties.

Our metric of choice to quantify the entropic loss stemming from mesh coarsening has been the thermal expansion coefficient  $\alpha$ , as all frequencies participate in thermal expansion. For Al (in the atomistic limit) our method recovers the atomistic  $\alpha$ —as given by the interatomic potential employed— and produces coarse thermal expansion coefficients that obey the relation:

$$\alpha(n'_h) \approx \frac{1.53 \times 10^{-5}}{n'_h} \approx \frac{N_h}{N} \alpha_{\text{at}} \quad (2.45)$$

This linear dependence with the number of nodes  $N_h$  (or inverse with the mesh size) permits the use of rescaling coefficients to account for the vibrational entropy loss. For example, to compute ensemble averages at temperature  $T$  in a mesh  $(N, N_h, r_c)$ , one would first calculate the corresponding  $\alpha(n'_h)$  from eq. (2.45). Then, the equivalent temperature at which that mesh would reproduce the full thermal behavior could be obtained by:  $T' = T\alpha_{\text{at}}/\alpha'$ .

For Ta, the anomalies of the interatomic potential employed result in negative and zero thermal expansion at low and high temperatures, respectively.

In the QC formulation considered here [9], nodal forces are computed from rigid clusters that do not contribute to the system's entropy. Therefore, entropic losses in coarse meshes are mainly due to a reduced configurational space. To mitigate this shortcoming, nodal forces could be calculated from the derivatives of the free energy –rather than from the potential energy, see eq. (2.7)– at the cluster level. The free energy could be built assuming a quasi or local harmonic approximation [54]. Another venue would be to use the anharmonic *max-ent* method proposed by Kurkarni et al. [29].

## 2.4 Appendix I: Derivation of the Free Energy Expression

We start from the expression for the partition function of a system of distinguishable particles, eq. (2.34),

$$Z_h(\theta, T) = \frac{1}{h^{3N_h}} \int \exp \left[ -\frac{\mathcal{H}_h(\mathbf{q}_h, \mathbf{p}_h, \theta)}{k_b T} \right] d\mathbf{q}_h d\mathbf{p}_h \quad (2.46)$$

Integration over momenta gives:

$$Z_h(\theta, T) = \left( \frac{2\pi m_h k_b T}{h^2} \right)^{\frac{3N_h}{2}} \int \exp \left[ -\frac{V(\mathbf{q}_h, \theta)}{k_b T} \right] d\mathbf{q}_h \quad (2.47)$$

Hence, the free energy of the system can be written as

$$\begin{aligned} F_h(\theta, T) &= -k_b T \ln Z(\theta, T) \\ &= -k_b T \ln \left[ \int \exp \left( -\frac{V(\mathbf{q}_h, \theta)}{k_b T} \right) d\mathbf{q}_h \right] - \left( \frac{3k_b T N_h}{2} \right) \ln \left[ \frac{2\pi m_h k_b T}{h^2} \right] \end{aligned} \quad (2.48)$$

To compute the first term in the r.h.s. –also known as *configuration integral*– we assume  $V$  admits a harmonic representation (we repeat eq. 2.20 for simplicity)

$$V(\mathbf{q}_h, \theta) = V(\mathbf{Q}_h, 0) + \frac{1}{2} (\mathbf{q}_h - \mathbf{Q}_h)^T \mathbf{K}(\mathbf{Q}_h, 0) (\mathbf{q}_h - \mathbf{Q}_h) \quad (2.49)$$

Equation (2.48) then becomes:

$$\begin{aligned} F_h(\theta, T) &= -k_b T \ln \left[ \int \exp \left( -\frac{V(\mathbf{Q}_h, 0) + \frac{1}{2} (\mathbf{q}_h - \mathbf{Q}_h)^T \mathbf{K}(\mathbf{Q}_h, 0) (\mathbf{q}_h - \mathbf{Q}_h)}{k_b T} \right) d\mathbf{q}_h \right] - \\ &\quad \left( \frac{3k_b T N_h}{2} \right) \ln \left[ \frac{2\pi m_h k_b T}{h^2} \right] \\ &= V(\mathbf{Q}_h, 0) - k_b T \ln \left[ \int \exp \left( -\frac{\mathbf{u}_h^T \mathbf{D}(\mathbf{Q}_h, 0) \mathbf{u}_h}{2k_b T} \right) d\mathbf{u}_h \right] - \left( \frac{3k_b T N_h}{2} \right) \ln \left[ \frac{2\pi m_h k_b T}{h^2} \right] \end{aligned} \quad (2.50)$$

where  $\mathbf{u}_h = \mathbf{M}_h^{\frac{1}{2}} (\mathbf{q}_h - \mathbf{Q}_h)$  are the *mass-weighted displacements*. By virtue of eq. (2.25), eq. (2.50) can be reduced to:

$$F_h(\theta, T) = V(\mathbf{Q}_h, 0) - \left( \frac{3k_b T N_h}{2} \right) \ln \left[ \frac{2\pi m_h k_b T}{h^2} \right] - k_b T \ln \left[ \int \prod_i^{3N_h} \exp \left( -\frac{\omega_i^2(\theta) y_{h,i}^2}{2k_b T} \right) dy_{h,i} \right] \quad (2.51)$$

In addition, after the following change of variable  $x_i = \omega_i(\theta) y_{h,i} / \sqrt{2k_b T}$ , the integral term evaluates to:

$$\begin{aligned} F_h(\theta, T) &= V(\mathbf{Q}_h, 0) - \left( \frac{3k_b T N_h}{2} \right) \ln \left[ \frac{2\pi m_h k_b T}{h^2} \right] - k_b T \sum_i^{3N_h} \ln \left[ \frac{\sqrt{2\pi k_b T}}{\omega_i(\theta)} \right] \\ &= V(\mathbf{Q}_h, 0) - \left( \frac{3k_b T N_h}{2} \right) \left[ \ln \left( \frac{2\pi m_h k_b T}{h^2} \right) + \ln(2\pi k_b T) \right] + k_b T \sum_i^{3N_h} \ln(\omega_i(\theta)) \end{aligned} \quad (2.52)$$

which, after operating slightly, is the final form for the free energy given in eq. (2.35)

## 2.5 Appendix II: The Embedded Atom Method

The Embedded Atom Method (EAM) is a semi-empirical energy model that relies on parameterized expressions, whose parameters are related to material properties that can be determined experimentally. In this way the method has a solid theoretical basis but is also anchored to accurately known material properties. The starting point of the EAM is the observation that the total electron density in the vicinity of a given atom can be thought of as the atomic density of the atom in question plus an electron density from the surrounding atoms. Then, there is an additional energy contribution from the electrostatic energy due to core-core overlap. In other words, the bond energies depend not only on the distance between atom  $i$  and  $j$  but also on the number and identity of their respective neighbors [55–57]:

$$\begin{aligned}
 V(\mathbf{q}) &= \sum_{i=1}^N F(\rho_i) + \frac{1}{2} \sum_{i=1}^N \sum_{j=1}^Z \Phi(r_{ij}) \\
 \rho_i &= \sum_{j=1}^Z f(r_{ij}) \quad r_{ij} = |\mathbf{q}_i - \mathbf{q}_j|
 \end{aligned}
 \tag{2.53}$$

where the pair potential  $\Phi(r_{ij})$  represents the energy due to electrostatic interactions between an atom and each of its neighbors,  $\rho_i$  describes the electron density that atom  $i$  feels due the environment, the many-body term –containing  $F(\rho_i)$ – accounts for the energy release upon embedding atom  $i$  in the local electron density  $\rho_i$ ,  $Z$  is the number of neighbors contributing to that density; and  $f(r_{ij})$  is the electron density at site  $i$  due to atom  $j$  as a function of the distance between them  $r_{ij}$ .

The separation into a pairwise interaction energy  $\Phi(r)$  and a non-linear embedding energy  $F(\rho)$  can be derived starting from the expression for the cohesive energy of a solid according to Density Functional Theory and by introducing two basic assumptions. The first assumption is that the embedding energy  $F$  can be written as a function of the local electron density  $\rho(r)$ . The second assumption is that this electron density can be approximated by the linear superposition of individual atoms' densities  $f(r)$ . The first assumption is justified by studies of the nearly uniform electron gas, while the second is reasonable provided covalent bonding effects are negligible. This naturally limits

the range of applicability to simple metals and late and early transition metals [57].

First principle calculations gave –in turn– the following important information about the general behavior of these functions. The embedding energy  $F(\rho)$  must go to zero at zero electron density  $\rho(r)$  and should have a negative slope and positive curvature for metals. In addition, the pair interaction term  $\Phi(r)$  should be purely repulsive. Thus, different authors assume different functional forms that meet these general conditions and adjust the parameters to fit known properties of materials.

### 2.5.1 Force Matching Method - Aluminum and Tantalum Potentials

The *Force Matching Method* was developed by Ercolessi and Adams [47] to obtain empirical potentials from both experimental results and a large amount of first principle calculations (positions and forces). If  $\{\alpha\}$  indicates the  $L$  parameters used to characterize the functions  $F(\rho)$ ,  $\Phi(r)$  and  $f(r)$ , the optimal set  $\{\alpha^*\}$  is determined by matching the forces supplied by first principles calculations with those predicted by the classical potential. The matching is performed by minimizing the objective function  $Z(\alpha)$ :

$$\begin{aligned}
 Z(\alpha) &= Z_F(\alpha) + Z_C(\alpha) \\
 Z_F(\alpha) &= \left( 3 \sum_{k=1}^M N_k \right)^{-1} \sum_{k=1}^M \sum_{i=1}^{N_k} |\mathbf{F}_{ki}(\alpha) - \mathbf{F}_{ki}^0|^2 \\
 Z_C(\alpha) &= \sum_{r=1}^{N_C} w_r (A_r(\alpha) - A_r^0)^2
 \end{aligned} \tag{2.54}$$

where  $M$  is the number of sets of atomic configurations available,  $N_k$  is the number of atoms in configuration  $k$ ,  $\mathbf{F}_{ki}(\alpha)$  is the force in atom  $i$  of set  $k$  as obtained with parametrization  $\alpha$ , and  $\mathbf{F}_{ki}^0$  is the reference force from first principles. In addition,  $Z_C$  contains contributions from  $N_C$  additional constraints.  $A_r(\alpha)$  are physical quantities obtained with parametrization  $\alpha$ .  $A_r^0$  are the corresponding reference quantities, which may be supplied either from first principles calculations or directly from experiments.  $w_r$  are weights chosen at convenience. Input data usually comes from different geometries and physical situations (clusters, surfaces, bulk, defects, etc) to achieve a good potential transferability. The functions  $F(\rho)$ ,  $\Phi(r)$  and  $f(r)$  are described using third-order

polynomials (cubic splines) that connect the  $\alpha$  set and preserve continuity of the functions and their first two derivatives across the junctions.

For aluminum, Ercolessi and Adams [47] parameterized the functions using 40 parameters: 14 for  $\Phi(r)$  and  $\rho(r)$ , and 12 for  $F(\rho)$ . First principle data were obtained from Density Functional Theory (DFT) calculations. They processed  $M = 85$  set of atomic configurations and  $N_C$  additional constraints, of which 8 for the cohesive energy  $E_c$ , the equilibrium lattice spacing  $a_o$ , the (unrelaxed) vacancy formations energy  $E_{UF}$ , the unrelaxed (111) stacking fault energy, the (unrelaxed) surface energy, the bulk modulus  $B$  and the shear moduli  $C_{11} - C_{12}$  and  $C_{44}$ ; and 22 to fit energy and pressure to the universal equation of state proposed by Rose et al. [58] at 11 different lattice spacings ( $a/a_o = 0.90, 0.94, 0.97, 1.05, 1.11, 1.20, 1.30, 1.40, 1.50, 1.60, 1.75$ ). The weights  $w_r$  assigned to the constraints and the cut-off radius  $R_c$  for  $\Phi(r)$  and  $\rho(r)$  were adjusted by a trial-and-error procedure. The cut-off radius is  $r_c = 5.56 \text{ \AA}$  for both electron density and pair potential.

For tantalum, Li et al. [50] fitted experimental values of lattice constant  $a_o$ , cohesive energy  $E_c$ , (unrelaxed) vacancy formation energy  $E_{UF}$ , bulk modulus  $B$ , and elastic constants  $C_{11}$ ,  $C_{12}$  and  $C_{44}$ . In addition, they also took into account data from the Rose et al. [58] equation of state for various contractions and expansions of the unit cell ( $a/a_o = 0.90, 0.94, 0.97, 1.05, 1.11, 1.20, 1.30$ ). For each function the authors chose 23 parameters, with a cutoff radius of  $3.987 \text{ \AA}$  for both electron density and pair potential. This distance is halfway between the second and third nearest neighbor distances and is reasonable for bcc metals, where second neighbors must be considered due to the nonclosely packed structure of the material.

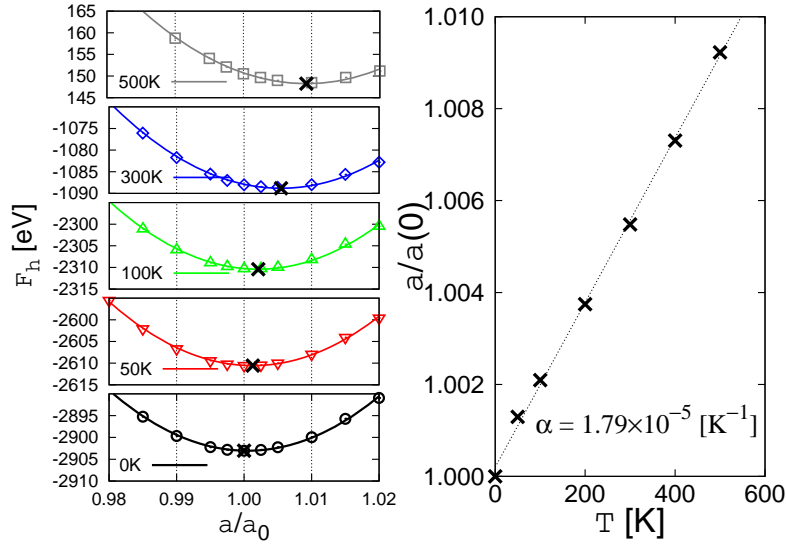
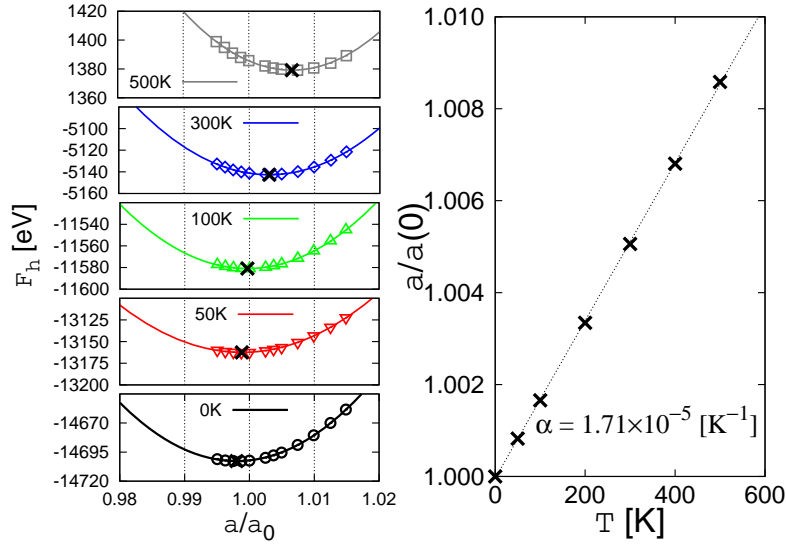
(a) Bulk (periodic)  $10a_0 \times 10a_0 \times 10a_0$  cell.(b) Finite (constrained surfaces)  $10a_0 \times 10a_0 \times 10a_0$  cell.

Figure 2.7: (Left) Free energy vs normalized lattice parameter for fully atomistic Al systems. The minima of the fitted 2<sup>nd</sup>-order polynomials (marked with a black 'x') are the equilibrium lattice parameter at each temperature, normalized to the bulk  $a_0$  of 4.032 Å. (Right) Temperature dependence of the equilibrium lattice parameter. The derivative of the linear fit to the data gives the thermal expansion coefficient  $\alpha$ .

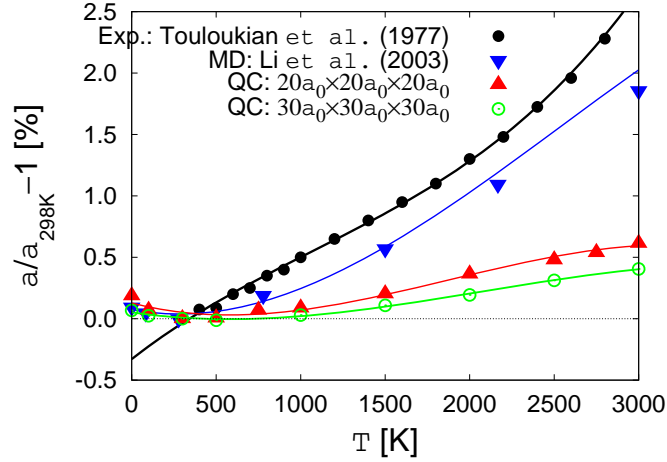


Figure 2.8: Thermal expansion behavior of Ta. Solid dots correspond to experimental data given by Touloukian et al. [44]. Inverted triangles are periodic MD calculations performed by Li et al. [50]. Solid triangles and open dots correspond to QC dynamic simulations for finite  $20a_0 \times 20a_0 \times 20a_0$  and  $30a_0 \times 30a_0 \times 30a_0$  systems. Finally, solid lines are third-degree polynomial fits to the data.

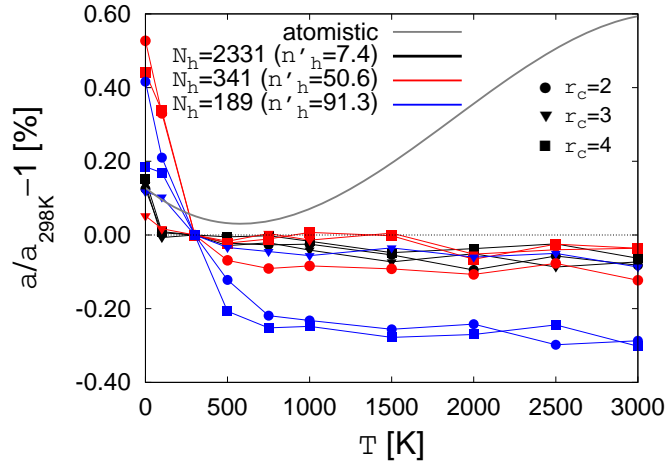


Figure 2.9: Thermal expansion behavior of the  $20a_0 \times 20a_0 \times 20a_0$  system (17261 lattice sites). Three meshes and three cluster sizes were considered. All meshes show negative thermal expansion until approximately 500K, at which point the lattice parameter becomes independent of  $T$  ( $\alpha = 0$ ). We recall that  $n'_h = N/N_h$  is the *effective nodal weight*.

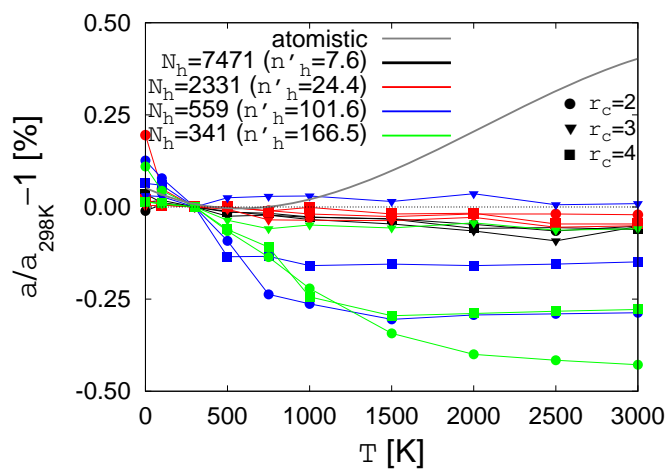


Figure 2.10: Thermal expansion behavior of the  $30a_0 \times 30a_0 \times 30a_0$  system (56791 lattice sites). Four meshes and three cluster sizes were considered. All meshes show negative thermal expansion until approximately 1000K, after which the lattice parameter becomes independent of  $T$  ( $\alpha = 0$ ).

## Chapter 3

# Equilibrium Mean-Field Framework for Alloys at Finite Temperature

The objective of this chapter is to obtain effective thermodynamic potentials while avoiding the treatment of all the system's atomic degrees of freedom. By restricting ourselves to the study of multi-species crystalline materials at finite temperature, the idea is to account for the energy contained in thermal oscillations and for the contribution of different components without the knowledge of the instantaneous velocity of such vibrations or the specific identity of each atom within the lattice. The ultimate goal is the development of a framework to simulate slow processes (such as corrosion or segregation of impurities) where the evolution occurs over time-windows that are intractable for the existing atomistic or atomistic-informed models. The first step in that direction is to build a model able to assess the effect of composition on material properties. In this chapter we present an extension of the work by Kulkarni et al. [4] to treat alloys at finite temperature. We validate the model against experimental measurements, such as lattice parameter, thermal expansion coefficient, elastic constants and surface segregation profiles. A non-equilibrium framework based in this model will be developed in the next chapter.

This chapter is organized as follows. Section 3.1 provides a concise review of the statistical mechanics fundamentals for atomistic systems containing multiple species. In Section 3.2 we use this variational formulation to obtain *maximum entropy* probability distribution functions for binary alloys. The derivation of effective thermodynamic potentials is presented in Section 3.3. Section 3.4

addresses the mean field treatment of interactions among different species. In Section 3.5 we particularize our formulation for systems in thermal equilibrium. We validate the proposed framework against experimental results in Section 3.6.

### 3.1 General Framework

Atomistic computer simulations have been employed for the past thirty years to determine structural and thermodynamic (equilibrium) properties of solids and their defects over a wide range of temperature and pressure. The traditional Monte Carlo (MC) and Molecular Dynamics (MD) methods, while ideally suited to these calculations, require appreciable computational resources in order to calculate the long-time averages from which properties are obtained [59, 60].

In order to overcome this disadvantage and thereby permit a reasonably quick, but accurate determination of the equilibrium properties of interest, the so called *Free Energy Minimization Method* (FEMM) [59, 61] was introduced to find thermodynamic properties of solids, including those with defects. The essence of this method is to write down a functional form for the free energy of the system in terms of microscopic variables such as the average atomic coordinates and atomic site occupancies (for a given temperature, pressure and set of chemical potentials), and to minimize this functional form by using the derivatives of the free energy with respect to the microscopic variables [59].

Aligned with the FEMM described above, the basic idea of this chapter is to obtain effective macroscopic thermodynamic potentials while avoiding the treatment of all the system's atomic degrees of freedom (position, momentum and identity). In this context the term *system* will denote a multi-species crystalline material allowed to exchange thermal energy and matter with the environment. In particular we wish to account for the energy contained in the thermal oscillations of the atoms and for the contribution of different species without solving the instantaneous atomic velocity of such vibrations or tracking the specific identity of each atom within the lattice.

The main differences between the FEMM and the framework we are about to present is that the later does not assume the system has reached equilibrium. In fact the effective potentials found

in this chapter (Helmholtz free energy  $F$ ) will be used in Chapter 4 to simulate out-of-equilibrium phenomena such as mass transfer. In addition, our method doesn't rely on a harmonic (or quasi-harmonic) treatment of atomic vibrations. Finally, we don't introduce any particular form of the configurational entropy as is done in FEMM [62, 63]. The functional dependence of this quantity emerges as an outcome of our model instead.

Owing to its origins in the *maximum entropy* principle, the method that follows is usually referred to as the max-ent method [4]. The key distinction of this approach from classical statistical thermodynamics is that local (instead of global) constraints are imposed. This allows us to derive local forms of the thermodynamic potentials which will become useful for the modeling of non-equilibrium phenomena.

In order to build local forms of thermodynamic potentials the system is split into a collection of subsystems (lattice sites) small enough for them to be close to equilibrium. All variables defined in equilibrium thermodynamics remain uniform within each subsystem but they take different values from cell to cell. Then each lattice site is allowed to have its own local concentration, temperature and chemical potential.

Consider a substitutional solid solution comprising  $N$  lattice sites, each of which can be occupied by one of  $M$  atomic species. From statistical mechanics, the value of any thermodynamic variable results from averaging over the configurations available to such a system:

$$\langle f \rangle = \sum_{\epsilon_1=0}^{M-1} \dots \sum_{\epsilon_N=0}^{M-1} \frac{1}{h^{3N}} \int_{-\infty}^{\infty} f p(\mathbf{q}, \mathbf{p}, \epsilon_1, \dots, \epsilon_N) d\mathbf{q}d\mathbf{p} \quad (3.1)$$

where  $(h^{3N})^{-1}$  is the natural unit of phase volume,  $h$  is Planck's constant and the usual  $(N!)^{-1}$  factor is missing because the system consists of *distinguishable* entities<sup>1</sup> [40, 64]. The label operator

---

<sup>1</sup>Since atoms vibrate about a given lattice site (that could be labeled), the system consists of *distinguishable* units.

used in expression (3.1) describes the species sitting at each lattice site according to,

$$\epsilon_i = \begin{cases} 0 & \text{if site } i \text{ is occupied by a particle of type 1} \\ 1 & \text{if site } i \text{ is occupied by a particle of type 2} \\ \dots & \\ M-1 & \text{if site } i \text{ is occupied by a particle of type M} \end{cases} \quad i = 1..N \quad (3.2)$$

In addition,

$$d\mathbf{q}d\mathbf{p} = \prod_{i=1}^N \prod_{j=1}^3 dq_{ij} dp_{ij} \quad N = \sum_{k=0}^{M-1} N_k \quad N_k = \sum_{i=1}^N x_{k,i} \quad (3.3)$$

where  $d\mathbf{q}|d\mathbf{p}$  refers to the complete array of lattice site's position|momenta.

The term *configuration* denotes a specific realization of all microscopic variables describing the system; and in this context comprises the instantaneous position  $(\mathbf{q}_i)_{i=1}^N$  momenta  $(\mathbf{p}_i)_{i=1}^N$  and species identity  $(\epsilon_i)_{i=1}^N$  of all atoms within the lattice. Not all configurations are equally likely. The probability with which each one occurs is described by the probability distribution function of the system  $p$ . Then, in order to calculate any thermodynamic variable using eq. (3.1) the first step is to construct a suitable  $p = p(\mathbf{q}, \mathbf{p}, \epsilon_1, \dots, \epsilon_N)^2$ .

The formulation that follows has no restrictions regarding the number of atomic species  $M$  that could be treated. For simplicity, however, we will restrict ourselves to binary systems,  $M = 2$ , where the label operator defined by eq. (3.2) becomes

$$\epsilon_i = \begin{cases} 1 & \text{if site } i \text{ is occupied by a particle of type A} \\ 0 & \text{if site } i \text{ is occupied by a particle of type B} \end{cases} \quad (3.4)$$

## 3.2 Building a Suitable Probability Distribution

As discussed in the previous section, the first step to calculate equilibrium quantities is to build a probability distribution  $p$  describing the likelihood of the different microstates available to the

---

<sup>2</sup>From this point forward the symbols  $\mathbf{q}|\mathbf{p}$  will denote the complete array of instantaneous position  $(\mathbf{q}_i)_{i=1}^N$  and momenta  $(\mathbf{p}_i)_{i=1}^N$  respectively.

system. We will accomplish this using a mean field approximation, where the basic idea is to focus the attention on one particle at a time and to treat the interaction with its neighbors as an average field [65].

Within the Information Theory framework, entropy is a measure of the uncertainty contained in the system's statistical distribution [65,66] and is usually defined as:

$$S = - \sum_{\epsilon_1=0}^1 \dots \sum_{\epsilon_N=0}^1 \frac{k_b}{h^{3N}} \int p \ln p \, d\mathbf{q}d\mathbf{p} \quad (3.5)$$

where  $k_b$  is the Boltzmann constant and the total number of sites  $N$  has been assumed constant.

From Information Theory the least biased probability distribution  $p$  can be obtained by maximizing the entropy of the distribution, eq. (3.5). In this work -in addition- the following constraints [29] are imposed to build the dependence of macroscopic potentials (such as the Helmholtz free energy  $F$ ) on *mean* atomistic quantities:

I. The probability distribution satisfies the normalization condition:

$$\sum_{\epsilon_1=0}^1 \dots \sum_{\epsilon_N=0}^1 \frac{1}{h^{3N}} \int p(\mathbf{q}, \mathbf{p}, \epsilon_1, \dots, \epsilon_N) \, d\mathbf{q}d\mathbf{p} = 1 \quad (3.6)$$

II. Each lattice site moves about a mean position  $\langle \mathbf{q}_i \rangle = \bar{\mathbf{q}}_i$  with a linear momentum that oscillates about a mean value  $\langle \mathbf{p}_i \rangle = \bar{\mathbf{p}}_i$ . The variance of these two quantities is assumed equal to  $3\tau_i^2$  and  $3\sigma_i^2$  respectively<sup>3</sup>:

$$\langle |\mathbf{q}_i - \bar{\mathbf{q}}_i|^2 \rangle = 3\tau_i^2 \quad \langle |\mathbf{p}_i - \bar{\mathbf{p}}_i|^2 \rangle = 3\sigma_i^2 \quad i = 1..N \quad (3.7)$$

Defining  $\omega_i = \frac{\sigma_i}{\tau_i}$  and adding the above expressions the following local constrain arises:

$$\langle |\mathbf{p}_i - \bar{\mathbf{p}}_i|^2 \rangle + \omega_i^2 \langle |\mathbf{q}_i - \bar{\mathbf{q}}_i|^2 \rangle = 6\sigma_i^2 \quad i = 1..N \quad (3.8)$$

---

<sup>3</sup>The factor of 3 is included to simplify the subsequent expressions.

where the parameters  $\omega_i$  and  $\sigma_i$  are assumed to be species independent.

III. The mean value of the label operator defined by eq. (3.4) is related to the atomic fraction of species  $A$  by:

$$\langle \epsilon_i \rangle = x_{A,i} \quad i = 1..N \quad (3.9)$$

For binary systems the value of  $x_{B,i}$  is obtained from mass conservation arguments:  $x_{B,i} = 1 - x_{A,i}$ .

Putting everything together, the probability distribution of the system  $p$  can be found by rendering stationary the following entropy functional (this is,  $\delta\Pi/\delta p = 0$ ):

$$\Pi = -\frac{k_b}{h^{3N}} \sum_{\epsilon_1=0}^1 \dots \sum_{\epsilon_N=0}^1 \int \left\{ p \ln p + \lambda p + p \sum_{i=1}^N \beta_i [|\mathbf{p}_i - \bar{\mathbf{p}}_i|^2 + \omega_i^2 |\mathbf{q}_i - \bar{\mathbf{q}}_i|^2] + p \sum_{i=1}^N \gamma_i \epsilon_i \right\} d\mathbf{q}d\mathbf{p} \quad (3.10)$$

where the first term represents the entropy of the distribution (defined in equation 3.5) and the constraints previously described are imposed through Lagrange multipliers ( $\lambda$ ,  $\{\beta\}$  and  $\{\gamma\}$ ). Stationarity yields:

$$p = \frac{1}{Z} \exp \left[ -\sum_{i=1}^N \beta_i (|\mathbf{p}_i - \bar{\mathbf{p}}_i|^2 + \omega_i^2 |\mathbf{q}_i - \bar{\mathbf{q}}_i|^2) - \sum_{i=1}^N \gamma_i \epsilon_i \right] \quad (3.11)$$

where  $Z$  is known as the partition function of the system.

Replacing the above expression in the normalization condition, eq. (3.6), the partition function  $Z$  reduces to:

$$\begin{aligned} Z &= \exp(1 + \lambda) = \\ &= \sum_{\epsilon_1=0}^1 \dots \sum_{\epsilon_N=0}^1 \frac{1}{h^{3N}} \int \exp \left[ -\sum_{i=1}^N \beta_i (|\mathbf{p}_i - \bar{\mathbf{p}}_i|^2 + \omega_i^2 |\mathbf{q}_i - \bar{\mathbf{q}}_i|^2) \right] \exp \left[ -\sum_{i=1}^N \gamma_i \epsilon_i \right] d\mathbf{q}d\mathbf{p} = \\ &= \frac{1}{h^{3N}} \prod_{i=1}^N \left( \sqrt{\frac{\pi}{\beta_i}} \right)^3 \left( \sqrt{\frac{\pi}{\beta_i}} \frac{1}{\omega_i} \right)^3 [1 + \exp(-\gamma_i)] \end{aligned} \quad (3.12)$$

Combining eqs. (3.11) and (3.12) with eq. (3.7) the set of Lagrange multipliers  $\{\beta\}$  takes the form:

$$\beta_i = \frac{1}{2\sigma_i^2} \quad i = 1..N \quad (3.13)$$

Following the same procedure (combining eqs. 3.11, 3.12 and 3.9) the set of Lagrange multipliers  $\{\gamma\}$  becomes,

$$\gamma_i = \ln \left( \frac{1 - x_{A,i}}{x_{A,i}} \right) \quad i = 1..N \quad (3.14)$$

Hence, the final expressions for the max-ent probability distribution and partition function are:

$$\begin{aligned} p(\mathbf{q}, \mathbf{p}, \{\epsilon\}; \bar{\mathbf{q}}, \bar{\mathbf{p}}, \{x_A\}, \{\sigma\}, \{\omega\}) &= \frac{1}{Z} \exp \left[ - \sum_{i=1}^N \frac{|\mathbf{p}_i - \bar{\mathbf{p}}_i|^2 + \omega_i^2 |\mathbf{q}_i - \bar{\mathbf{q}}_i|^2}{2\sigma_i^2} \right] \prod_{i=1}^N \left( \frac{x_{A,i}}{1 - x_{A,i}} \right)^{\epsilon_i} \\ Z &= \frac{1}{h^{3N}} \prod_{i=1}^N \left( \sqrt{2\pi}\sigma_i \right)^3 \left( \sqrt{2\pi}\frac{\sigma_i}{\omega_i} \right)^3 \left( \frac{1}{1 - x_{A,i}} \right) \end{aligned} \quad (3.15)$$

Due to the locality of the imposed constraints, the probability distribution  $p$  and the partition function  $Z$  depend on effective locally-defined variables (the so called *mean field parameters* by [29]) such as mean atomic position  $\bar{\mathbf{q}}_i$ , momenta  $\bar{\mathbf{p}}_i$  and atomic fraction  $x_{A,i}$ . They represent additional unknowns so they will be determined as part of the simulation process. In addition, this dependence on effective *local* atomistic quantities will be inherited by the macroscopic potentials through averaging (see eq. 3.1), which will allow each lattice site to have its own concentration and temperature. The last statement will permit a natural extension of the proposed framework to non-equilibrium processes.

The probability distribution found in this section involves Gaussian functions. Consequently the phase averages may be computed analytically for many functions, or at least numerically while retaining the anharmonic effect of the interatomic potentials in the macroscopic thermodynamic properties. In this work, Gauss quadrature rules that integrate exactly polynomials up to third order would be used. The reader is referred to Appendix I for further details.

As a final remark, note that the probability distribution  $p$  and the partition function  $Z$  emerge as products of terms associated with each lattice site. In statistical thermodynamics this multiplicative form is usually obtained when the system comprises a collection of statistically independent subsystems [40]. In this work, however, the interaction among different subsystems (lattice sites) is embedded in the set  $\{\omega\}$ , which contains the dependence of  $p$  and  $Z$  on the interatomic interactions.

In following sections, each  $\omega_i$  (unspecified so far) will be found to be a function of the complete set of lattice sites.

### 3.3 Thermodynamic Potentials

The partition function  $Z$  derived in previous sections is connected with classic thermodynamics through the thermodynamic potential  $\phi$ :

$$\frac{\phi}{k_b T} = -\ln Z \quad (3.16)$$

being  $\phi$  the function that reaches a minimum when the system attains thermodynamic equilibrium [67].

A closed system (i. e., one in which  $N$ ,  $N_A$  &  $N_B$  remain constant) allowed to exchange thermal energy with the environment is best described within the Canonical framework, where the relevant potential  $\phi$  is the Helmholtz free energy  $F$ :

$$F = U - TS \quad (3.17)$$

Here  $U$  and  $T$  denote internal energy and temperature respectively.

In contrast, a binary non-reactive system able to transfer/receive both thermal energy and matter to/from the environment is usually studied within the Grand Canonical formalism, where the relevant function  $\phi$  is the Grand Canonical potential  $W$ ,

$$\begin{aligned} W &= U - TS - \mu_A N_A - \mu_B N_B \\ &= U - TS - \Delta\mu N_A \end{aligned} \quad (3.18)$$

Here  $\mu_k$  is the chemical potential of species  $k$ ,  $\Delta\mu$  is the chemical potential difference  $\Delta\mu = \mu_A - \mu_B$  and the second line of eq. (3.18) follows since the number of lattice sites  $N$  has been assumed

constant<sup>4</sup>.

From the previous discussion the equilibrium configuration of a closed lattice system (at finite temperature) can be found by minimizing its Helmholtz free energy  $F$ . For an open system, the Grand Canonical potential  $W$  should be minimized instead. According to the definition of both quantities (3.17, 3.18), however, one first needs to specify the internal energy  $U$ , the entropy  $S$ , and –for an open system– the chemical potential difference  $\Delta\mu$ .

### 3.3.1 Entropy

Replacing the probability distribution and the partition function given by eq. (3.15) in expression (3.5), the integral for the global entropy evaluates to:

$$\begin{aligned} S &= \sum_{i=1}^N \left( 3k_b \ln \left( \frac{\sigma_i^2}{\hbar\omega_i} \right) + 3k_b - k_b x_{A,i} \ln x_{A,i} - k_b x_{B,i} \ln x_{B,i} \right) \\ &= \sum_{i=1}^N S_i \end{aligned} \quad (3.23)$$

where the terms involving atomic fractions ( $x_A, x_B$ ) are known collectively as *configurational entropy* and the sum over all sites is consistent with the fact that entropy is an extensive variable.

---

<sup>4</sup>Proof: Consider a system in contact with both a thermal and a particle reservoir at  $T^s = T^r$ ,  $\mu_A^s = \mu_A^r$  and  $\mu_B^s = \mu_B^r$ . Since system plus reservoir form an isolated macrosystem:

$$d(U^s + U^r) = 0 \quad (3.19)$$

If the macrosystem reaches equilibrium through a reversible process,

$$d(S^s + S^r) = 0 \quad (3.20)$$

Combining eqs. (3.19) and (3.20) with the first fundamental relation for a binary system [65]:  $dU = TdS - pdV + \mu_A dN_A + \mu_B dN_B$ ,

$$dU^s - T^r dS^s - \mu_A^r dN_A^s - \mu_B^r dN_B^s = 0 \quad (3.21)$$

where we have assumed conservation of each component within the macrosystem  $-d(N_A^s + N_A^r) = d(N_B^s + N_B^r) = 0$ – and rigid walls  $-dV^s = dV^r = 0$ . Finally, when the system's number of lattice sites is held constant  $-d(N_A^s + N_B^s) = 0$ – eq. (3.21) becomes

$$dU^s - T^s dS^s - \Delta\mu^s dN_A^s = d(U - TS - \Delta\mu N_A) = 0 \quad (3.22)$$

where the superindices have been removed because the reservoir intensive properties ( $\mu_k^r, T^r$ ) remain unchanged through the equilibration process

### 3.3.2 Internal Energy

The internal energy  $U$  is usually defined as the mean value of the Hamiltonian  $\mathcal{H}$  of the system,  $U \equiv \langle \mathcal{H} \rangle$ , where:

$$\mathcal{H} = \frac{1}{2} \mathbf{p}^T \mathbf{M}^{-1} \mathbf{p} + V \quad (3.24)$$

Here first and second terms describe the kinetic and potential contributions, respectively. If the Hamiltonian  $\mathcal{H}$  has an additive structure ( $\mathbf{M}_{k\ell} = m\delta_{k\ell}$ ) the above becomes:

$$\mathcal{H} = \sum_{i=1}^N \left[ \frac{1}{2} \frac{|\mathbf{p}_i|^2}{m_i} + V_i(\mathbf{q}, V^{AA}, V^{AB}, V^{BB}) \right] \quad (3.25)$$

where no localizing approximations has been made since  $V_i(\mathbf{q})$  depends on the entire array  $\mathbf{q}$ . In addition,  $V_i$  accounts for the interatomic interactions among different species through  $V^{AA}$ ,  $V^{AB}$  and  $V^{BB}$ . These quantities result from subatomic (non-resolved) scales of the system, i. e., they play the same role constitutive relations play for continuum models. Therefore, they are an input for this framework. In this work, they will be described by interatomic potentials.

In order not to track the specific identity of each site the Hamiltonian  $\mathcal{H}$  will be approximated by:

$$\mathcal{H} \simeq \sum_{i=1}^N \frac{1}{2\bar{m}_i} |\mathbf{p}_i|^2 + \sum_{i=1}^N V_i(\mathbf{q}, \{x_A\}, V^{AA}, V^{AB}, V^{BB}) \quad (3.26)$$

where  $\bar{m}_i$  denotes a weighted mass:

$$\bar{m}_i = x_{A,i} m_A + x_{B,i} m_B \quad i = 1..N \quad (3.27)$$

Performing the ensemble average of eq. (3.26) the internal energy  $U$  of the system follows<sup>5</sup> [68]:

$$U = \sum_{i=1}^N \frac{1}{2\bar{m}_i} \langle |\mathbf{p}_i|^2 \rangle + \sum_{i=1}^N \langle V_i \rangle (\bar{\mathbf{q}}, \{x_A\}, \{\omega\}, V^{AA}, V^{AB}, V^{BB}) \quad (3.28)$$

---

<sup>5</sup>By computing the ensemble average of the system's Hamiltonian, the interaction energy becomes a function of the atomic mean positions  $\bar{\mathbf{q}}$  –rather than the instantaneous ones  $\mathbf{q}$ – and the set  $\{\omega\}$ ; see eq. (3.1).

Now, in order to evaluate the first term, recall that from eq. (3.7):

$$\begin{aligned} 3\sigma_i^2 &\equiv \langle |\mathbf{p}_i - \bar{\mathbf{p}}_i|^2 \rangle = \langle |\mathbf{p}_i|^2 \rangle - |\bar{\mathbf{p}}_i|^2 \Rightarrow \\ &\Rightarrow \frac{1}{2} \langle |\mathbf{p}_i|^2 \rangle = \frac{1}{2} (3\sigma_i^2 + |\bar{\mathbf{p}}_i|^2) \end{aligned} \quad (3.29)$$

and inverting eq. (3.23),

$$\sigma_i(x_{A,i}, S_i, \omega_i) = \sqrt{\hbar\omega_i} \exp \left[ \frac{S_i}{6k_b} - \frac{1}{2} + \frac{1}{6}x_{A,i} \ln x_{A,i} + \frac{1}{6}x_{B,i} \ln x_{B,i} \right] \quad (3.30)$$

Finally, combining eq. (3.30) with eqs. (3.29) and (3.28), the internal energy  $U$  of a system undergoing a quasi-static process (where  $\bar{\mathbf{p}}_i$  reduces to zero) can be written as:

$$\begin{aligned} U(\bar{\mathbf{q}}, \{x_A\}, \{S\}, \{\omega\}) &= \frac{3}{2} \sum_{i=1}^N \frac{\hbar\omega_i}{\bar{m}_i} \exp \left[ \frac{S_i}{3k_b} - 1 + \frac{1}{3}x_{A,i} \ln x_{A,i} + \frac{1}{3}x_{B,i} \ln x_{B,i} \right] + \\ &+ \sum_{i=1}^N \langle V_i \rangle (\bar{\mathbf{q}}, \{x_A\}, \{\omega\}, V^{AA}, V^{AB}, V^{BB}) \end{aligned} \quad (3.31)$$

### 3.3.3 Closed Systems and the Helmholtz Free Energy

As stated at the end of Section 3.3, one finds the equilibrium configuration of a multispecies closed lattice system at finite temperature by minimizing its Helmholtz free energy  $F$ . This minimization process could in turn be used to compute equilibrium properties. From eqs. (3.31) and (3.17) the Helmholtz free energy reads<sup>6</sup>:

$$\begin{aligned} F(\bar{\mathbf{q}}, \{x_A\}, \{S\}, \{T\}, \{\omega\}) &= \frac{3}{2} \sum_{i=1}^N \frac{\hbar\omega_i}{\bar{m}_i} \exp \left[ \frac{S_i}{3k_b} - 1 + \frac{1}{3}x_{A,i} \ln x_{A,i} + \frac{1}{3}x_{B,i} \ln x_{B,i} \right] + \\ &+ \sum_{i=1}^N \langle V_i \rangle - \sum_{i=1}^N T_i S_i \end{aligned} \quad (3.32)$$

---

<sup>6</sup>Recall:

- 1) the term *system* denotes a substitutional solid solution
- 2) a quasi-static evolution is assumed:  $\bar{\mathbf{p}}_i = \mathbf{0}$
- 3)  $x_{A,i} + x_{B,i} = 1 \quad \forall i = 1..N$
- 4)  $\bar{m}_i = x_{A,i} m_A + x_{B,i} m_B \quad \forall i = 1..N$

where the term  $TS$  was replaced by a sum over lattice sites under the assumption of the local equilibrium hypothesis [4].

Recall that in the process of building the dependence of macroscopic potentials on mean atomistic quantities we have introduced a number of additional unknowns (the so called *mean field* parameters)<sup>7</sup>:  $\bar{\mathbf{q}}_i$ ,  $\bar{\mathbf{p}}_i$ ,  $x_{A,i}$ ,  $S_i$ ,  $T_i$  and  $\omega_i$ ;  $i = 1..N$ . As was explained before, they will be an outcome of the simulation process.

Taking into account that the Helmholtz free energy is the thermodynamic potential that attains a minimum when the system reaches equilibrium [67], the complete problem of finding the equilibrium configuration of a closed binary system undergoing a quasi-static process at finite temperature may be enunciated as

$$\min_{\bar{\mathbf{q}}} \min_{\{x_A\}} \min_{\{S\}} \min_{\{T\}} \min_{\{\omega\}} F(\bar{\mathbf{q}}, \{x_A\}, \{S\}, \{T\}, \{\omega\}) \quad (3.33)$$

Notice that we obtain the ensemble average of the interaction energy  $\langle V_i \rangle$  at site  $i$  by recourse to numerical quadrature, see Appendix I.

### 3.3.4 Open Systems and the Grand Canonical Potential

One finds the equilibrium configuration of a lattice system able to exchange both energy and matter with the environment by minimizing its Grand Canonical potential  $W$ , which from eq. (3.18) reads:

$$\begin{aligned} W(\bar{\mathbf{q}}, \{x_A\}, \{S\}, \{T\}, \{\omega\}, \{\Delta\mu\}) &= \frac{3}{2} \sum_{i=1}^N \frac{\hbar\omega_i}{\bar{m}_i} \exp \left[ \frac{S_i}{3k_b} - 1 + \frac{1}{3}x_{A,i} \ln x_{A,i} + \frac{1}{3}x_{B,i} \ln x_{B,i} \right] + \\ &+ \sum_{i=1}^N \langle V_i \rangle - \sum_{i=1}^N T_i S_i - \sum_{i=1}^N x_{A,i} \Delta\mu_i \end{aligned} \quad (3.34)$$

As was the case for closed systems, the minimization of  $W$  could be used to find some of the system's equilibrium properties.

In closing this section, notice that both the system's Helmholtz free energy  $F$  and Grand Canonical potential  $W$  depend on effective locally-defined variables such as mean atomic position  $\bar{\mathbf{q}}_i$ ,

---

<sup>7</sup>Temperature and entropy are added to the list of parameters because the Helmholtz free energy  $F$  depends on them according to:  $F = U - TS$

temperature  $T_i$  and atomic fraction  $x_{A,i}$ . This implies that the concentration and temperature fields could vary from site to site within the lattice.

### 3.4 Interatomic Interactions

Interaction among different atoms has been unspecified so far. The presented framework is not attached to any particular technique to calculate such interactions (provided they can be computed from the position of the atoms within the system).

In this work we use semi-empirical many-body potentials such as the Embedded Atom Method (EAM) due to their success in accurately describing bulk and surface properties, grain boundaries, internal voids and fracture processes in pure metals [55,56,69].

Accordingly, the potential energy of a single-species system can be written as [55,56]:

$$\begin{aligned}
 V(\mathbf{q}) &= \sum_{i=1}^N F(\rho_i) + \frac{1}{2} \sum_{i=1}^N \sum_{j=1}^Z \Phi(r_{ij}) \\
 \rho_i &= \sum_{j=1}^Z f(r_{ij}) \quad r_{ij} = |\mathbf{q}_i - \mathbf{q}_j|
 \end{aligned}
 \tag{3.35}$$

where the pair potential  $\Phi(r_{ij})$  represents the energy due to electrostatic interactions between an atom and each of its neighbors,  $\rho_i$  describes the electron density that atom  $i$  feels due the environment, the many-body term –containing  $F(\rho_i)$ – accounts for the energy release upon embedding atom  $i$  in the local electron density  $\rho_i$ ,  $Z$  is the number of neighbors contributing to that density; and  $f(r_{ij})$  is the electron density at site  $i$  due to atom  $j$  as a function of the distance between them  $r_{ij}$ .

The main advantage the EAM framework has for alloy modeling is that both the embedding function  $F$  and the electron density function  $f$  depend on the species of atom  $i$ , but are independent of the atom type at the other end of the interaction. Therefore the same functions used for pure metal are suitable for alloys [55,56,69]. Hence, the potential energy of a binary alloy has the following

form [56]

$$\begin{aligned}
V(\mathbf{q}, V^{AA}, V^{AB}, V^{BB}) = & \sum_{i^A=1}^{N_A} F^A(\rho_i) + \frac{1}{2} \sum_{i^A=1}^{N_A} \left( \sum_{j^A=1}^{Z_A} \Phi^{AA}(r_{ij}) + \sum_{j^B=1}^{Z_B} \Phi^{AB}(r_{ij}) \right) + \\
& + \sum_{i^B=1}^{N_B} F^B(\rho_i) + \frac{1}{2} \sum_{i^B=1}^{N_B} \left( \sum_{j^A=1}^{Z_A} \Phi^{BA}(r_{ij}) + \sum_{j^B=1}^{Z_B} \Phi^{BB}(r_{ij}) \right) \quad (3.36)
\end{aligned}$$

where  $i^A|i^B$  indicate summation over type- $A$  and type- $B$  atoms;  $V^{AA}$ ,  $V^{AB}$ ,  $V^{BB}$  generically describe the interactions among atoms of different species and the electron density  $\rho_i$  can be written as

$$\rho_i = \sum_{j^A=1}^{Z_A} f^A(r_{ij}) + \sum_{j^B=1}^{Z_B} f^B(r_{ij}) \quad (3.37)$$

In this work, we don't track the specific identity of each lattice site. Therefore we'll approximate the above formulas by:

$$\begin{aligned}
V(\mathbf{q}, \{x_A\}, V^{AA}, V^{AB}, V^{BB}) = & \sum_{i=1}^N x_{A,i} F^A(\rho_i) + \frac{1}{2} \sum_{i=1}^N x_{A,i} \sum_{j=1}^Z x_{A,j} \Phi^{AA}(r_{ij}) + \\
& + \sum_{i=1}^N \underbrace{x_{B,i}}_{1-x_{A,i}} F^B(\rho_i) + \frac{1}{2} \sum_{i=1}^N x_{B,i} \sum_{j=1}^Z x_{B,j} \Phi^{BB}(r_{ij}) + \\
& + \frac{1}{2} \sum_{i=1}^N \sum_{j=1}^Z (x_{A,i} x_{B,j} + x_{B,i} x_{A,j}) \Phi^{AB}(r_{ij}) \\
\rho_i = & \sum_{j=1}^Z (x_{A,j} f^A(r_{ij}) + x_{B,j} f^B(r_{ij})) \quad (3.38)
\end{aligned}$$

where  $x_A^i|x_B^i$  is the probability of finding an atom of type  $A|B$  at site  $i$  and the following identity  $\Phi^{AB}(r) = \Phi^{BA}(r)$  has been used. Note that the above approximation is only exact for linear terms, i. e., those involving the pair contributions to the potential energy.

Finally, the function describing the interaction energy among atoms in eq. (3.26) can be written

as:

$$\begin{aligned}
V_i(\mathbf{q}, \{x_A\}, V^{AA}, V^{AB}, V^{BB}) = & x_{A,i} F^A(\rho_i) + \frac{1}{2} x_{A,i} \sum_{j=1}^Z x_{A,j} \Phi^{AA}(r_{ij}) + \\
& + x_{B,i} F^B(\rho_i) + \frac{1}{2} x_{B,i} \sum_{j=1}^Z x_{B,j} \Phi^{BB}(r_{ij}) + \\
& + \frac{1}{2} \sum_{j=1}^Z (x_{A,i} x_{B,j} + x_{B,i} x_{A,j}) \Phi^{AB}(r_{ij}) \quad (3.39)
\end{aligned}$$

The reader is referred to Appendix II for further details on the specific functions and empirical parameters used in this work. In addition, details regarding the calculation of the mean interaction energy  $\langle V_i \rangle$  (appearing in eqs. 3.32 and 3.34) can be found in Appendix I.

The numerical examples to be presented in the next section have been obtained using the EAM potentials proposed by [56] for binary fcc alloys.

### 3.5 Systems in Thermal Equilibrium

The formulation presented in Sections 3.3.3 and 3.3.4 allows further simplification for systems in thermal equilibrium.

According to the Equipartition Theorem of classical Statistical Thermodynamics<sup>8</sup>, each quadratic term in the Hamiltonian contributes  $\frac{k_b T}{2}$  to the mean internal energy. From eqs. (3.28) and (3.29):

$$\begin{aligned}
\frac{1}{2\bar{m}_i} \langle |\mathbf{p}_i|^2 \rangle &= \frac{3}{2\bar{m}_i} \sigma_i^2 = \frac{3}{2} k_b T_i \Rightarrow \\
\Rightarrow \sigma_i^2 &= \bar{m}_i k_b T_i \quad (3.40)
\end{aligned}$$

where we have assumed a quasistatic process ( $\bar{\mathbf{p}}_i = \mathbf{0}$ ). Replaced into eq. (3.23) it yields,

$$S_i = 3k_b \ln \left( \frac{\bar{m}_i k_b T_i}{\hbar \omega_i} \right) + 3k_b - k_b x_A^i \ln x_A^i - k_b x_B^i \ln x_B^i \quad (3.41)$$

---

<sup>8</sup>The equipartition theorem becomes inaccurate at low temperatures, when quantum effects are significant. The limit is set by the so called *Debye* temperature  $T_D$ , a collection of constants and material-dependent variables.

According to eq. (3.31) the internal energy  $U$  of a system undergoing a quasi-static process can then be written as:

$$U(\bar{\mathbf{q}}, \{x_A\}, \{T\}, \{\omega\}) = \sum_{i=1}^N \left( \frac{3}{2} k_b T_i + \langle V_i \rangle \right) \quad (3.42)$$

Replacing eqs. (3.41) and (3.42) into eq. (3.32), the Helmholtz free energy  $F$  becomes,

$$F(\bar{\mathbf{q}}, \{x_A\}, \{T\}, \{\omega\}) = \sum_{i=1}^N \langle V_i \rangle - k_b \sum_{i=1}^N T_i \left[ 3 \ln \left( \frac{\bar{m}_i k_b T_i}{\hbar \omega_i} \right) + \frac{3}{2} - x_{A,i} \ln x_{A,i} - x_{B,i} \ln x_{B,i} \right] \quad (3.43)$$

On the other hand, replacing eq. (3.41) into eq. (3.34), the Grand Canonical potential  $W$  turns into,

$$\begin{aligned} W(\bar{\mathbf{q}}, \{x_A\}, \{T\}, \{\omega\}, \{\Delta\mu\}) = & -k_b \sum_{i=1}^N T_i \left[ 3 \ln \left( \frac{\bar{m}_i k_b T_i}{\hbar \omega_i} \right) + \frac{3}{2} - x_{A,i} \ln x_{A,i} - x_{B,i} \ln x_{B,i} \right] + \\ & + \sum_{i=1}^N \langle V_i \rangle - \sum_{i=1}^N x_{A,i} \Delta\mu_i \end{aligned} \quad (3.44)$$

The relation between entropy  $S$  and temperature  $T$ , eq. (3.41), allows us to further simplify eq. (3.33). Then, equilibrium properties of closed two-species systems at finite temperature can be found by solving:

$$\inf_{\bar{\mathbf{q}}} \inf_{\{x_A\}} \inf_{\{T\}} \inf_{\{\omega\}} F(\bar{\mathbf{q}}, \{x_A\}, \{T\}, \{\omega\}) \quad (3.45)$$

An analogous equation for open systems is:

$$\inf_{\bar{\mathbf{q}}} \inf_{\{x_A\}} \inf_{\{T\}} \inf_{\{\omega\}} \inf_{\{\Delta\mu\}} W(\bar{\mathbf{q}}, \{x_A\}, \{T\}, \{\omega\}, \{\Delta\mu\}) \quad (3.46)$$

These two equations will become the tool to calculate equilibrium properties in the next section. Specifically, we will obtain the minimizers by recourse to a non-linear version of the Conjugate Gradient Method.

## 3.6 Equilibrium Mean-Field Framework Validation

In this Section we assess the validity of the model with experimental data of four alloy equilibrium properties. Specifically, in Section 3.6.1 we calculate the lattice parameter variation of nickel-palladium alloys with composition. Then we obtain linear thermal expansion coefficients for two different copper-nickel alloys in Section 3.6.2. The effect of copper concentration on copper-nickel elastic constants is studied in Section 3.6.3. Finally, in Section 3.6.4, we model surface segregation in copper-nickel and silver-gold alloys for different temperatures and surface orientations. All numerical results were obtained using EAM type potentials, see Appendix II for further details.

### 3.6.1 Nickel-Palladium Lattice Parameter

Both nickel (Ni) and palladium (Pd) are fcc metals and form a fcc random solid solution through the entire range of compositions [70]. In this section, the alloy lattice parameter  $a$  was obtained using eq. (3.45) on periodic samples containing 365 lattice sites for different (uniform) values of temperature and Pd concentration. In other words, for prescribed values of Pd atomic percentage ( $\sim x_A$ ) and temperature  $T$ , eq. (3.45) was minimized with respect to the whole set of atomic mean positions  $\bar{\mathbf{q}}$  and mean field parameters  $\{\omega\}$  to find the equilibrium lattice parameter  $a$ .

Fig. 3.1 shows the numerical outcome against single crystal measurements [70] obtained at two different temperatures. Both numerical and experimental results follow a smooth curve as a function of composition, with a considerable positive deviation from Vegard's law ( $a_{AB} = x_A a_A + (1 - x_A) a_B$  where  $a_{AB}$  is the alloy lattice parameter and  $a_A|_{a_B}$  are the lattice parameters of the alloy components). The agreement between the two is fairly good, showing the ability of the model to capture deviations from Vegard's law.

Notice that the pure element lattice parameters don't match exactly the experimental values at room temperature 298 K due to the fact that Johnson's potentials were fitted using room temperature quantities instead of 0 K ones. Consequently, no temperature effects were taken into account in fitting procedures, disregarding entropic and kinetic contributions to the free energy  $F$  at room temperature.

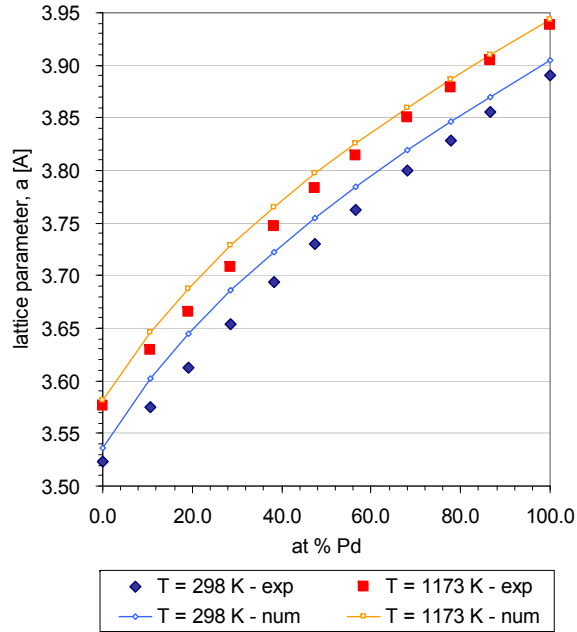


Figure 3.1: NiPd lattice parameter versus Pd atomic percentage at two different temperatures. Experimental [70] single crystal results are included for comparison purposes.

### 3.6.2 Copper-Nickel Thermal Expansion

Both copper (Cu) and nickel (Ni) are fcc metals and form a fcc random solid solution through the entire range of compositions. As was the case in the last section, lattice parameters were obtained using eq. (3.45) on periodic samples containing 666 lattice sites for different (uniform) values of temperature and Cu concentration. From the equilibrium lattice parameter  $a$ , the coefficient of linear thermal expansion  $\alpha$  was found,

$$\alpha = \frac{a - a_{300}}{a_{300}} \quad (3.47)$$

where  $a_{300}$  is the alloy equilibrium lattice parameter at room temperature. Figure 3.2 shows the comparison between numerical and experimental [71] results for two different single crystal CuNi alloys as a function of temperature. Notice that the model is able to capture the difference in thermal expansion that comes with concentration. The error remains below 8% above room temperature.

In order to understand the model limitations, we show thermal expansion coefficients of copper and nickel single crystals in Fig. 3.3 together with their experimental counterparts [71,72]. Since the

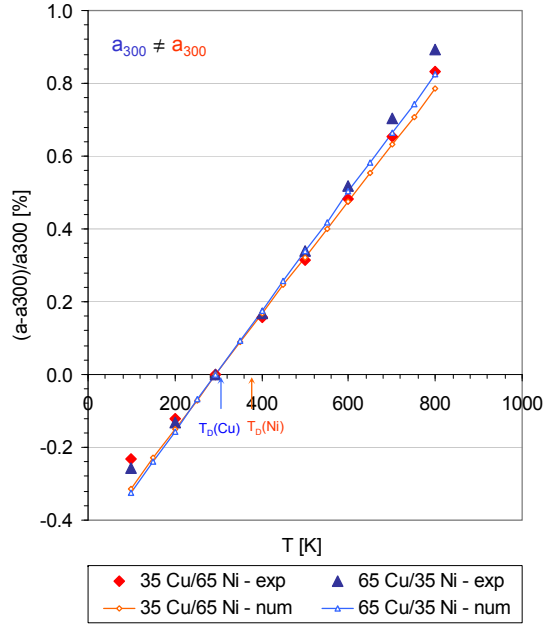


Figure 3.2: Numerical and experimental [71] results of linear thermal expansion in two single-crystal CuNi alloys as a function of temperature. Color arrows indicate the Debye temperature of the pure alloy components.

presented framework is based on classical thermodynamics, it cannot capture the low temperature behavior observed experimentally, see Fig. 3.3. This is expected because the contribution of quantum effects to the lattice vibration energy becomes dominant at low temperatures. In particular, recall that this section's numerical results were obtained using the Equipartition of Energy (eq. 3.40) to relate temperature  $T$  and entropy  $S$ , which is not valid below the *Debye* temperature. Numerical results remain within 10% error for temperatures as high as 70% of the melting point for both metals. As was explained by [4] –who studied thermal properties of single-species samples using a similar framework– the disagreement observed beyond that point is related to the fact that oscillation of different lattice sites was assumed to be only weakly correlated (see eq. 3.7), which is not valid as the material approaches its melting point. From the previous discussion it follows that the same limitations the model has for single-species samples are inherited by alloys.

As a final remark, notice that the higher thermal expansion observed in Cu-rich samples both numerically and experimentally in Fig. 3.2 is consistent with the results of Fig. 3.3, where it is clear that pure copper has a higher thermal expansion coefficient than nickel.

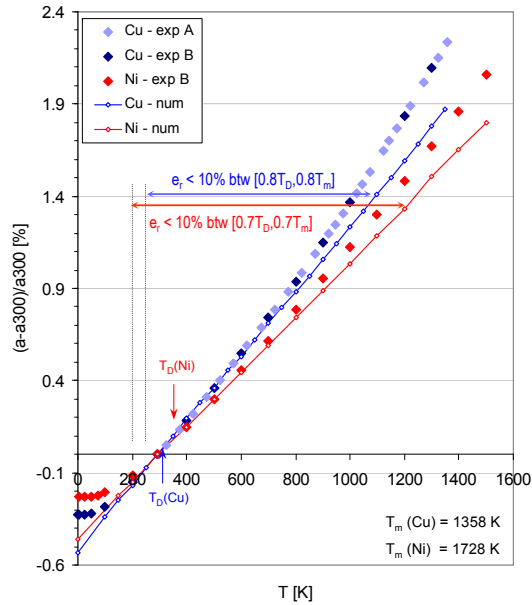


Figure 3.3: Numerical and experimental results (A: [72], B: [71]) of linear thermal expansion in single crystal copper and nickel as a function of temperature.  $T_m$  and  $T_D$  denote the melting point and the *Debye* temperature, respectively.

### 3.6.3 Copper-Nickel Elastic Constants

The energetics of a crystalline system subjected to small deformations can be described in terms of linear elasticity theory. The strain energy stored may be captured via the elastic energy density  $w$ , a local quantity of the form [73]:

$$w(\epsilon) = \frac{1}{2} \sum_{ijkl} C_{ijkl} \epsilon_{ij} \epsilon_{kl} \quad (3.48)$$

where  $C_{ijkl}$  and  $\epsilon_{ij}$  are the elastic moduli and the infinitesimal strain tensor components.

The relation between elastic strain and microscopic degrees of freedom can be built as follows. From the continuum perspective the strain energy density  $w$  is the energy gain (per unit volume  $V$ ) that comes with deformation [73]:

$$w(\epsilon) = \frac{1}{V} (F(\bar{\mathbf{q}}, \epsilon) - F(\bar{\mathbf{q}}, \mathbf{0})) \quad (3.49)$$

where  $F(\bar{\mathbf{q}}, \epsilon)$  is the Helmholtz free energy of the deformed state<sup>9</sup> and  $F(\bar{\mathbf{q}}, \mathbf{0})$  is the free energy of

<sup>9</sup>As was mentioned in previous sections, the total energy of a closed system at finite temperature is best described

the perfect crystal.

Expanding  $F(\epsilon)$  about the unstrained reference state ( $\epsilon = \mathbf{0}$ ) and keeping terms up to second order only,

$$F(\bar{\mathbf{q}}, \epsilon) \approx F(\bar{\mathbf{q}}, \mathbf{0}) + \sum_{ij} \left. \frac{\partial F}{\partial \epsilon_{ij}} \right|_{\epsilon=\mathbf{0}} \epsilon_{ij} + \frac{1}{2} \sum_{ijkl} \left. \frac{\partial^2 F}{\partial \epsilon_{ij} \partial \epsilon_{kl}} \right|_{\epsilon=\mathbf{0}} \epsilon_{ij} \epsilon_{kl} \quad (3.50)$$

On the recognition that the expansion is about the reference state and hence the linear term in the expansion vanishes<sup>10</sup>, the combination of eqs. (3.49) and (3.50) gives [68, 74]

$$C_{ijkl} = \left( \frac{1}{V} \frac{\partial^2 F}{\partial \epsilon_{ij} \partial \epsilon_{kl}} \right) \Big|_{\epsilon=\mathbf{0}} = \frac{\partial^2 w}{\partial \epsilon_{ij} \partial \epsilon_{kl}} \Big|_{\epsilon=\mathbf{0}} \quad (3.51)$$

where the last equality stems from eq. (3.48).

$\mathbf{C}$  is a fourth order tensor with 81 components. Major and minor symmetries of the elastic moduli tensor  $\mathbf{C}$  reduce the number of independent component from 81 to 21. Crystal symmetries further reduce the number of independent components. In particular, cubic crystals (such as fcc or bcc) have only three independent constants [75]:  $C_{11}$ ,  $C_{12}$  and  $C_{44}$ .

By recourse to Voigt notation the elastic energy density (eq. 3.48) can be written as

$$w(\epsilon) = \frac{1}{2} \sum_{\alpha\beta} C_{\alpha\beta} \epsilon_{\alpha} \epsilon_{\beta} \quad (3.52)$$

In addition one could write:  $\epsilon = \gamma\zeta$ , where  $\zeta$  is a symmetric transformation matrix and  $\gamma$  is a scalar measure of the applied strain. It then follows that  $d\epsilon_{ij} = \xi_{ij} d\gamma$ . Then, eq. (3.51) becomes

$$\left( \frac{1}{V} \frac{\partial^2 F}{\partial \gamma^2} \right) \Big|_{\gamma=0} = \frac{\partial^2 w}{\partial \gamma^2} \Big|_{\gamma=0} \quad (3.53)$$

---

by the Helmholtz free energy  $F$

<sup>10</sup>According to hyperelasticity theory  $\frac{\partial F}{\partial \epsilon_{ij}}$  is a measure of stress within the system, so it vanishes in a zero strain configuration provided no residual stresses are considered.

Similarly, the strain energy density  $w$  (eq. 3.52) can be written as

$$w = \frac{1}{2}C_{11}\gamma^2 (\xi_{11}^2 + \xi_{22}^2 + \xi_{33}^2) + C_{12}\gamma^2 (\xi_{11}\xi_{22} + \xi_{22}\xi_{33} + \xi_{11}\xi_{33}) + 2C_{44}\gamma^2 (\xi_{12}^2 + \xi_{23}^2 + \xi_{13}^2) \quad (3.54)$$

To determine the three independent elastic moduli of CuNi alloys, free energies  $F$  corresponding to uniform values of temperature  $T = 300 \text{ K}$  and different values of Cu concentration were obtained on periodic samples containing 365 lattice sites for different deformation states  $\gamma$ . In other words, a homogeneous strain  $\epsilon = \gamma\zeta$  was applied to a system with prescribed values of Cu atomic percentage ( $\sim x_A$ ) and temperature  $T$ . The energy of the deformed state  $F$  was calculated at equally spaced values of  $\gamma$  ranging from  $-0.002$  to  $+0.002$  in steps of  $0.0001$  (negative values of  $\gamma$  were included to account for the anharmonicity of the crystal [75]) by minimizing eq. (3.45) with respect to the set of mean field parameters  $\{\omega\}$ . A fifth-order polynomial was fitted through the calculated energies and the value of the specific elastic constant was extracted from the curvature of this energy curve about the unstrained state  $\gamma = 0$ .

The first of the three independent elastic constants was the bulk modulus  $B$  (which is a linear combination of  $C_{11}$  and  $C_{12}$ ), defined as the inverse of the compressibility  $\kappa$ . The (isothermal) compressibility measures the variation of the crystal volume  $V$  with pressure  $p$ ,

$$\kappa = -\frac{1}{V} \left. \frac{\partial V}{\partial p} \right|_T = \frac{1}{B} \quad (3.55)$$

where  $B$  is the (isothermal) bulk modulus. Combining the first fundamental relation for a binary system [65]:  $dU = TdS - pdV + \mu_A dN_A + \mu_B dN_B$  with the Helmholtz free energy definition:  $F = U - TS$ ,

$$\left. \frac{\partial F}{\partial V} \right|_{T, N_i} = -p \quad (3.56)$$

Then, from eqs. (3.55) and (3.56),

$$B = V \left. \frac{\partial^2 F}{\partial V^2} \right|_{T, N_i} \quad (3.57)$$

which implies that the bulk modulus  $B$  can be obtained by varying the volume of the crystal, i. e., by transforming the basis vectors of the lattice  $\{\mathbf{a}_1, \mathbf{a}_2, \mathbf{a}_3\}$  according to:

$$\mathbf{a}'_i(\gamma) = \mathbf{a}_i + \gamma(\xi \cdot \mathbf{a}_i) \quad (3.58)$$

with  $\xi = \mathbf{I}$  the identity matrix. Taking into account that the volume  $V$  of an unstrained system containing  $n_1 \times n_2 \times n_3$  units cells is given by

$$V(0) = n_1 \mathbf{a}_1 \cdot (n_2 \mathbf{a}_2 \times n_3 \mathbf{a}_3) \quad (3.59)$$

it then follows from eq. (3.58) that:

$$V(\gamma) = (1 + \gamma)^3 V(0) \quad (3.60)$$

and consequently

$$V \frac{\partial^2}{\partial V^2} = -\frac{2}{3} \frac{\partial}{\partial V} + \frac{(1 + \gamma)^2}{9V(\gamma)} \frac{\partial^2}{\partial \gamma^2} \quad (3.61)$$

Finally, combining eqs. (3.56), (3.57) and the last row of eq. (3.61), the bulk modulus  $B$  for a system at zero pressure becomes

$$B = V \left. \frac{\partial^2 F}{\partial V^2} \right|_{T, N_i} = \frac{1}{9V(0)} \left. \frac{\partial^2 F}{\partial \gamma^2} \right|_{T, N_i, \gamma=0} \quad (3.62)$$

The relation between the bulk modulus  $B$  and the set of elastic constants  $\{C_{11}, C_{12}, C_{44}\}$  can be determined as follows. Replacing  $\xi = \mathbf{I}$  into eq. (3.54) the strain energy density  $w$  reads

$$w = 3 \left( \frac{1}{2} C_{11} + C_{12} \right) \gamma^2 \quad (3.63)$$

Combining the last equation with eq. (3.53), the final expression for the bulk modulus (eq. 3.62)

becomes:

$$B = \frac{1}{3}(C_{11} + 2C_{12}) \quad (3.64)$$

Similarly,  $C_{11}$  is related to the free energy curvature for the following transformation matrix:

$$\xi = \begin{bmatrix} 1 & 0 & 0 \\ 0 & 0 & 0 \\ 0 & 0 & 0 \end{bmatrix} \quad (3.65)$$

where, according to eq. (3.54), the elastic energy density  $w$  can be written as

$$w = \frac{1}{2}C_{11}\gamma^2 \quad (3.66)$$

Then, from eq. (3.53):

$$C_{11} = \left. \frac{\partial^2 w}{\partial \gamma^2} \right|_{\gamma=0} = \frac{1}{V(0)} \left. \frac{\partial^2 F}{\partial \gamma^2} \right|_{\gamma=0} \quad (3.67)$$

Finally, the shear modulus  $C_{44}$  describes the elastic energy of volume conserving strains [75] with no diagonal components in  $\epsilon$ . We have calculated this quantity by applying shear on a (100) plane in the  $y$  direction:

$$\xi = \begin{bmatrix} 0 & 1 & 0 \\ 1 & 0 & 0 \\ 0 & 0 & 0 \end{bmatrix} \quad (3.68)$$

in which case, eq. (3.54) becomes

$$w = 2C_{44}\gamma^2 \quad (3.69)$$

and using eq. (3.53),

$$C_{44} = \frac{1}{4} \left. \frac{\partial^2 w}{\partial \gamma^2} \right|_{\gamma=0} = \frac{1}{4V(0)} \left. \frac{\partial^2 F}{\partial \gamma^2} \right|_{\gamma=0} \quad (3.70)$$

The final formulas for the three elastic constants are summarized on Table 3.1.

Figure 3.4 shows numerical and experimental results [72] of elastic constants in single crystal CuNi

Elastic Constant	Transformation Matrix $\xi$	Final Formula
$B = \frac{1}{3}(C_{11} + 2C_{12})$	$\xi = \begin{bmatrix} 1 & 0 & 0 \\ 0 & 1 & 0 \\ 0 & 0 & 1 \end{bmatrix}$	$B = \left( \frac{1}{9V} \frac{\partial^2 F}{\partial \gamma^2} \right) \Big _{\gamma=0}$
$C_{11}$	$\xi = \begin{bmatrix} 1 & 0 & 0 \\ 0 & 0 & 0 \\ 0 & 0 & 0 \end{bmatrix}$	$C_{11} = \left( \frac{1}{V} \frac{\partial^2 F}{\partial \gamma^2} \right) \Big _{\gamma=0}$
$C_{44}$	$\xi = \begin{bmatrix} 0 & 1 & 0 \\ 1 & 0 & 0 \\ 0 & 0 & 0 \end{bmatrix}$	$C_{44} = \left( \frac{1}{4V} \frac{\partial^2 F}{\partial \gamma^2} \right) \Big _{\gamma=0}$

Table 3.1: Elastic Constants calculation

alloys as a function of the copper concentration (at room temperature). Note that even though the potential used to describe the interaction among atoms of different species  $V^{AB}$  was built without fitting any specific alloy property [56] the agreement is excellent for  $C_{11}$  and the Voigt-average shear modulus  $G = \frac{1}{5}(C_{11} - C_{12} + 3C_{44})$ , and remains within 10% error for the bulk modulus  $B$ .

The offset between measurements and numerical values of  $B$  can be rationalized as follows. The interatomic potential we are using constrains the anisotropy ratio  $A = C/C'$  between the cubic shear moduli  $C = C_{44}$  and  $C' = (C_{11} - C_{12})/2$  to be 2 regardless of the atomic species [76]. Thus only two of the three independent elastic constants can be fitted exactly with this EAM potential.

### 3.6.4 Surface Segregation

Surfaces are created by breaking bonds across a plane in a metal crystal, so atoms at the surface have missing bonds with respect to the ones located in the bulk. Surface segregation has three main driving forces. The first one is the lowering of the surface energy. Thus, the element with the lower surface energy will normally segregate to the surface (this is the primary driving force for the systems studied in this section). The segregation is face dependent because the number of out-of-plane neighbors depends on the orientation of the surface. As a consequence, segregation in an fcc lattice is most pronounced at the (110) face, followed by the (100) and is less pronounced at the (111) surface [57]. The second driving force for segregation is the lowering of the total bond

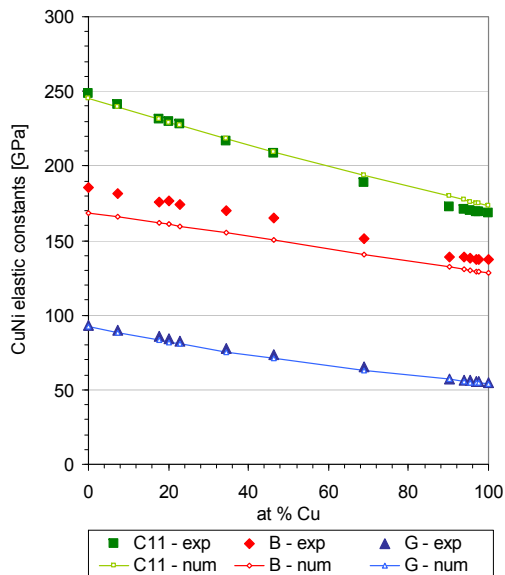


Figure 3.4: Numerical and experimental results [72] of elastic constants in single crystal CuNi alloys as a function of Cu concentration.

energy. When the AB bond has more energy than the average of the AA and BB bonds, there is a preference for AA and BB bonds. Then the corresponding AB repulsions enhance the segregation of the minority component and give rise to a monotonous depth profile. Otherwise, an oscillating depth profile appears [57]. The third driving force pertains to the relaxation of elastic strain energy due to the difference in atomic size between A and B. This effect favors the segregation of the minority component when the size difference exceeds 10% and is important only for larger solute atoms. All of the above savings are partially offset by the decreased randomness of the crystal when atoms of one component are localized on the surface. Therefore segregation in random alloys is always less pronounced at higher temperatures [57].

In the examples presented so far the sample had a (uniform) prescribed concentration. The final case of this chapter concerns the simulation of surface segregation in random fcc alloys, where composition is allowed to vary from site to site.

One can study segregation phenomena in binary alloys using either the Canonical or the Grand Canonical ensemble. However, when the number of atoms of each component remains unchanged (as is the case within the Canonical ensemble) and since the simulation slab is of limited dimensions,

the surface to bulk ratio is unrealistically large and compositional rearrangements at the surface may have a large influence on the bulk composition [57]. Alternatively, the Grand Canonical ensemble can be used. A constant bulk composition is then maintained by imposing the correct difference in chemical potential  $\Delta\mu$ , a quantity that is not known *a priori*.

In this work, segregation was studied within the Grand Canonical formalism. The calculations were performed in three steps. First, we determined the properties of the perfect, uniform composition crystal. This was done by choosing a bulk composition and temperature and then minimizing the free energy  $F$  (eq. 3.45) with respect to the set of effective atomic positions  $\bar{\mathbf{q}}$  and mean field parameters  $\{\omega\}$ . The samples were periodic and contained 666 lattice sites. We then differentiated the equilibrium free energy  $F$  with respect to composition  $x_{A,i}$  to obtain the chemical potential difference  $\Delta\mu_i$ . Since at equilibrium the chemical potential for a component is everywhere constant, we fixed all site's chemical potential difference  $\Delta\mu$  at their bulk values [77]. Finally, we introduced the appropriate interface and minimized the Grand Canonical potential  $W$  (eq. 3.46) with respect to the set of effective atomic positions  $\bar{\mathbf{q}}$ , mean field parameters and  $\{\omega\}$  and atomic fractions  $\{x_A\}$ . In this last step, periodic boundary conditions were applied in the direction parallel to the surface, see Fig. 3.5. In addition, atoms within the bottom cell were constrained to the lattice spacing, atomic fraction and mean field parameter of the bulk alloys at equilibrium. The samples were large enough ( $4 \times 4 \times 10$  unit cells) for this boundary condition not to affect the outcome of the simulation, which started from an homogeneous sample at bulk concentration. As a final remark, the composition of each layer in pictures to follow was determined by averaging over all the atomic sites in that layer.

#### 3.6.4.1 Copper-Nickel Results

The interest in the physics and chemistry of CuNi surfaces relies on the enhancement of selectivity and catalytic activity that these alloys present over the pure metals for certain reactions. One of the most important factors controlling these effects is the composition of the upper most layer of the system [78,79]. CuNi alloys are used, for example, in cyclohexane dehydrogenation into benzene [79].

Figure 3.6 shows the Cu surface concentration as a function of its bulk counterpart. Deviations

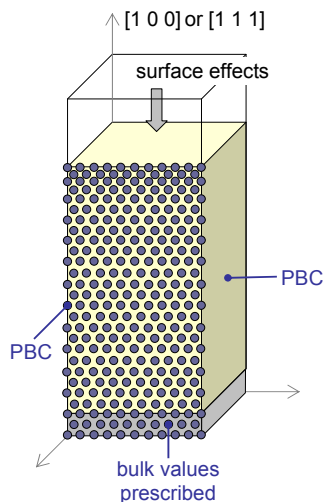


Figure 3.5: Scheme of the sample used to simulate surface segregation phenomena.

from the line  $x_{Cu}^{surface} = x_{Cu}^{bulk}$  indicate segregation. If the surface concentration is above that line, Cu segregates to the surface; if below, the concentration of Ni at the surface is greater than in the bulk. The model is able to predict the effect of temperature and crystal-face orientation on the equilibrium surface concentration.

Our results are consistent with the fact that segregation is more favorable in open surfaces (100). The last statement can be understood by taking into account that the number of broken bonds is 4 for a (100) surface and 3 for the (111) surface. The system tends to compensate the higher number of dangling bonds at the (100) surface by maximizing the number of low-energy Cu broken bonds (the cohesive energy is 3.54 eV for Cu and 4.45 eV for Ni [56]). In addition, we are able to predict that segregation is reduced as temperature increases.

### 3.6.4.2 Gold-Silver Results

The gold (Au)-silver (Ag) system is characterized by a disordered solid solution for the whole range of concentrations [55]. Both metals and their alloys form fcc crystal structures.

Fig. 3.7 shows the numerical outcome against measurements [81,82] obtained for different surface orientations, Ag bulk compositions and temperatures. Notice that both numerical and experimental results follow a damped oscillatory concentration profile, expected for the AgAu system due its

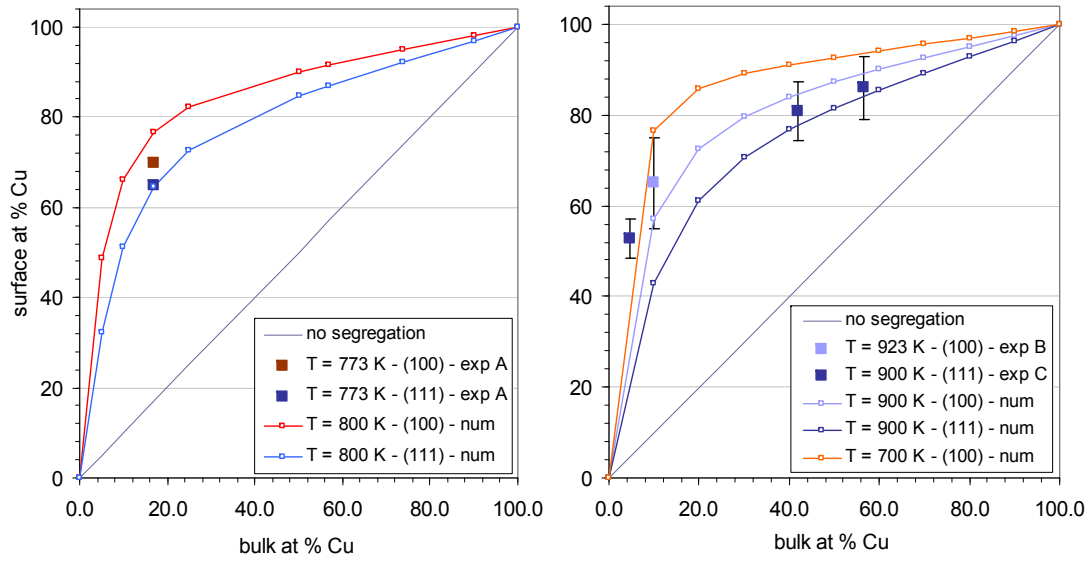


Figure 3.6: Numerical and experimental results (A: [80], B: [78], C: [79]) of surface segregation in CuNi alloys for different surface orientations and temperatures.

negative heat of mixing [57]. The last remark can be rationalized as follows: since the AgAu bond has less energy than the average of the AgAg and AuAu bonds there is a preference for AgAu bonds within the system. Then, when Ag segregates to the surface a second Au rich layer is energetically more favorable.

Overall, the model does a reasonably good job predicting the effect of temperature and surface orientation on the segregation profiles. As depicted in Fig. 3.7, for a given bulk concentration our results are consistent with the fact that segregation is more favorable in open surfaces (100), which are in addition more sensitive to temperature effects (notice that the oscillatory profile is more pronounced for the 100 than for the 111 surface) [81]. Finally, the model anticipates that segregation is reduced with temperature (due to entropy reduction, as explained at the beginning of this chapter), which can be noticed again by the lower crest/valley ratio obtained at 750 K on the left portion of Figure 3.7.

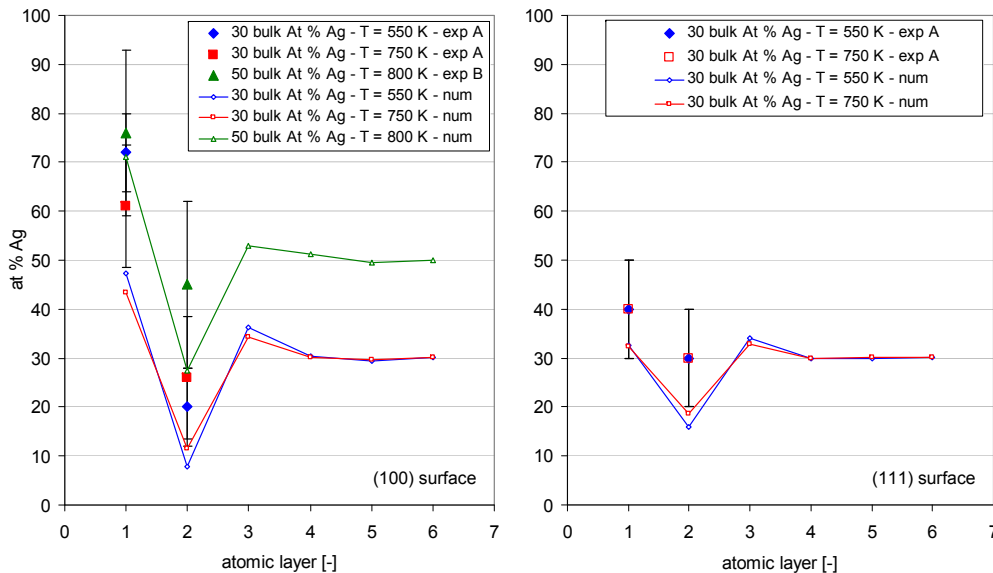


Figure 3.7: Numerical and experimental results (A: [81], B: [82]) of segregation profiles in AgAu alloys for different surface orientations, Ag bulk compositions and temperatures.

### 3.7 Discussion

In this chapter we presented a numerical framework capable of assessing the effect of composition on equilibrium properties for atomistic crystalline alloy systems at finite temperature. Based upon statistical mechanics and mean field theories we built effective local thermodynamic potentials, where concentrations may be viewed as the time-averaged composition of each atomic site in the system. In this sense atoms are *effective* or *mean field* atoms. Equilibrium material properties then followed from minimization. To assert the validity of the model, its ability to reproduce experimental measurements was tested. Specifically, we calculated the lattice parameter variation of nickel-palladium alloys with composition. Then we obtained linear thermal expansion coefficients for two different copper-nickel alloys. Next, we studied the effect that copper concentration has on copper-nickel elastic constants. Finally we simulated surface segregation in copper-nickel and silver-gold alloys for different temperatures and surface orientations. The model predicts (experimental) alloy properties with reasonable accuracy. In addition, since it treats effective rather than instantaneous atomic degrees of freedom, this framework is computationally more efficient than traditional Molecular Dynamics or Monte Carlo methods [59,60].

### 3.8 Appendix I: Numerical Quadrature for Gaussian Functions

As was mentioned previously, the probability distribution  $p$  found in Section 3.2 involves Gaussian functions. Consequently phase averages (eq. 3.1) may be computed analytically for many functions. Due to the difficulty of integrating many-body potentials, however, Gauss quadrature rules [83] will be used to obtain the mean potential energy  $\langle V_i \rangle$  appearing on eqs. (3.32), (3.34), (3.43) and (3.44).

Specifically, we suppose that each function  $V_i$  involves a finite number of neighboring atoms. Then the integrals in  $\langle V_i \rangle$  can be computed using the Hermite-Gauss quadrature rule appropriate for the dimension of the space [83]. For the general case of an  $n$ -body interatomic potential  $\phi(\mathbf{q}_1, \dots, \mathbf{q}_n)$  the expectation value given by eq. (3.1) becomes

$$\begin{aligned}
 \langle \phi(\mathbf{q}_1, \dots, \mathbf{q}_n) \rangle &= \sum_{\epsilon_1=0}^1 \dots \sum_{\epsilon_N=0}^1 \frac{1}{h^{3N}} \int_{-\infty}^{\infty} \phi(\mathbf{q}_1, \dots, \mathbf{q}_n) p(\mathbf{q}, \mathbf{p}, \epsilon_1, \dots, \epsilon_N) \prod_{i=1}^N \prod_{j=1}^3 dq_{ij} dp_{ij} \\
 &= \prod_{i=1}^n \left( \sqrt{2\pi} \frac{\sigma_i}{\omega_i} \right)^{-3} \int_{-\infty}^{\infty} \phi(\mathbf{q}_1, \dots, \mathbf{q}_n) \prod_{i=1}^n \exp\left(-\frac{\omega_i^2}{2\sigma_i^2} |\mathbf{q}_i - \bar{\mathbf{q}}_i|^2\right) d\mathbf{q}_i \\
 &= \left(\frac{1}{\pi}\right)^{\frac{3}{2}n} \int_{-\infty}^{\infty} \dots \int_{-\infty}^{\infty} \tilde{\phi}(\mathbf{x}_1, \dots, \mathbf{x}_n) \prod_{i=1}^n \exp\left(-|\mathbf{x}_i|^2\right) d\mathbf{x}_i \tag{3.71}
 \end{aligned}$$

where the multiple integral in the last row of eq. (3.71) is of dimension  $3n$  and we have made the following change of variables

$$\begin{aligned}
 \tilde{\phi}(\mathbf{x}_1, \dots, \mathbf{x}_n) &= \phi(\mathbf{q}_1(\mathbf{x}_1), \dots, \mathbf{q}_n(\mathbf{x}_n)) \\
 \mathbf{x}_i &= \frac{\omega_i}{\sqrt{2}\sigma_i} (\mathbf{q}_i - \bar{\mathbf{q}}_i) \tag{3.72}
 \end{aligned}$$

A quadrature rule using  $M$  integration points reduces the above integral to

$$\langle \phi(\mathbf{q}_1, \dots, \mathbf{q}_n) \rangle \approx \left(\frac{1}{\pi}\right)^{\frac{3}{2}n} \sum_{k=1}^M \tilde{\phi}(\theta_k) w_k \tag{3.73}$$

where  $\theta_k = (\mathbf{x}_1, \dots, \mathbf{x}_n)$  is the  $k$ -th quadrature point (a  $3n$ -dimensional vector) and  $w_k$  is the related

quadrature weight. A limiting factor in the choice of quadrature formulae is the dimension of the domain of integration. For many-body potentials such as the ones pertaining to the Embedded Atom Method family (EAM), we are restricted to  $3^{rd}$  degree quadrature due to the high dimension of the space of integration. Given, for example, an fcc crystal with nearest-neighbor interactions,  $n = 13$  for an atom having all its neighbors, so the dimension of each quadrature point is  $m = 39^{11}$ . Then, if a quadrature rule of order 3 is assumed, the number of quadrature point is  $M = 2m = 78$ .

For a  $m$ -dimensional space the quadrature points proposed by Stroud [83] are

$$\begin{aligned} & \overbrace{\left( \pm\sqrt{\frac{m}{2}}, 0, \dots, 0 \right)}^m \\ & \dots \\ & \left( 0, 0, \dots, \pm\sqrt{\frac{m}{2}} \right) \end{aligned} \tag{3.74}$$

and the weight factors can be written as

$$w_k = \frac{\pi^{\frac{m}{2}}}{2m} \quad \forall k = 1..M \tag{3.75}$$

As final remark notice that the max-ent probability distribution  $p$  provides a way to compute an approximate mean internal energy  $\langle V \rangle$  that is exact for up to a  $3^{rd}$  order Taylor expansion about the set of mean atomic positions  $\bar{\mathbf{q}}$ . This higher order approximation has the ability to account for the anharmonicity of the interaction potential –although approximately– when studying the thermodynamic behavior of materials.

---

<sup>11</sup> $m = 3n$  is the dimension of the integration space

### 3.9 Appendix II: Johnson's EAM Potentials

According to the analytic nearest-neighbor EAM model proposed by Johnson for fcc pure metals [56], both the electron density  $f(r)$  and the two-body potential  $\Phi(r)$  can be expressed as decreasing exponential functions requiring two parameters each<sup>12</sup>:

$$\begin{aligned} f(r) &= f_e \exp \left[ -\beta \left( \frac{r}{r_e} - 1 \right) \right], & r_e &= \frac{a}{\sqrt{2}} \\ \Phi(r) &= \Phi_e \exp \left[ -\gamma \left( \frac{r}{r_e} - 1 \right) \right] \end{aligned} \quad (3.76)$$

In addition the embedding function  $F(\rho)$  is obtained from the zero-temperature equation of state proposed by Rose et al. [58]<sup>13</sup>:

$$F(\rho) = -E_c \left[ 1 - \frac{\alpha}{\beta} \ln \left( \frac{\rho}{\rho_e} \right) \right] \left( \frac{\rho}{\rho_e} \right)^{\frac{\alpha}{\beta}} - 6\Phi_e \left( \frac{\rho}{\rho_e} \right)^{\frac{\gamma}{\beta}}, \quad \rho_e = 12f_e \quad (3.77)$$

The model parameters ( $f_e$ ,  $\Phi_e$ ,  $\alpha$ ,  $\beta$ , and  $\gamma$ ) are determined by fitting the lattice constant  $a$  or atomic volume  $V$ , the cohesive energy  $E_c$ , the unrelaxed vacancy-formation energy  $E_{UF}$ , the bulk modulus:

$$B = \frac{C_{11} + 2C_{12}}{3} \quad (3.78)$$

and the Voigt-average shear modulus (all these quantities at room temperature):

$$G = \frac{C_{11} - C_{12} + 3C_{44}}{5} \quad (3.79)$$

This potential does not include additional parameters to fit alloy properties, but the calculated heat of solution for binary alloys has been shown to be consistent with experimental data [56]. The model parameters for the elements used in this work (Cu, Ni, Pd, Au, Ag) are listed in Table 3.2.

---

<sup>12</sup>In prior EAM calculations the electron density  $f(r)$  has been assumed to be well represented by spherically averaged free-atom densities calculated from Hartree-Fock theory. According to Johnson [76], when these Hartree-Fock electronic densities are plotted they can be approximated by a single exponential function. This is therefore the functionality assumed by this author.

<sup>13</sup>Based upon the compilation of many first-principle calculations, Rose et al. showed that for a broad range of materials the cohesive energy  $E_c$  as a function of nearest-neighbor distance  $r_e$  is well approximated by an EOS.

element	$f_e$ [-]	$\Phi_e$ [eV]	$\alpha$ [-]	$\beta$ [-]	$\gamma$ [-]
Cu	0.30	0.59	5.09	5.85	8.00
Ni	0.41	0.74	4.98	6.41	8.86
Pd	0.27	0.65	6.42	5.91	8.23
Au	0.23	0.65	6.37	6.67	8.20
Ag	0.17	0.48	5.92	5.96	8.26

Table 3.2: EAM parameters

The information provided above allows the determination of the following functions in equation (3.38):  $F^A(\rho)$ ,  $F^B(\rho)$ ,  $f^A(r)$ ,  $f^B(r)$ ,  $\Phi^{AA}(r)$ ,  $\Phi^{BB}(r)$ . Johnson builds the remaining  $\Phi^{AB}(r)$ —which describes the pair interaction between atoms of different species— from the monoatomic functions [56]:

$$\Phi^{AB}(r) = \frac{1}{2} \left[ \frac{f^B(r)}{f^A(r)} \Phi^{AA}(r) + \frac{f^A(r)}{f^B(r)} \Phi^{BB}(r) \right] \quad (3.80)$$

## Chapter 4

# Variational Coupling for Non-Equilibrium Mechano-Chemical Problems

The equilibrium formulation presented in the last chapter allowed us to characterize the effect of concentration on (equilibrium) material properties. However, our final goal is to simulate kinetic processes such as the time evolution of impurity segregation towards grain boundaries. To this end, we present in this chapter an extension of the variational formulation proposed by Yang et al. [5] for mechano-chemical coupled problems.

The main difference between the work done by Yang et al. [5] and the framework we are about to present is that the latter is discrete from the onset. Therefore, instead of discretizing the governing equations describing the behavior of continuum media, we start directly from a discrete system without any reference to the continuum. This seems a more natural starting point for the atomistic samples considered so far, which are intrinsically discrete. Crystalline solids are of important practical interest in material science, and the anisotropic nature of their properties arises from the geometry and connectivity of the intermolecular bonds in the lattice. We will model these lattices as inherently discrete objects. In particular, we think this could yield a more detailed geometric understanding of how the system evolves in the presence of grain boundaries and other defects.

The formulation that follows relies on Discrete Exterior Calculus (DEC) [84]. This theory develops *ab initio* a calculus on discrete manifolds that parallels the calculus on smooth manifolds of arbitrary finite dimension. In our case we make use of *simplicial complexes*. Familiar examples of

simplicial complexes are meshes of triangles embedded in  $\mathcal{R}^3$  and tetrahedral meshes occupying a portion of  $\mathcal{R}^3$ . Given a set of lattice points, in this work we construct a simplicial triangulation by recourse to Delaunay triangulation techniques.

In this chapter we show the existence of a joint potential function whose Euler-Lagrange equations yield the equilibrium equation, the kinetic relations and the conservation of mass of different species within a binary alloy. We restrict ourselves to elastic solids undergoing diffusional processes since we do not assume any flow, hardening rules or viscosity law in our work. Moreover, the only kinetic relation that we introduce *a priori* is the generalized Fick's law of diffusion.

As we shall see, the variational structure determines the coupling between mechanics and diffusion in a unique way. Thus, there is no need to postulate additional constitutive relations relating chemical potentials with concentrations or the state of stress of the system.

## 4.1 Balance Laws

The following equations describe the mechano-chemical coupled problem for a binary system with no prescribed external fluxes or forces:

1. Linear momentum balance<sup>1</sup>,

$$\nabla \cdot \sigma = \mathbf{0} \quad \text{in } V \quad (4.1)$$

2. A-component mass balance<sup>2</sup>,

$$\dot{x}_A = -\nabla \cdot \mathbf{J}_A \quad \text{in } V \quad (4.2)$$

3. Equation of state,

$$F = F(\mathbf{E}, x_A) \quad \text{in } V \quad (4.3)$$

---

<sup>1</sup>The very different time scales for elastic and chemical equilibrium justify the assumption of elastic equilibrium at all times [85]

<sup>2</sup>Since we are not considering chemical reactions, and by definition

$$\frac{\partial F}{\partial x_k} = \mu_k, \quad x_A + x_B = 1$$

then  $\mu_B = -\mu_A$ . As we'll see, the atomic flux  $\mathbf{J}_k$  is proportional to the gradient of chemical potential  $\nabla \mu_k$ . Then there is no need to solve for the B-component balance provided that the number of lattice sites  $N$  remains constant.

where  $\sigma$  is the Cauchy stress tensor,  $x_A$  is the atomic fraction of the  $A$ -component,  $\mathbf{J}_A$  is the atomic flux of that species,  $F$  is the Helmholtz free energy,  $\mathbf{E}$  is an appropriate deformation measure, and  $V$  is the volume occupied by the system in the current configuration.

## 4.2 Rate Problem

A rate problem involves finding the rate of change of the state of the system given its current state and boundary conditions. For an elastic solid undergoing diffusional processes (but no chemical reactions), this means the problem of determining  $(\dot{\mathbf{q}}, \{\dot{x}_A\}, \{\mu_A\})^3$  given the current local state  $(\mathbf{E}, \{x_A\})$ .

We consider the set of lattice sites as a collection of points indexed by an index set  $I_0$  and a collection of bonds defined by pairs of sites and indexed by an index set  $I_1$ . We denote by  $\Omega_0$  the collection of scalar real-valued discrete fields  $u : I_0 \rightarrow \mathbb{R}$  defined over the point set  $I_0$ , and by  $\Omega_1$  the collection of scalar real-valued discrete fields  $\beta : I_1 \rightarrow \mathbb{R}$  defined over the bond set  $I_1$ . In addition  $d : \Omega_0 \rightarrow \Omega_1$  is the discrete differential operator [84, 86],

$$du_{ij} = u_j - u_i \quad (4.4)$$

for all  $[i, j] \in I_1$ . We define the codifferential operator  $\delta : \Omega_1 \rightarrow \Omega_0$  by duality through the identity

$$\langle du, \beta \rangle = \sum_{[i,j] \in I_1} du_{ij} \beta_{ij} = \sum_{i \in I_0} u_i \delta \beta_i = \langle u, \delta \beta \rangle \quad (4.5)$$

for all  $u \in \Omega_0$  and  $\beta \in \Omega_1$ .

Next, we consider discrete joint potential functions of the following form:

$$\Phi [\dot{\mathbf{q}}, \{\dot{x}_A\}, \{\mu_A\}] = \dot{F}(\dot{\mathbf{q}}, \{\dot{x}_A\}) - \sum_{i \in I_0} \mu_{A,i} \dot{x}_{A,i} + \Delta(\{x_A\}, \{\mu_A\}) \quad (4.6)$$

---

<sup>3</sup> $\dot{\mathbf{q}}$  and  $\{\mu_A\}$  are the set of atomic mean positions and chemical potentials in the current configuration, respectively.  $\dot{y}$  represents the rate of change of  $y$  over a given infinitesimal time interval.

where  $\mu_A$  is the chemical potential of the  $A$ -component and  $\Delta$  is a dissipation potential.

The Helmholtz free energy  $F$  should remain unchanged if the crystal and the system of applied stresses are translated or rotated together. A potential is translationally invariant, i. e.,  $F(u + c) = F(u)$  for all  $c \in \Omega_0$  such that  $c = \text{constant}$  for all  $i \in I_0$ , if it can be expressed as<sup>4</sup> [86]

$$F(u) = F(du) \quad (4.7)$$

Likewise, taking into account that the driving force of diffusion is given by the gradient of chemical potential  $\nabla\mu_A$ , we claim that  $\Delta$  should also be translationally invariant, this is,

$$\Delta(\mu_A) = \Delta(d\mu_A) \quad (4.8)$$

where  $d\mu_A \in \Omega_1$  is a bondwise discrete chemical potential gradient. Then, the dissipation potential  $\Delta$  acts as a potential for the atomic flux, i. e., it has the fundamental property that

$$\mathbf{J}_A = \frac{\partial \Delta}{\partial d\mu_A} \quad (4.9)$$

where  $\mathbf{J}_A \in \Omega_1$  are the bondwise mass fluxes. In this work we will specifically assume quadratic and bondwise-additive dissipation potentials. In particular, we write whereupon the discrete joint functional as,

$$\Phi [d\dot{\mathbf{q}}, \{\dot{x}_A\}, \{\mu_A\}] = \dot{F}(d\dot{\mathbf{q}}, \{\dot{x}_A\}) - \sum_{i \in I_0} \mu_{A,i} \dot{x}_{A,i} - \sum_{[i,j] \in I_1} \frac{1}{2} M_A \bar{x}_{A,ij} d\mu_{A,ij}^2 \quad (4.10)$$

where  $M_A$  is the mobility of the diffusing species –an additional input parameter besides interatomic potentials– and  $\bar{x}_{A,ij} \in \Omega_1$  represents the average concentration on bond  $[i, j]$  and will be defined in the next section. Here, the term *bond* denotes an edge (or 1-cell) of the Delaunay triangulation built over the lattice sites of the system.

---

<sup>4</sup>Since the Helmholtz free energy  $F$  is also a function of the set  $\{x_A\}$ , we consider  $F$  to be a potential of the type  $F : [I_0 \times I_1] \rightarrow \mathbb{R}$ , or in other words:  $F = F(\{x_A\}, d\mathbf{q})$ .

For quadratic dissipation potentials of the form included in (4.10), the relation (4.9) reduces to the generalized Fick's law [87]<sup>5</sup>,

$$\mathbf{J}_{A,ij} = -M_A \bar{x}_{A,ij} d\mu_{A,ij} \quad (4.11)$$

Now, in order to guarantee that the general rate problem for chemo-elastic solids is equivalent to the stationarity principle:  $\delta\Phi = 0$ , we still need to prove that the Euler-Lagrange equations that follow from  $\delta\Phi = 0$  give the balance laws (4.1)-(4.3).

The basic variations needed to determine the discrete Euler-Lagrange equations are obtained from changing the value of the function  $\Phi$  at a given lattice site  $k$  leaving the other values fixed. These variations have the form

$$\phi_\epsilon = \phi + \epsilon\eta \quad (4.12)$$

where  $\epsilon \in \mathbb{R}$  and  $\eta \in \Omega_0$  is such that

$$\langle \eta, k \rangle = 1, \quad \langle \eta, j \rangle = 0 \quad (4.13)$$

for any given  $j \in I_0$ ,  $j \neq k$ .

This family of variations is enough to establish the variational principle [84],

$$\left. \frac{d\Phi}{d\epsilon}(\phi_\epsilon) \right|_{\epsilon=0} = 0 \quad (4.14)$$

As follows from eq. (4.10),  $\Phi = \Phi [d\dot{\mathbf{q}}, \{\dot{x}_A\}, \{\mu_A\}]$ . Thus changing the value of  $\Phi$  at site  $k$  gives,

$$\begin{aligned} & \Phi \left[ \{d\dot{\mathbf{q}}_{jk}\}_{(\dot{\mathbf{q}}_k + \epsilon\eta)}, \{d\dot{\mathbf{q}}_{\ell m}\}, \{\dot{x}_A\}, \{\mu_A\} \right] = \\ & \dot{F} \left( \{d\dot{\mathbf{q}}_{jk}\}_{(\dot{\mathbf{q}}_k + \epsilon\eta)}, \{d\dot{\mathbf{q}}_{\ell m}\}, \{\dot{x}_A\} \right) - \sum_{i \in I_0} \mu_{A,i} \dot{x}_{A,i} - \sum_{[i,j] \in I_1} \frac{1}{2} M_A \bar{x}_{A,ij} d\mu_{A,ij}^2 \end{aligned} \quad (4.15)$$

---

<sup>5</sup>Thus, in this work Fick's law is used as the constitutive equation relating the atomic flux  $\mathbf{J}_A$  with the driving force for diffusion, i. e., the gradient of chemical potential  $\nabla\mu_A$

where  $\ell, m \neq k$ ,

$$\begin{aligned} \Phi [d\dot{\mathbf{q}}, \dot{x}_{A,1}, \dots, (\dot{x}_{A,k} + \epsilon\eta), \dots, \dot{x}_{A,N}, \{\mu_A\}] &= \dot{F} (d\dot{\mathbf{q}}, \dot{x}_{A,1}, \dots, (\dot{x}_{A,k} + \epsilon\eta), \dots, \dot{x}_{A,N}, \{\mu_A\}) - \\ &\sum_{i \in I_0, i \neq k} \mu_{A,i} \dot{x}_{A,i} - \mu_{A,k} (\dot{x}_{A,k} + \epsilon\eta) - \sum_{[i,j] \in I_1} \frac{1}{2} M_A \bar{x}_{A,ij} d\mu_{A,ij}^2 \end{aligned} \quad (4.16)$$

$$\begin{aligned} \Phi [d\dot{\mathbf{q}}, \{\dot{x}_A\}, \mu_{A,1}, \dots, (\mu_{A,k} + \epsilon\eta), \dots, \mu_{A,N}] &= \dot{F} (d\dot{\mathbf{q}}, \{\dot{x}_A\}) - \sum_{i \in I_0, i \neq k} \mu_{A,i} \dot{x}_{A,i} - \\ &(\mu_{A,k} + \epsilon\eta) \dot{x}_{A,k} - \sum_{[i,j] \in I_1, i, j \neq k} \frac{1}{2} M_A \bar{x}_{A,ij} d\mu_{A,ij}^2 - \sum_{[i,k] \in I_1} \frac{1}{2} M_A \bar{x}_{A,ik} d\mu_{A,ik}^2 \end{aligned} \quad (4.17)$$

Taking variations as described in expression (4.14); eqs. (4.15), (4.16) and (4.17) become respectively,

$$\sum_{[i,k] \in I_1} \frac{\partial \dot{F}}{\partial d\dot{\mathbf{q}}_{ik}} d\eta_{ik} = \mathbf{0} \quad (4.18)$$

$$\frac{\partial \dot{F}}{\partial \dot{x}_{A,k}} \langle \eta, k \rangle - \mu_{A,k} \langle \eta, k \rangle = 0 \quad (4.19)$$

$$-\dot{x}_{A,k} \langle \eta, k \rangle - \sum_{[i,k] \in I_1} (M_A \bar{x}_{A,ik} d\mu_{A,ik}) d\eta_{ik} = 0 \quad (4.20)$$

where –from eq. (4.13)–  $\langle \eta, k \rangle = 1$ .

Finally, by recourse to the codifferential operator definition (eq. 4.5) and the following identity

$$\left\langle \frac{\partial F}{\partial du} (du), dv \right\rangle = \left\langle \delta \frac{\partial F}{\partial du} (du), v \right\rangle \quad \forall v \in \Omega_0 \quad (4.21)$$

the Euler-Lagrange equations that follow from  $\delta\Phi = 0$  can be written as:

$$\delta \frac{\partial \dot{F}}{\partial d\dot{\mathbf{q}}} = \mathbf{0} \quad (4.22)$$

$$\frac{\partial \dot{F}}{\partial \dot{x}_A} = \mu_A \quad (4.23)$$

$$\dot{x}_A = \delta (M_A \bar{x}_A d\mu_A) \quad (4.24)$$

The correspondence between eqs. (4.1)-(4.3) and (4.22)-(4.24) confirms that the solution to the

mechano-chemical rate problem may be stated as a three field variational problem

$$\inf_{\bar{\mathbf{q}}} \inf_{\{\dot{x}_A\}} \sup_{\{\mu\}} \Phi \quad (4.25)$$

where transient effect appear as rate-dependency in a quasi-stationary form, and we look for the set of chemical potentials  $\{\mu\}$  that maximize  $\Phi$  since this functional is concave in that field.

### 4.3 Incremental Formulation

We now present a time-discretized version of the variational problem presented in the last section. The purpose of time discretization is to reduce the modeling of time-dependent phenomena to a sequence of incremental problems, each characterized by a variational principle. Following the work by Yang et al. [5], we give an outline of the incremental extremum problem formulated by identifying a convenient joint potential that is consistent with the field equations. To this end, we consider a sequence of times  $t^0, \dots, t^n$  and seek to characterize the state of the system  $(\bar{\mathbf{q}}^{n+1}, \{x_A^{n+1}\}, \{\mu_A^{n+1}\})$  at time  $t^{n+1}$  assuming the state  $(\bar{\mathbf{q}}^n, \{x_A^n\}, \{\mu_A^n\})$  is known. Specifically, we construct a family of incremental functionals  $\Phi^{n+1}$  based on the backward Euler finite difference scheme (to avoid stability time-step  $\Delta t$  restrictions):

$$\begin{aligned} \Phi^{n+1} [d\bar{\mathbf{q}}^{n+1}, \{x_A^{n+1}\}, \{\mu_A^{n+1}\}] = & (F^{n+1} - F^n) - \\ & \sum_{i \in I_0} \mu_{A,i}^{n+1} (x_{A,i}^{n+1} - x_{A,i}^n) - \sum_{[i,j] \in I_1} \frac{\Delta t}{2} M_A \bar{x}_{A,ij}^n (d\mu_{A,ij}^{n+1})^2 \end{aligned} \quad (4.26)$$

The incremental variational problem then becomes

$$\inf_{\bar{\mathbf{q}}^{n+1}} \inf_{\{x_A^{n+1}\}} \sup_{\{\mu^{n+1}\}} \Phi^{n+1} \quad (4.27)$$

This scheme is consistent with the field equations (4.1)-(4.3) because taking variations of the

discrete functional yields:

$$\delta \frac{\partial F^{n+1}}{\partial d\bar{\mathbf{q}}^{n+1}} = O(\Delta t) \quad (4.28)$$

$$\frac{\partial F^{n+1}}{\partial x_A^{n+1}} - \mu_A^{n+1} = O(\Delta t) \quad (4.29)$$

$$-\frac{(x_A^{n+1} - x_A^n)}{\Delta t} - \delta (M_A \bar{x}_A^n d\mu_A^{n+1}) = O(\Delta t^2) \quad (4.30)$$

which converge to the discrete field equations (4.1)-(4.3) as  $\Delta t \rightarrow 0$ , provided the second term on the l.h.s of eq. (4.20):  $-\sum_{i \in \text{St}(k)} M_A \bar{x}_{A,ik}^n d\mu_{A,ik}^{n+1}$  is consistent with  $\nabla \cdot (M_A x_A^n \nabla \mu_A^{n+1})$  (see eq. 4.11).

Next we propose a functional form for  $\bar{x}_{A,ij}$  that meets the above consistency requirement. From eq. (4.4),

$$\sum_{i \in \text{St}(k)} -M_A \bar{x}_{A,ik} d\mu_{A,ik} = M_A [\bar{x}_{A,1k}(\mu_{A,1} - \mu_{A,k}) + \dots + \bar{x}_{A,Zk}(\mu_{A,Z} - \mu_{A,k})] \quad (4.31)$$

where  $Z$  is the number of sites that share a bond with atom  $k$  and –hereafter– we omit the time supra-index for simplicity. Expanding the l.h.s of the last equation about  $\mu_{A,k}$  it becomes,

$$\begin{aligned} \sum_{i \in \text{St}(k)} -M_A \bar{x}_{A,ik} d\mu_{A,ik} &= \bar{x}_{A,1k} M_A \left[ \frac{\partial \mu_A}{\partial x} \Big|_k \Delta x_{1k} + \frac{\partial \mu_A}{\partial y} \Big|_k \Delta y_{1k} + \frac{\partial \mu_A}{\partial z} \Big|_k \Delta z_{1k} \right] + \\ &\bar{x}_{A,1k} M_A \left[ \frac{1}{2} \frac{\partial^2 \mu_A}{\partial x^2} \Big|_k \Delta x_{1k}^2 + \frac{1}{2} \frac{\partial^2 \mu_A}{\partial y^2} \Big|_k \Delta y_{1k}^2 + \frac{1}{2} \frac{\partial^2 \mu_A}{\partial z^2} \Big|_k \Delta z_{1k}^2 \right] + \\ &\dots + \\ &\bar{x}_{A,Zk} M_A \left[ \frac{\partial \mu_A}{\partial x} \Big|_k \Delta x_{Zk} + \frac{\partial \mu_A}{\partial y} \Big|_k \Delta y_{Zk} + \frac{\partial \mu_A}{\partial z} \Big|_k \Delta z_{Zk} \right] + \\ &\bar{x}_{A,Zk} M_A \left[ \frac{1}{2} \frac{\partial^2 \mu_A}{\partial x^2} \Big|_k \Delta x_{Zk}^2 + \frac{1}{2} \frac{\partial^2 \mu_A}{\partial y^2} \Big|_k \Delta y_{Zk}^2 + \frac{1}{2} \frac{\partial^2 \mu_A}{\partial z^2} \Big|_k \Delta z_{Zk}^2 \right] + O(\Delta^2) \end{aligned} \quad (4.32)$$

In addition, we assume the average concentration on bond  $[i, j]$  can be written as

$$\bar{x}_{A,ik} = \frac{c}{2} (x_{A,i} + x_{A,k}) \quad (4.33)$$

and therefore also admits a series expansion about  $x_{A,k}$ . Then eq. (4.32) turns into:

$$\begin{aligned}
& \sum_{i \in \text{St}(k)} -M_A x_{A,ik} d\mu_{A,ik} = x_{A,k} cM_A \left. \frac{\partial \mu_A}{\partial x} \right|_k (\Delta x_{1k} + \dots + \Delta x_{Zk}) + x_{A,k} cM_A \left. \frac{\partial \mu_A}{\partial y} \right|_k (\Delta y_{1k} + \dots + \Delta y_{Zk}) + \\
& x_{A,k} cM_A \left. \frac{\partial \mu_A}{\partial z} \right|_k (\Delta z_{1k} + \dots + \Delta z_{Zk}) + \frac{1}{2} x_{A,k} cM_A \left. \frac{\partial^2 \mu_A}{\partial x^2} \right|_k (\Delta x_{1k}^2 + \dots + \Delta x_{Zk}^2) + \\
& \frac{1}{2} x_{A,k} cM_A \left. \frac{\partial^2 \mu_A}{\partial y^2} \right|_k (\Delta y_{1k}^2 + \dots + \Delta y_{Zk}^2) + \frac{1}{2} x_{A,k} cM_A \left. \frac{\partial^2 \mu_A}{\partial z^2} \right|_k (\Delta z_{1k}^2 + \dots + \Delta z_{Zk}^2) + \\
& \frac{1}{2} cM_A \left. \frac{\partial x_A}{\partial x} \frac{\partial \mu_A}{\partial x} \right|_k (\Delta x_{1k}^2 + \dots + \Delta x_{Zk}^2) + \frac{1}{2} cM_A \left. \frac{\partial x_A}{\partial x} \frac{\partial \mu_A}{\partial y} \right|_k (\Delta x_{1k} \Delta y_{1k} + \dots + \Delta x_{Zk} \Delta y_{Zk}) + \\
& \frac{1}{2} cM_A \left. \frac{\partial x_A}{\partial x} \frac{\partial \mu_A}{\partial z} \right|_k (\Delta x_{1k} \Delta z_{1k} + \dots + \Delta x_{Zk} \Delta z_{Zk}) + \frac{1}{2} cM_A \left. \frac{\partial x_A}{\partial y} \frac{\partial \mu_A}{\partial x} \right|_k (\Delta x_{1k} \Delta y_{1k} + \dots + \Delta x_{Zk} \Delta y_{Zk}) + \\
& \frac{1}{2} cM_A \left. \frac{\partial x_A}{\partial y} \frac{\partial \mu_A}{\partial y} \right|_k (\Delta y_{1k}^2 + \dots + \Delta y_{Zk}^2) + \frac{1}{2} cM_A \left. \frac{\partial x_A}{\partial y} \frac{\partial \mu_A}{\partial z} \right|_k (\Delta y_{1k} \Delta z_{1k} + \dots + \Delta y_{Zk} \Delta z_{Zk}) + \\
& \frac{1}{2} cM_A \left. \frac{\partial x_A}{\partial z} \frac{\partial \mu_A}{\partial x} \right|_k (\Delta x_{1k} \Delta z_{1k} + \dots + \Delta x_{Zk} \Delta z_{Zk}) + \frac{1}{2} cM_A \left. \frac{\partial x_A}{\partial z} \frac{\partial \mu_A}{\partial y} \right|_k (\Delta y_{1k} \Delta z_{1k} + \dots + \Delta y_{Zk} \Delta z_{Zk}) + \\
& \frac{1}{2} cM_A \left. \frac{\partial x_A}{\partial z} \frac{\partial \mu_A}{\partial z} \right|_k (\Delta z_{1k}^2 + \dots + \Delta z_{Zk}^2) + O(\Delta^3)
\end{aligned} \tag{4.34}$$

On the other hand,

$$\nabla \cdot (M_A x_A \nabla \mu_A) = M_A \left( \frac{\partial x_A}{\partial x} \frac{\partial \mu_A}{\partial x} + \frac{\partial x_A}{\partial y} \frac{\partial \mu_A}{\partial y} + \frac{\partial x_A}{\partial z} \frac{\partial \mu_A}{\partial z} \right) \Big|_k + x_{A,k} M_A \left( \frac{\partial^2 \mu_A}{\partial x^2} + \frac{\partial^2 \mu_A}{\partial y^2} + \frac{\partial^2 \mu_A}{\partial z^2} \right) \Big|_k \tag{4.35}$$

Then, compatibility of eqs. (4.34) and (4.35) requires,

$$\begin{aligned}
\Delta x_{1k} + \dots + \Delta x_{Zk} &= 0 \\
\Delta y_{1k} + \dots + \Delta y_{Zk} &= 0 \\
\Delta z_{1k} + \dots + \Delta z_{Zk} &= 0 \\
\Delta x_{1k} \Delta y_{1k} + \dots + \Delta x_{Zk} \Delta y_{Zk} &= 0 \\
\Delta x_{1k} \Delta z_{1k} + \dots + \Delta x_{Zk} \Delta z_{Zk} &= 0 \\
\Delta y_{1k} \Delta z_{1k} + \dots + \Delta y_{Zk} \Delta z_{Zk} &= 0 \\
\frac{c}{2} (\Delta x_{1k}^2 + \dots + \Delta x_{Zk}^2) &= 1 \\
\frac{c}{2} (\Delta y_{1k}^2 + \dots + \Delta y_{Zk}^2) &= 1 \\
\frac{c}{2} (\Delta z_{1k}^2 + \dots + \Delta z_{Zk}^2) &= 1
\end{aligned} \tag{4.36}$$

The first six equations are satisfied automatically for a bulk atom in both fcc and bcc perfect lattices.

The last three yield –for both crystal structures,

$$c = \frac{1}{a^2} \tag{4.37}$$

where  $a$  is the lattice parameter.

We will generalize the last equation by defining,

$$c = \frac{6}{\sum_i^Z r_{ik}^2} \tag{4.38}$$

where  $r_{ik}$  stands for the distance between atoms  $i$  and  $k$  and we have added the last three equations in (4.36). Then, the final expression for  $x_{A,ik}$  in eq. (4.26) is,

$$\bar{x}_{A,ik} = 3 \left[ \frac{x_{A,i} + x_{A,k}}{\sum_i^Z r_{ik}^2} \right] \tag{4.39}$$

Eqs. (4.26), (4.27) and (4.39) will become the tool to describe the time evolution of mechano-

chemical problems in the next section. Moreover, we will rely on the expressions developed in Chapter 3 to account for the Helmholtz free energy  $F$  of the system. Specifically, and for the examples we are about to present, we will use eq. (3.43), which assumes thermal equilibrium during the diffusion process.

## 4.4 Numerical Results

In this section we assess the validity of the non-equilibrium formulation developed in previous sections. Specifically, we present two proof-of-concept examples: diffusion in a rigid solid and diffusion within a solid subjected to uniaxial tensile strain.

Two samples comprising  $3 \times 3 \times 30$  unit cells (3691 lattice sites) were subjected to an initial copper concentration profile of the form:

$$x_A(z)|_{t=0} = \frac{(2x_A^o - 1)}{4\sqrt{\pi M_A k_b T t_o}} a_o \exp\left[\frac{-(z - \frac{L}{2})^2}{4M_A k_b T t_o}\right] + (1 - x_A^o) \quad (4.40)$$

where  $x_A^o = 0.8$ ,  $t_o = 5.3 \times 10^6$  ps,  $T = 700$  K,  $M_A = 1.1 \times 10^{-8}$   $\text{\AA}^2/\text{eV}/fs$  [88]; and  $L \approx 110$   $\text{\AA}$  is the total length of the sample, see Fig. 4.1. In addition,  $a_o = 3.5801$   $\text{\AA}$  is the equilibrium lattice parameter determined for that temperature and composition in a fully periodic system containing 666 lattice sites. Periodic boundary conditions were applied in both  $x$  and  $y$  directions, while atoms within the region  $z \in [0, a]$  and  $z \in [L - a, L]$  were constrained to the equilibrium lattice spacing  $a$ , atomic fraction  $x_A$ , mean field parameter  $w$  and chemical potential  $\mu_A$  of the fully periodic system. The samples were large enough (or in other words, the total simulation time was short enough) in order for this boundary condition not to affect the outcome of the simulation. Furthermore, atomic positions were prescribed in the entire first sample and in the left half of the second sample, see Fig. 4.1. The time step  $\Delta t$  was at least one order of magnitude smaller than the characteristic time of the system:  $a_o^2/(M_A k_b T)$ . In both cases, the time evolution was obtained from eqs. (4.26)-(4.27) by recourse to a non-linear version of the Conjugate Gradient Method.

Fig. 4.2 depicts the numerical results obtained for the rigid solid system against the (analytical)

solution for a thin film in the middle of an infinite bar,

$$x_A(z, t) = \frac{(2x_A^o - 1)}{4\sqrt{\pi M_A k_b T t}} a_o \exp\left[\frac{-(z - \frac{L}{2})^2}{4M_A k_b T t}\right] + (1 - x_A^o) \quad (4.41)$$

which is valid for  $2\sqrt{Dt} > a_o$ <sup>6</sup>. Expression (4.41) is a solution of eq. (4.2) provided the generalized Fick's law is valid,  $\mathbf{J}_A = -M_A x_A \nabla \mu_A$ , mobility  $M_A$  and temperature  $T$  are uniform within the sample, and the following constitutive equation relates the chemical potential  $\mu_A$  with the atomic fraction of the diffusing species  $x_A$ ,

$$\mu_A = \mu_A^o + k_b T \ln x_A \quad (4.42)$$

Moreover, the analytical solution described above corresponds to the following boundary conditions [89],

$$\begin{aligned} x_A &\rightarrow (1 - x_A^o) \quad \text{as } t \rightarrow \infty \quad \text{for } z \rightarrow 0|L \\ x_A &\rightarrow \infty \quad \text{as } t \rightarrow 0 \quad \text{for } z = \frac{L}{2} \end{aligned} \quad (4.43)$$

Now, recall that within the numerical framework presented in Section 4.3 chemical potential  $\mu_A$  and concentration  $x_A$  are independent variables. Then, the agreement between numerical and analytical results observed in Fig. 4.2 implies that the model captures the fact that the chemical potential of copper diffusing in a nickel-rich rigid solid solution has indeed the form given in eq. (4.42). In addition, notice that the time step used was  $\Delta t = 10^5$  ps, five orders of magnitude larger than the largest time step achievable in molecular dynamics (MD) simulations.

Fig. 4.3 shows the numerical results obtained for the semi-rigid solid system subjected to uniaxial tensile strain and to the initial Cu profile given by eq. (4.40). In this case we used a time step  $\Delta t = 5.0 \times 10^4$  ps, which gives a strain rate of the order  $10^4$  s<sup>-1</sup>, 3 orders of magnitude smaller than the smallest strain rate achievable for MD [90], see Fig. 4.1-b. Furthermore, eq. (4.27) was solved

---

<sup>6</sup>In order to make feasible the comparison between analytical and numerical results, this requirement determined our choice of  $t_o$  in eq. (4.40).

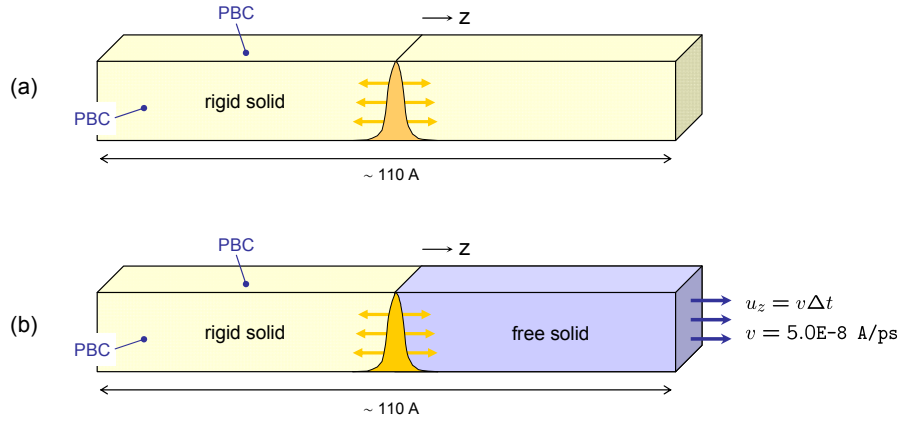


Figure 4.1: Scheme of the sample used to simulate: (a) rigid body diffusion, and (b) semi-rigid body diffusion. The orientation of the system is such that z- and  $[0\ 0\ 1]$  directions coincide.

using a staggered scheme, i. e., for each time step concentration  $x_A$  and chemical potential  $\mu_A$  were solved first –maintaining position  $\bar{\mathbf{q}}$  fixed– and then *vice versa*. Convergence was achieved once both sets of variables were obtained within one iteration.

The interplay between deformation and diffusion can be seen by comparing Figs. 4.2 and 4.3. Since the lattice parameter is 3 % larger in Cu than in Ni, Cu diffuses preferentially to the regions of the sample under tensile strain. Therefore, as the simulation evolves, the symmetry of the concentration profile is progressively lost. Moreover, starting from  $t = 3.0 \times 10^7 \text{ ps}$  the concentration of Cu increases on the plane of atoms originally at  $z = a_o/2$  because this plane is gradually seen as a free surface. This is consistent with the findings of Section 3.6.4, where Cu is the segregating species in CuNi alloys. This surface enrichment occurs faster than the diffusion driven purely by chemical potential gradients on the rigid portion of the sample, which explains the Cu impoverishment of the first five atomic planes to the left of  $z = 0$ .

## 4.5 Discussion

In this chapter we presented a numerical framework capable of following the time evolution of crystalline systems undergoing diffusion and deformation processes over time windows currently out of reach to traditional atomistic methods such as Molecular Dynamics (MD) or Monte Carlo (MC).

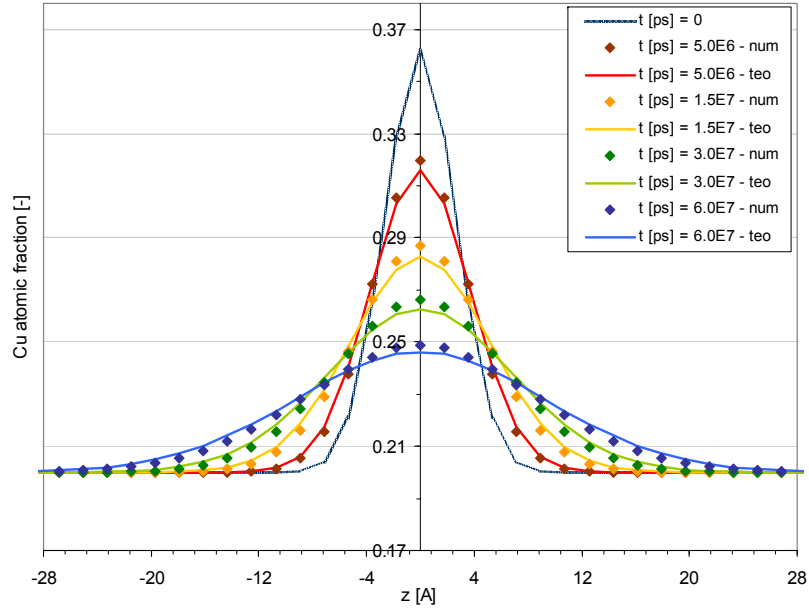


Figure 4.2: Time evolution of the average layer concentration within a rigid solid.

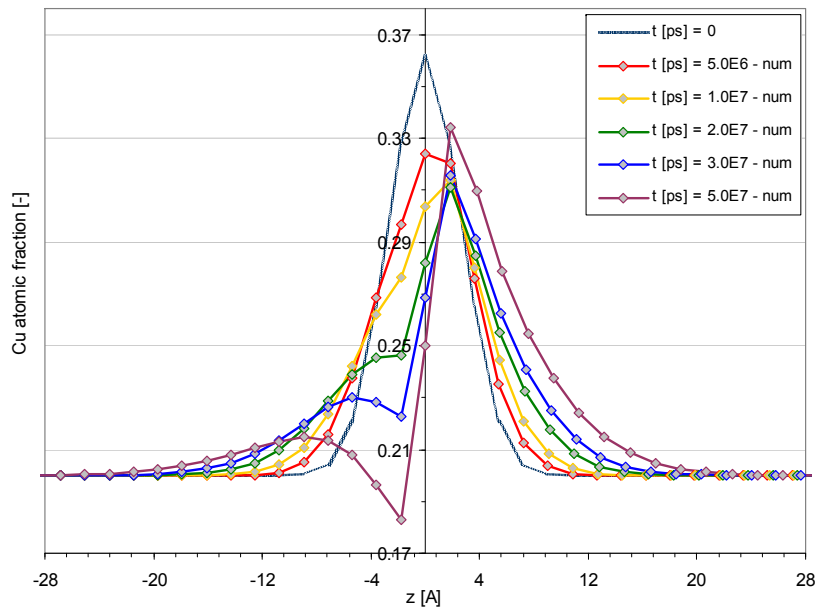


Figure 4.3: Time evolution of the average layer concentration within a semi-rigid solid subjected to uniaxial tensile strain in the  $z$ -direction.

In addition, the above was accomplished while retaining the underlying atomistic description of the material.

Based upon Discrete Exterior Calculus (DEC), we formulated a discrete variational setting in which the modeling of time-dependent phenomena is reduced to a sequence of incremental problems, each characterized by a variational principle. In this fashion we were able to study the interplay between deformation and diffusion using time steps (or strain rates) that are orders of magnitude larger (or smaller in the case of strain rates) than their MD|MC counterparts.

The model relies on the validity of the generalized Fick's law of diffusion and requires the mobility of the diffusing species as additional input, but it determines automatically the coupling between mechanics and diffusion. Therefore, there is no need to postulate additional constitutive relations connecting the impurity's chemical potential  $\mu_A$  with its concentration  $x_A$  or the state of stress of the system.



## Chapter 5

# Replica Time Integrators

This chapter is concerned with the classical problem of wave propagation in discrete models of nonuniform spatial resolution. We develop a new class of *Replica Time Integrators* (RTIs) that permit the two-way transmission of signals across mesh interfaces. This two-way transmissibility is accomplished by representing the state of the coarse region by means of a collection of identical copies –or *replicas*– of itself. In dimension  $d$ , RTIs afford an  $O(n^d)$  speed-up factor in sequential mode, and  $O(n^{d+1})$  in parallel, over regions that are coarsened  $n$ -fold. By a combination of phase-error analysis and numerical testing, we show that RTIs are convergent, and result in exact two-way transmissibility at the Courant-Friedrichs-Lewy (CFL) limit for any angle of incidence. RTIs allow step waves and thermal phonons to cross mesh interfaces in both directions listlessly, i. e., without appreciable loss or addition of energy, and without any ostensible internal reflections.

We begin by formulating RTIs for the elementary case of one-dimensional linear elastodynamics in Section 5.2. This special case provides a simple framework in which to introduce RTIs, firstly as a convergent and transmitting finite-difference scheme, secondly in their replica reinterpretation. Conveniently, the underlying finite-difference scheme is amenable to phase-error analysis. This analysis shows that the scheme is indeed convergent and establishes the transmission characteristics of the scheme across mesh interfaces. Remarkably, the scheme is found to afford exact two-way transmissibility at the Courant-Friedrichs-Lewy (CFL) limit. The introductory one-dimensional case also affords a third reinterpretation of the finite-difference scheme in terms of an overlap region between fine and coarse regions. This reinterpretation is subsequently taken as a basis for formally extending

RTIs to the finite-element and fully nonlinear frameworks. In Section 5.2 we also present numerical examples that exhibit some of the salient properties of RTIs, including their excellent performance in a standard benchmark test proposed by Belytschko et al. [91]. A particularly suggestive example concerns the transmission of thermal phonons into a 100-fold coarser region, represented by means of 100 replicas. Because of this relatively large size, it is possible to start thinking of the replica ensemble in the light of statistical thermodynamics, a line of thought that we return to in the discussion contained in Section 5.6.

In Section 5.3 we show that the entire program works just as well in arbitrary dimensions. We start by formulating RTIs as a finite-difference scheme, establishing its convergence and transmissibility properties by means of phase-error analysis. Subsequently we proceed to reinterpret the scheme in terms of replicas. As in the one-dimensional case, the phase error analysis shows that RTIs are convergent and afford exact two-way transmissibility at mesh interfaces at the CFL limit for any angle of incidence. In Section 5.4, RTIs are formally reformulated within the framework of finite elements, both linear and nonlinear. The properties of this extension are investigated in Section 5.5. Specifically, we perform numerical tests concerning three-dimensional linear and nonlinear step waves in a plate-impact configuration and their transmission across mesh interfaces under conditions of normal and tangential incidence. The step waves are allowed to reverberate several times through the thickness of the plate, resulting in several crossings of the mesh interface, both from the fine to the coarse region as well as from the coarse to the fine region. In all cases, the RTI waves cross the mesh interface listlessly, i. e., without appreciable loss or addition of energy, and without any ostensible internal reflections. Finally, the possible applications of RTIs to discrete-to-continuum approaches and, in particular, to the transition between molecular dynamics and continuum thermodynamics are discussed in Section 5.6 by way of future outlook.

## 5.1 Introduction

A fundamental problem of non-uniform discretizations is to formulate time-integration schemes that are capable of listlessly transmitting waves across mesh interfaces. The distinguishing characteristic

of the present approach, which we term *Replica Time Integration*, or RTI for short, is that it allows for the two-way transmission of thermal phonons across mesh interfaces. By thermal phonons here we specifically mean waves of wavelengths that are too small to be resolved by the coarse regions of the model. The two-way transmission afforded by RTIs is accomplished by representing the state of the coarse regions by means of *replica ensembles*, consisting of collections of identical copies of the coarse regions. Similar replica ensembles are commonly used in statistical physics to describe the equilibrium thermodynamic properties of systems such as spin glasses (cf., e. g., [92]). In RTI, the replicas within each ensemble run on their own slow time step and are out-of-phase with respect to each other by one fast time step. With the aid of this device, thermal phonons in the fine regions of the model can effectively be transmitted into coarse regions as ensembles of replica waves with a minimum of spurious internal reflections at the interface. Conversely, ensembles of replica waves in the coarse regions of the model are transmitted as thermal phonons into the fine regions. Remarkably, even with the overhead of replication factored in, in dimension  $d$  RTIs afford an  $O(n^d)$  speed-up factor in sequential mode, and  $O(n^{d+1})$  in parallel, over regions that are coarsened  $n$ -fold.

The problem of wave propagation in discrete models of nonuniform spatial resolution, and the related problem of radiating boundaries for the simulation of infinite domains has received considerable attention. For linear problems, exact non-reflecting boundary conditions have been derived [11, 94, 95, 117]. A number of other transmitting and absorbing boundary schemes have been proposed, including the absorbing boundary condition (ABC) method [96, 97], buffering [98–100], the perfectly matched layer method (PML) [101–106], the super-grid-method (SuGS) [104], stadium damping [107], variational boundary conditions [94, 95], the bridging domain method [91, 108], and others. The applicability of some of these methods is limited by assumptions of linearity, dimensionality, planarity of the interface, thermodynamic equilibrium and others. In addition, the implementation of some of these methods is compounded by features such as non-locality, hereditary integrals, constraint equations and others. Finally, the accuracy and efficiency of the transmitting boundaries is sometimes poor. Perhaps more fundamentally, the two-way transmissibility at mesh interfaces afforded by RTI does not appear to have been addressed or attempted in the past.

## 5.2 One-Dimensional Replica Time Integrators

By way of motivation, we begin by introducing RTIs in the simple setting of one-dimensional linear wave propagation. Specifically, we consider the problem

$$\rho \frac{\partial^2 u}{\partial t^2} - C \frac{\partial^2 u}{\partial x^2} = f(x, t) \quad x \in [a, b], \quad t \in [0, T] \quad (5.1a)$$

$$u(a, t) = u_a(t) \text{ or } C \frac{\partial u}{\partial x}(a, t) = f_a(t) \quad t \in [0, T] \quad (5.1b)$$

$$u(b, t) = u_b(t) \text{ or } C \frac{\partial u}{\partial x}(b, t) = f_b(t) \quad t \in [0, T] \quad (5.1c)$$

$$u(x, 0) = u_0(x) \text{ and } \frac{\partial u}{\partial t}(x, 0) = v_0(x) \quad x \in [a, b] \quad (5.1d)$$

governing the propagation of linear waves over an interval  $[a, b]$  of the real line and over a time interval  $[0, T]$ . For instance, in applications to linear elastic waves  $u(x, t)$  is the displacement field,  $\rho$  is the mass density,  $C$  is a one-dimensional elastic modulus, which jointly give a wave celerity  $c = \sqrt{C/\rho}$ ,  $f(x, t)$  is a distribution of body forces,  $u_a(t)$  and  $u_b(t)$  are prescribed boundary displacements,  $f_a(t)$  and  $f_b(t)$  prescribed boundary forces, and  $u_0(x)$  and  $v_0(x)$  are initial displacements and velocities, respectively. The one-dimensional linear wave propagation problem just defined furnishes a simple and convenient framework in which to introduce many of the main concepts that lead to the formulation of RTIs. Extensions to general dimensions and non-linear systems are supplied in subsequent sections.

### 5.2.1 A Transmitting Finite-Element Scheme

Begin by considering the case of a space-time grid of size  $(\Delta x, \Delta t)$  that coarsens at  $x = 0$  to a space-time grid of size  $(n\Delta x, \Delta t)$  for some integer  $n > 1$ , Fig. 5.1. We particularly wish to devise a convergent space-time discretization of problem (5.1) that supports the solutions shown in Fig. 5.1a and b. These solutions represent *elementary signals* that are zero everywhere except on characteristic lines  $x = \pm ct$ , where the solutions take the value 1. Evidently, by superposition this condition suffices to ensure that general wave profiles can be transmitted listlessly across the interface. Indeed, any initial wave profile can be decomposed into *unit pulses*, i. e., profiles that are one at a single node

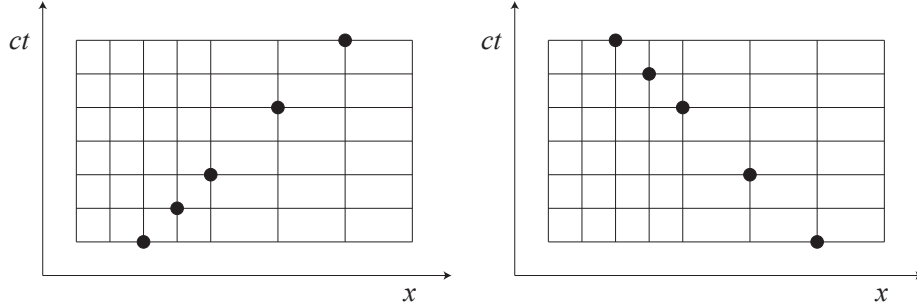


Figure 5.1: Space-time grid of size  $(\Delta x, \Delta t)$  that coarsens at  $x = 0$  to a space-time grid of size  $(2\Delta x, \Delta t)$ . Elementary signals that must be supported by the algorithm (signals are 1 at black dots, 0 elsewhere).

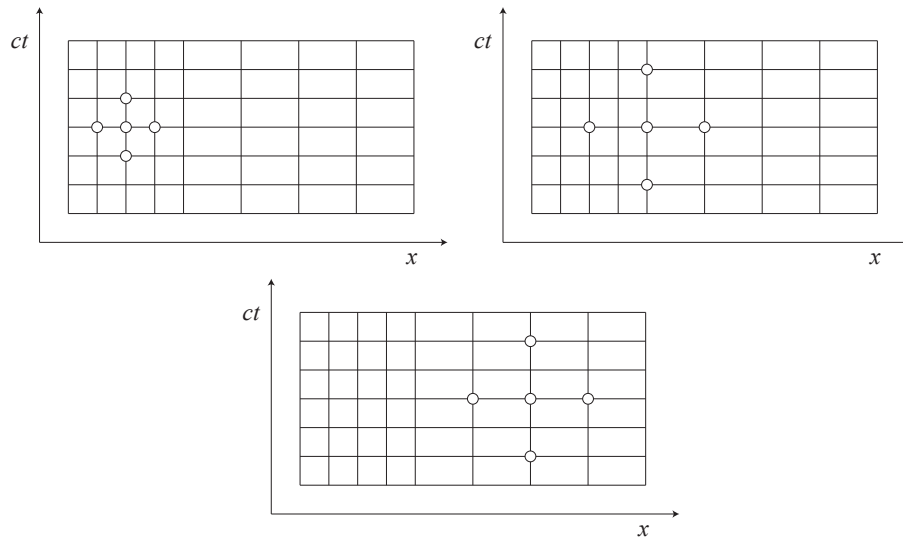


Figure 5.2: Finite-difference stencils that define a finite-difference scheme that transmits elementary signals across the interface in both directions.

in the spatial grid and zero elsewhere, and the corresponding solution at subsequent times follows by superposition of elementary signals.

A simple finite-differences scheme that satisfies the *transmissibility* requirement just formulated is shown in Fig. 5.2. The figure specifically depicts the finite-difference stencils that define the scheme, namely:

- (i) Interior point in fine grid,  $\alpha < 0$

$$\frac{u_{\alpha}^{i+1} - 2u_{\alpha}^i + u_{\alpha}^{i-1}}{\Delta t^2} - c^2 \frac{u_{\alpha+1}^i - 2u_{\alpha}^i + u_{\alpha-1}^i}{\Delta x^2} = 0 \quad (5.2)$$

(ii) Interface point,  $\alpha = 0$

$$\frac{u_0^{i+n} - 2u_0^i + u_0^{i-n}}{(n\Delta t)^2} - c^2 \frac{u_1^i - 2u_0^i + u_{-n}^i}{(n\Delta x)^2} = 0 \quad (5.3)$$

(iii) Interior point in coarse grid,  $\alpha > 0$

$$\frac{u_\alpha^{i+n} - 2u_\alpha^i + u_\alpha^{i-n}}{(n\Delta t)^2} - c^2 \frac{u_{\alpha+1}^i - 2u_\alpha^i + u_{\alpha-1}^i}{(n\Delta x)^2} = 0 \quad (5.4)$$

where  $u_\alpha^i$  denotes the discrete solution,  $\alpha$  enumerates grid points in the  $x$ -direction and  $i$  in the  $t$ -direction. It is readily verified that the finite-difference scheme thus defined indeed supports elementary signals provided that the Courant-Friedrichs-Lewy (CFL) identity

$$\frac{c\Delta t}{\Delta x} = 1 \quad (5.5)$$

is satisfied.

As already noted, the discrete solution corresponding to general initial conditions can then be obtained by superposition of elementary signals. This representation immediately shows that, if the initial velocities and strains are bounded, they remain uniformly bounded at all times and, hence, the scheme is stable.

### 5.2.2 Phase-Error Analysis

It is instructive to analyze the dispersion characteristics of the transmitting finite-difference scheme (5.2 - 5.4). For linear systems, phase-error analysis constitutes a conventional means of analyzing the convergence characteristics of numerical schemes for wave propagation problems (e. g., [109, 110]). Extensions of phase-error analysis to nonlinear systems and the relation between *phase-error convergence* and  $\Gamma$ -convergence have been investigated in [111].

Consider a wave of the form

$$u_{\alpha}^i = \Re \left\{ A_I^- e^{\iota(\omega^- i \Delta t - k^- \alpha \Delta x)} + A_R^- e^{\iota(\omega^- i \Delta t + k^- \alpha \Delta x)} \right\} \quad \alpha \leq 0 \quad (5.6a)$$

$$u_{\alpha}^i = \Re \left\{ A_T^+ e^{\iota(\omega^+ i \Delta t - k^+ \alpha n \Delta x)} \right\} \quad \alpha \geq 0 \quad (5.6b)$$

where  $A_I^-$  is the complex amplitude of the incident wave,  $A_R^-$  the complex amplitude of the reflected wave,  $A_T^+$  the complex amplitude of the transmitted wave,  $k^{\pm}$  are wave numbers,  $\omega^{\pm}$  frequencies, and we write  $\iota = \sqrt{-1}$ . Compatibility at the interface,  $\alpha = 0$ , requires

$$\omega^- = \omega^+ \equiv \omega \quad (5.7a)$$

$$A_I^- + A_R^- = A_T^+ \quad (5.7b)$$

Insertion of (5.6a) into (5.2) and of (5.6b) into (5.4) gives

$$\left( \cos(\omega \Delta t) - 1 \right) - \left( \frac{c \Delta t}{\Delta x} \right)^2 \left( \cos(k^- \Delta x) - 1 \right) = 0 \quad (5.8a)$$

$$\left( \cos(\omega n \Delta t) - 1 \right) - \left( \frac{c \Delta t}{\Delta x} \right)^2 \left( \cos(k^+ n \Delta x) - 1 \right) = 0 \quad (5.8b)$$

respectively. These discrete dispersion relations can be solved for the wave numbers  $k^{\pm}$  provided that the CFL condition

$$\frac{c \Delta t}{\Delta x} \leq 1 \quad (5.9)$$

is satisfied. Finally, (5.3) gives

$$2A_T^+ \left( \cos(\omega n \Delta t) - 1 \right) - \left( \frac{c \Delta t}{\Delta x} \right)^2 \left[ A_T^+ (e^{-\iota k^+ n \Delta x} - 2) + A_I^- e^{\iota k^- n \Delta x} + A_R^- e^{-\iota k^- n \Delta x} \right] = 0 \quad (5.10)$$

Given the amplitude  $A_I^-$  of the incident wave, the system of equations (5.7b) and (5.10) can be solved for the amplitudes  $A_R^-$  and  $A_T^+$  of the reflected and transmitted waves, respectively. Introducing the

complex representation

$$A_R^- = a_r + \iota a_i \quad A_T^+ = b_r + \iota b_i \quad (5.11)$$

equation (5.7b) yields

$$1 + a_r = b_r \quad a_i = b_i \quad (5.12)$$

where the amplitude of the incident wave  $A_T^-$  has been assumed real and equal to unity. For the real and imaginary parts of  $A_R^-$  we obtain

$$a_r = \frac{-\gamma_1^2 + \gamma_2\gamma_3}{\gamma_1^2 + \gamma_2^2} \quad (5.13a)$$

$$a_i = \frac{\gamma_1(\gamma_2 + \gamma_3)}{\gamma_1^2 + \gamma_2^2} \quad (5.13b)$$

where

$$\gamma_1 = \left(\frac{c\Delta t}{\Delta x}\right)^2 (\cos(k^+ n\Delta x) - \cos(k^- n\Delta x)) \quad (5.14a)$$

$$\gamma_2 = \left(\frac{c\Delta t}{\Delta x}\right)^2 (\sin(k^+ n\Delta x) + \sin(k^- n\Delta x)) \quad (5.14b)$$

$$\gamma_3 = \left(\frac{c\Delta t}{\Delta x}\right)^2 (\sin(k^- n\Delta x) - \sin(k^+ n\Delta x)) \quad (5.14c)$$

$$\arccos \left[ 1 + \left(\frac{c\Delta t}{\Delta x}\right)^2 (\cos(k^+ n\Delta x) - 1) \right] = n \arccos \left[ 1 + \left(\frac{c\Delta t}{\Delta x}\right)^2 (\cos(k^- \Delta x) - 1) \right] \quad (5.14d)$$

We verify that in the limit of  $\Delta t \rightarrow 0$ ,  $\Delta x \rightarrow 0$ , taken at  $\Delta x/\Delta t = \text{constant}$ , the discrete dispersion relations (5.8a) and (5.8b) reduce to

$$\omega \sim ck \quad (5.15)$$

which is the dispersion relation of the continuum. Thus, in the limit,  $k^\pm \rightarrow k = \omega/c$ ,  $|A_T^\pm| \rightarrow 1$  and  $|A_R^\pm| \rightarrow 0$  and, hence, (5.6a - 5.6b) converge to a solution of the problem (5.1).

The particular case in which the CFL identity (5.5) is satisfied is particularly simple and illuminating. In this case, the dispersion relations (5.8a) and (5.8b) are satisfied by the same wave

number

$$k^+ = k^- = \frac{\omega}{c} \equiv k \quad (5.16)$$

in agreement with the continuum dispersion relation (5.15), and (5.7b) and (5.10) are satisfied with

$$A_T^+ = A_T^- \equiv A \quad (5.17a)$$

$$A_R^+ = 0 \quad (5.17b)$$

Thus, the transmitting finite-difference scheme (5.2-5.4) is indeed fully transmitting when run at the CFL limit precisely. For instance, consider the case

$$k = \frac{\pi}{\Delta x} \quad (5.18a)$$

$$\omega = ck = \frac{\pi}{\Delta t} \quad (5.18b)$$

By this choice, (5.6a-5.6b) become

$$u_\alpha^i = \Re \left\{ A e^{\iota(i-\alpha)\pi} \right\} \quad \alpha \leq 0 \quad (5.19a)$$

$$u_\alpha^i = \Re \left\{ A e^{\iota(i-n\alpha)\pi} \right\} \quad \alpha \geq 0 \quad (5.19b)$$

Alternatively, this solution can be obtained directly by superposition of elementary signals of the type shown in Fig. 5.1. Remarkably, we observe that the incident wave (5.19a), which may be regarded as the highest-frequency and shortest-wavelength *phonon* supported by the fine space-time grid, is fully transmitted through the interface despite being unresolved by the coarse spatial grid. However, the nature of the representation of the wave changes radically as it traverses the interface, see Fig. 5.3. Thus, on the coarse spatial grid region the field  $u_\alpha^i$  is spatially uniform, i. e., independent of  $\alpha$ , and takes the values  $\pm 1$  alternately. We note that these are precisely the values taken by the incoming wave on the fine grid. In this manner, the coarse spatial grid manages to record a list of values describing the structure of incoming unresolved phonons. An interpretation of such records

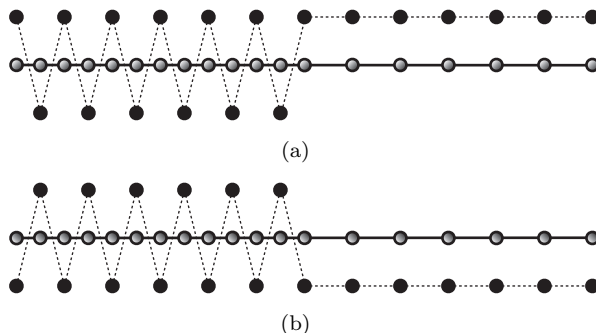


Figure 5.3: The two states of the solution of the transmitting finite-difference scheme (5.2-5.4) run at the CFL limit (5.5) for an incoming phonon unresolved by the coarse spatial mesh.

as statistical samples will be developed in the next section.

It is readily verified that a wave of the form

$$u_{\alpha}^i = \Re \left\{ A e^{i(i+\alpha)\pi} \right\} \quad \alpha \leq 0 \quad (5.20a)$$

$$u_{\alpha}^i = \Re \left\{ A e^{i(i+n\alpha)\pi} \right\} \quad \alpha \geq 0 \quad (5.20b)$$

is also a solution of (5.2-5.4) at the CFL limit (5.5). In particular, a wave of the form (5.20b) is fully transmitted into the fine spatial grid, where it synthesizes into the high-frequency phonon (5.20a). Solutions (5.19a-5.19b) and (5.20a-5.20b) provide a first illustration of two-way convertibility of unresolved phonons into statistical samples.

In general, the amplitude  $|A_R^+|$  of the reflected wave, or reflection coefficient, is a function of the Courant number (5.5). Fig. 5.4 depicts the reflection coefficient as a function of the coarsening ratio and the Courant number. Reflection coefficients corresponding to the central difference scheme are also shown for comparison (cf., e. g., [112]). It is interesting to note from the figure that the reflection coefficient reduces to zero for a coarsening ratio  $n = 1$ , corresponding to a uniform grid. Furthermore, the RTI reflection coefficient tends to zero as the Courant number tends to one, which shows that RTIs are exactly transmitting in that limit. For general values of the Courant number and coarsening ratio the RTI scheme clearly outperforms central differences as regards the extent of numerical reflection at the interface.

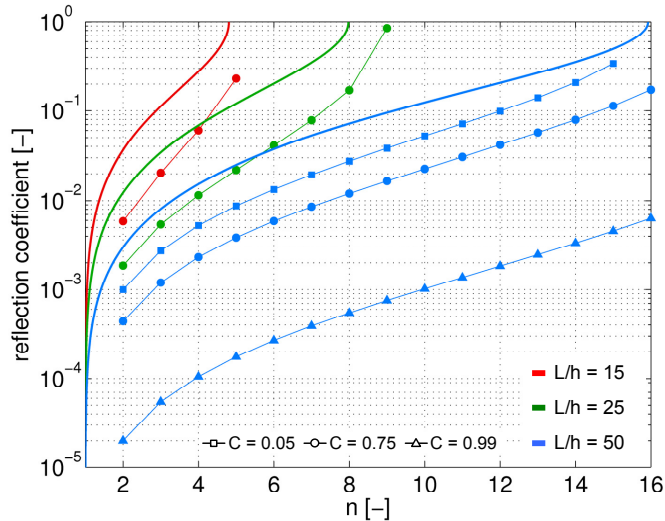


Figure 5.4: Magnitude of the reflected wave amplitude  $|A_R^+|$ , or reflection coefficient, vs. the ratio  $n$  of coarse to fine grid size for three different number of points per wavelength,  $L/h = L/\Delta x = 2\pi/\Delta x/k^-$ , and Courant numbers  $C = 0.05$  (squares),  $0.75$  (circles) and  $0.99$  (triangles). Lines without symbols correspond to central differences.

### 5.2.3 Replica Reinterpretation

We now proceed to reinterpret the transmitting finite-difference scheme (5.2-5.4) as a *replica time-integration* (RTI) scheme. To this end, we note that, in the coarse space-time grid, the finite-difference scheme (5.4) *decouples* into independent central-difference schemes for  $n$  replicas  $\{(\alpha, jn + k), \alpha \geq 0, j \in \mathbb{Z}, k = 0, \dots, n - 1\}$  of a space-time grid of size  $(n\Delta x, n\Delta t)$ . This decomposition is shown schematically in Fig. 5.5, which shows a fine space-time grid on the left and a replica ensemble (of multiplicity 3) on the right, separated by an interface. The  $k$ th replica in the ensemble may be regarded as a *copy* of a space-time grid of size  $(n\Delta x, n\Delta t)$  shifted in time by  $k\Delta t$ ,  $k = 0, \dots, n - 1$ . Each replica is capable of absorbing from the fine region the elementary signal that is in phase with the replica. Conversely, each replica is capable of supporting –and transmitting to the fine region– an elementary signal of a certain phase. A general wave exiting the fine grid is distributed over the replicas, and this distribution may be regarded as a specific realization, or sample, of a *statistical ensemble*. Conversely, a general collection of waves exiting the replica ensemble is synthesized into a general wave in the fine grid.

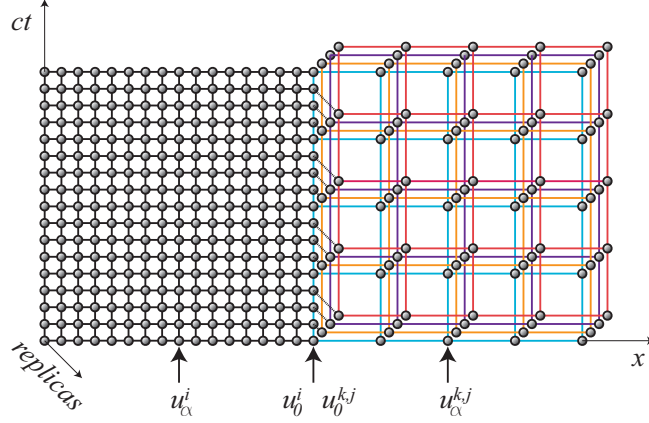


Figure 5.5: Replica re-interpretation of the time-integration scheme shown in Fig. 5.2. The schematic shows the interface between the fine and coarse spatial grids and the replica ensemble (color-coded) used to represent solutions over the coarse spatial grid.

It is illuminating to reinterpret solution (5.19a-5.19b) within the replica representation. We recall that in this solution the incoming wave (5.19a) consists of a phonon that is unresolved by the coarse spatial grid. Under these conditions, the coarse solution is spatially uniform and alternates between the values taken by the incoming wave, Fig. 5.3. In the replica representation, each value of (5.19b) is picked up by a different replica in the ensemble. In this manner, the coarse solution may be regarded as a *sampling*, in the sense of statistical physics (cf., e. g., [92] for theories of statistical physics based on replica ensembles), of incoming phonons whose wavelengths are too short to be resolved by the coarse mesh. Thus, RTIs solve the transmissibility problem between regions of different spatial resolution by setting up replica ensembles on the coarse regions of the grid and by the two-way conversion between short-wavelength phonons and statistical samples.

---

**Algorithm 1:** Replica implementation of the one-dimensional transmitting scheme

---

- 1: For given  $i$ , set  $j = \lfloor i/n \rfloor$ ,  $k = (i \bmod n)$ ,  $u_0^i = u_0^{k,j}$  and  $u_{-1}^{k,j} = u_{-n}^i$
  - 2: For  $\alpha < 0$ ,  $u_\alpha^{i+1} = 2u_\alpha^i - u_\alpha^{i-1} + \left(\frac{c\Delta t}{\Delta x}\right)^2 (u_{\alpha-1}^i - 2u_\alpha^i + u_{\alpha+1}^i)$
  - 3: For  $\alpha \geq 0$ ,  $u_\alpha^{k,j+1} = 2u_\alpha^{k,j} - u_\alpha^{k,j-1} + \left(\frac{c\Delta t}{\Delta x}\right)^2 (u_{\alpha-1}^{k,j} - 2u_\alpha^{k,j} + u_{\alpha+1}^{k,j})$
- 

A replica implementation of the one-dimensional transmitting finite-difference scheme (5.2-5.4) is shown in Algorithm 1. In this implementation, the solution is composed of the solution  $\{u_\alpha^i, \alpha \leq 0, i \in \mathbb{Z},\}$  over the fine space-time grid, and the solutions  $\{u_\alpha^{k,j}, \alpha \geq -1, j \in \mathbb{Z}, k = 0, \dots, n-1\}$

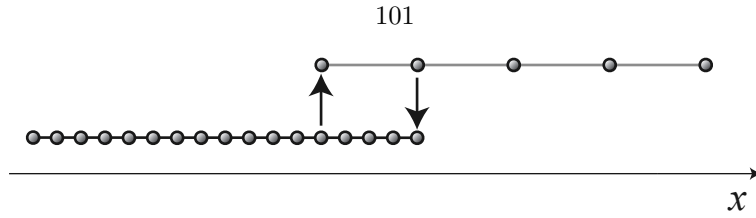


Figure 5.6: Schematic of master-slave relation of overlap implementation of RTIs. The up-down arrows point from master grid points to slave grid points.

over each of the  $n$  replicas of the coarse space-time grid. The fine solution extends up to the interface and the replicas extend beyond the interface over a coarse spatial grid size  $n\Delta x$ . In particular, the replicas and the fine solution overlap over the region  $-n\Delta x \leq x \leq 0$ . Step (i) in Algorithm 1 *activates* the replica  $k$  in phase with time  $i$ . For  $\alpha < 0$  the solution over the fine grid proceeds as in the standard central difference scheme with the value of  $u_0^i$  at the interface set by the replicas, i. e., set to  $u_0^{k,j}$ . The solution over each of the replicas also proceeds as in the standard central difference scheme with the value of  $u_{-1}^{k,j}$  set by the fine solution, i. e., set to  $u_{-n}^i$ . Thus, the point  $\alpha = 0$  of the fine grid is tied—or slave—to the coarse-grid replicas, whereas the point  $\alpha = -1$  of the replicas is tied—or slave—to the fine grid. This master-slave relation between the fine grid and the replicas is shown schematically in Fig. 5.6.

In closing this section we note that, whereas the introduction of an overlap region is not strictly necessary for defining the RTI in a finite-difference setting, it will prove convenient in extensions of the RTIs to nonlinear systems and to higher dimensions and, accordingly, we adopt the device from the outset. It also bears emphasis that the RTI scheme just described is simply a reinterpretation of the transmitting finite-difference scheme (5.2-5.4), and that both schemes are in fact identical. In particular, it thus follows that all the convergence properties of the transmitting finite-difference scheme carry over unchanged to the RTI scheme.

#### 5.2.4 Complexity of One-Dimensional RTIs

Whereas the  $n$ -fold replication of the coarse grid that is the basis of RTIs increases the computational complexity of the schemes by a factor of  $n$  with respect to central differences on a single coarse grid, a net speed-up factor of  $n$  still remains with respect to central differences on the fine grid.

We may regard the  $n$ -fold slow-down resulting from replication as the price to pay for two-way transmissibility across the interface. However, the processing of the replicas is trivially parallelizable, and a straightforward parallel implementation may be expected to afford a speed-up of  $O(n)$  in execution time. Thus, the execution times for parallel RTIs may be expected to exhibit a speed-up factor of  $O(n^2)$ , i. e., to be comparable to the execution times for sequential central differences on a single coarse space-time grid.

### 5.2.5 Numerical Examples

In this section we illustrate the interconvertibility of high-frequency thermal vibrations and heat afforded by RTIs by means of simple one-dimensional examples. The system consists of two regions of equal length, with a fine grid on the left of the interface and a four-fold coarser grid on the right. In all calculations the time step  $\Delta t$  is selected so as to satisfy the CFL condition exactly (Courant number = 1).

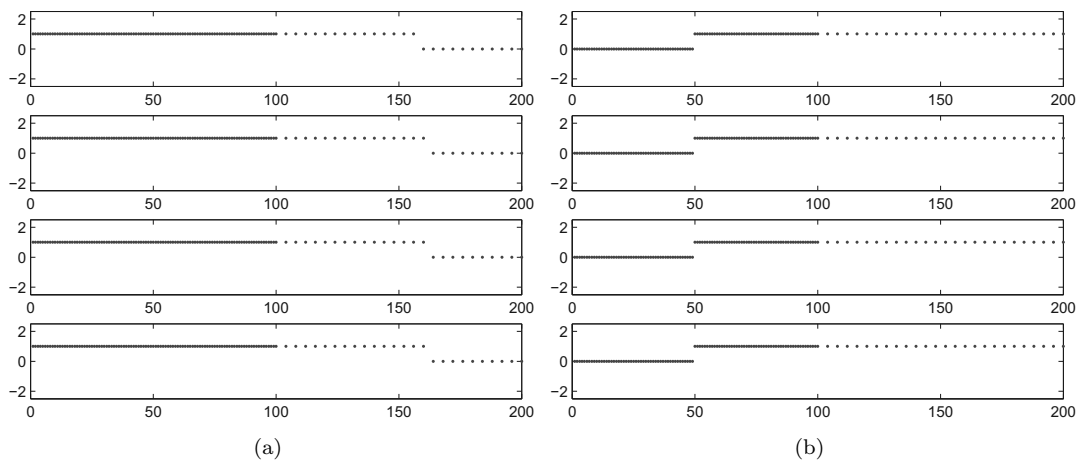


Figure 5.7: One-dimensional grid consisting of two regions of equal length, a fine grid on the left of the interface and a four-fold coarser grid on the right. Four replicas of the coarse grid are used in the solution. a) Snapshot of step wave after the transmission from the fine to the coarse grid. b) Snapshot of step wave after transmission from the coarse to the fine grid.

Figure 5.7 shows the simple test of a step wave. Figure 5.7a shows a snapshot of a right-going step wave after its transmission across the interface. As may be seen from the figure, the step wave is transmitted exactly across the interface. This exact transmissibility is remarkable in view of the

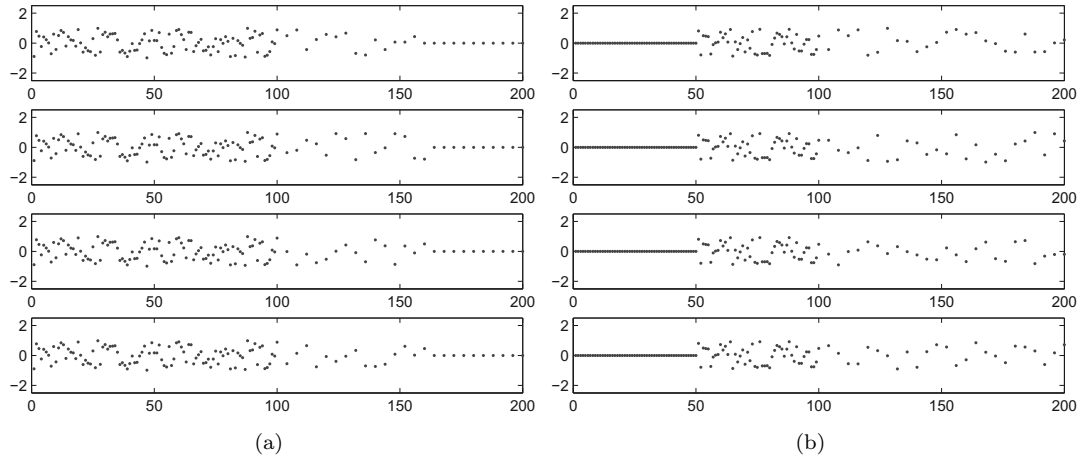


Figure 5.8: One-dimensional grid consisting of two regions of equal length, a fine grid on the left of the interface and a four-fold coarser grid on the right. Four replicas of the coarse grid are used in the solution. a) Snapshot of arbitrary wave after the transmission from the fine to the coarse grid. b) Snapshot of arbitrary wave after transmission from the coarse to the fine grid.

inability of a single coarse grid to resolve and support the incoming step wave. Indeed, only by the simultaneous operation of all four replicas can the step wave be absorbed exactly by the coarse grid. Fig. 5.7b shows a snapshot of a left-going step wave after its transmission across the interface. Such a wave is generated, e. g., by the reflection from the right boundary of a left-going step wave generated on the fine grid. As may be seen from the figure, all out-of-phase replica waves recombine at the interface to reconstruct a perfect step wave on the fine grid. This simple test illustrates the two-way transmissibility of phonons between fine and coarse grids afforded by RTIs.

Since, in the linear range, any arbitrary wave can be represented as a superposition of step waves, it follows that the two-way transmissibility property of RTIs holds for arbitrary waves as well. As a simple illustration of this property, Fig. 5.8 shows arbitrary waves being transmitted listlessly across the interface, both from the fine to the coarse grid, Fig. 5.8a, and from the coarse to the fine, Fig. 5.8b. As in the case of step waves discussed previously, the interface effectively *splits* signals arriving from the fine grid into out-of-phase components carried by the replicas of the coarse grid and, conversely, combines signals arriving from the coarse-grid replicas into a single signal on the fine grid.

Next, we illustrate the replica ensemble aspect of RTIs and how such replica ensembles could

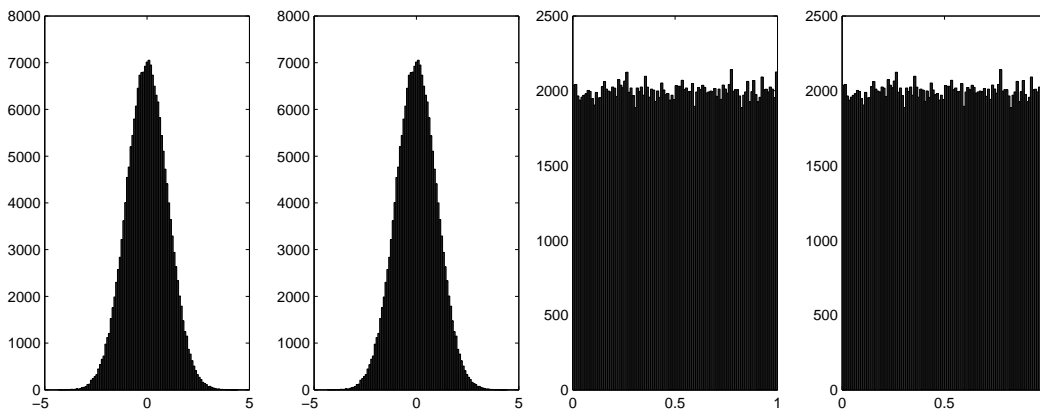


Figure 5.9: One-dimensional grid consisting of two regions of equal length, a fine grid on the left of the interface and a hundred-fold coarser grid on the right. A hundred replicas of the coarse grid are used in the solution. Histograms of signal values on all points of the fine and coarse grids after transmission of the signal transmission across the interface. a) Normally distributed random signal. b) Uniformly distributed random signal.

be used to simulate heat transfer across mesh interfaces. To this end, we consider a test case as in the foregoing but with a coarsening-ratio of 100, i. e., the coarse-grid size is a hundred times larger than the fine-grid size. In particular, the coarse grid is now replicated 100 times, which begins to provide a modicum of statistical sampling of the solution. Two types of random signals, normally and uniformly distributed, are inserted into the system through the left boundary. Histograms of the signal values on all points of the fine and coarse grids after transmission of the signal transmission across the interface are shown in Fig. 5.9. We may regard the signal on the fine grid as consisting of thermal phonons that cannot be resolved or carried by one single coarse grid. As is evident from Fig. 5.9, such thermal phonons are absorbed by the coarse grid by populating the replica ensemble. After transmission through the mesh boundary, the statistical properties of the replica ensemble are identical to those of the incident thermal phonons. This interconvertibility between phonons and replica ensembles is entirely reversible. In particular, an ensemble of replica waves inserted through the right boundary of the domain recombine at the mesh interface and are transmitted listlessly into the fine region as a distribution of thermal phonons of identical statistical characteristics.

### 5.2.6 A Benchmark Test

For purposes of comparison with other work, we close this section by considering a one-dimensional test proposed by Belytschko et al. [91]. The test consists of a domain of 748.75 Å in length divided into two regions: a fine region on the left of grid size 1.25 Å containing 300 nodes; and a coarse region containing 150 nodes at twice the grid size. The elastic modulus of the material is  $E = 11.66$  eV/Å<sup>3</sup> and the wave speed is  $c = 372.82$  Å/ps. By way of excitation, the displacement boundary condition

$$u_z(t) = \begin{cases} a_1 [1 + \cos \{\pi + 2\pi a_2 (100 - ct)\}] [1 + a_3 \cos (2\pi a_4 ct)] & ct \leq 100 \text{ Å} \\ 0 & \text{otherwise} \end{cases} \quad (5.21)$$

containing a combination of high and low frequency modes is applied to the left boundary, where  $a_1 = 0.00617$  Å,  $a_2 = 0.01$  Å<sup>-1</sup>,  $a_3 = 0.1$  and  $a_4 = 1.0$  Å<sup>-1</sup>.

Fig. 5.10 shows the results of RTI calculations run exactly at the CFL limit,  $\Delta t = 6.7 \times 10^{-3}$  ps. The subfigures show the common fine-grid solution and each of the replica solutions. As may be seen from the figure, the waves are transmitted exactly across the interface in both directions, with each replica capturing its in-phase component. By way of comparison, Fig. 5.11 shows a conventional central differences solution with edge-to-edge coupling, i. e., with the fine and coarse grids attached at a single node. The calculation is run at the CFL of the fine grid. As expected, the high frequency component of the incoming wave is largely reflected by the interface.

## 5.3 Extension to Multiple Dimensions

We now proceed to formulate RTIs in arbitrary dimensions. The formulation follows along the same lines as in the introductory one-dimensional case discussed in the foregoing, namely, we start by formulating a convergent and transmitting time-integration scheme and then proceed to re-interpret it in terms of replica ensembles. Whereas the schemes formulated in this section are dimension-independent, we describe them in two dimensions for ease of exposition. Likewise, whereas the

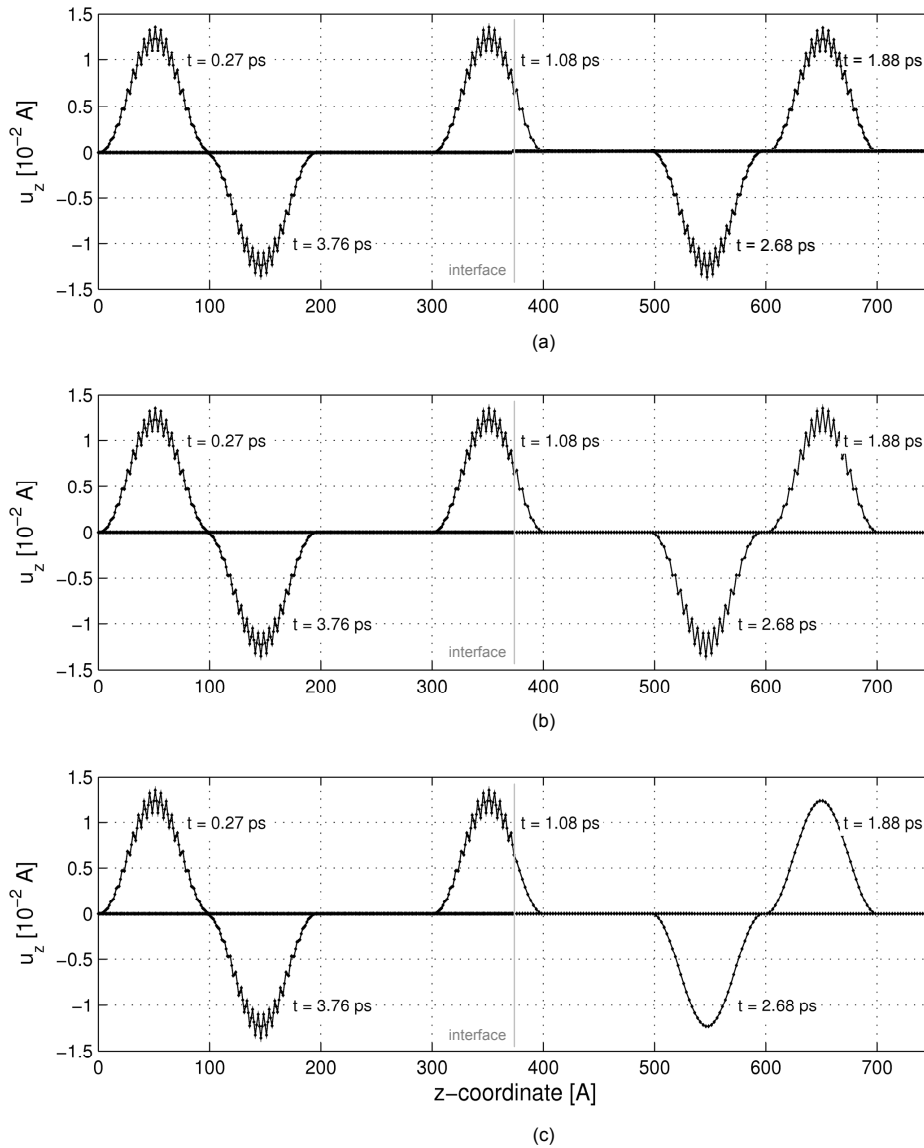


Figure 5.10: One-dimensional benchmark test of Belytschko et al. [91], consisting of a fine grid on the left of the domain attached to a two-fold coarser grid on the right and subjected to harmonic excitation at the left boundary. a) RTI solution. b) and c) Individual replica components of the RTI solution.

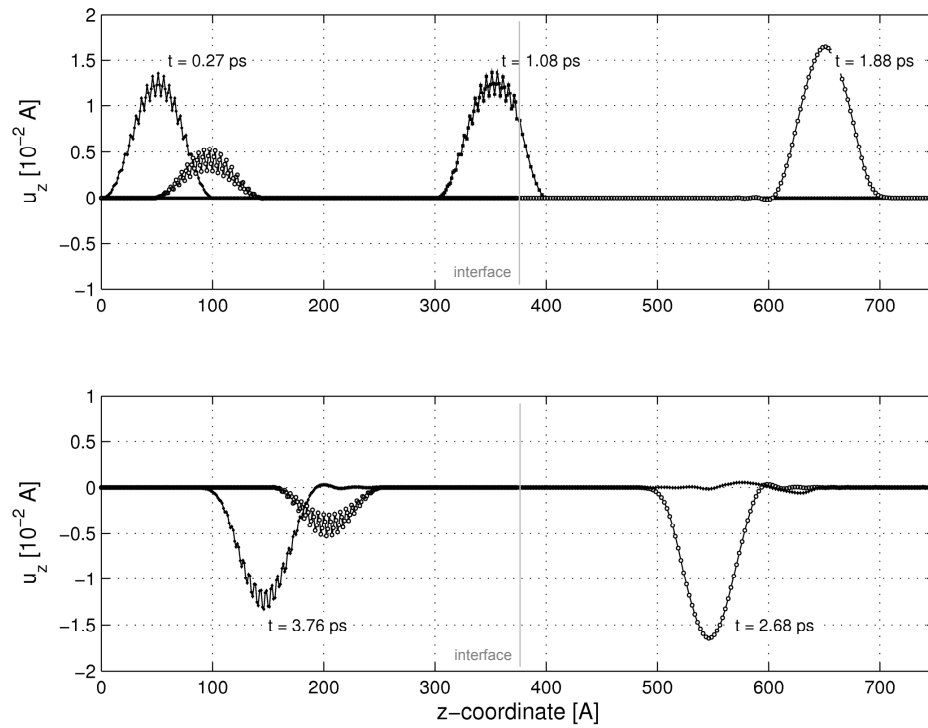


Figure 5.11: One-dimensional benchmark test of Belytschko et al. [91], consisting of a fine grid on the left of the domain attached to a two-fold coarser grid on the right and subjected to harmonic excitation at the left boundary. Central differences solution.

schemes apply just as well to linear and non-linear problems, we formulate them in the linear range in the interest of simplicity. Specifically, we consider the problem

$$\rho \frac{\partial^2 u}{\partial t^2} - C \left( \frac{\partial^2 u}{\partial x^2} + \frac{\partial^2 u}{\partial y^2} \right) = f(x, y, t) \quad (x, y) \in V \subset \mathbb{R}^2, \quad t \in [0, T] \quad (5.22a)$$

$$u(x, y, t) = g(x, y, t) \text{ or } C \frac{\partial u}{\partial n}(x, y, t) = h(x, y, t) \quad (x, y) \in \partial V, \quad t \in [0, T] \quad (5.22b)$$

$$u(x, y, 0) = u_0(x, y) \text{ and } \frac{\partial u}{\partial t}(x, y, 0) = v_0(x, y) \quad (x, y) \in V \quad (5.22c)$$

governing the propagation of linear waves over an domain  $V \subset \mathbb{R}^2$  and over a time interval  $[0, T]$ . For instance, in applications to linear elastic waves over a membrane  $u(x, y, t)$  is the deflection field,  $\rho$  is the mass density,  $C$  is a one-dimensional elastic modulus, which jointly give a wave celerity  $c = \sqrt{C/\rho}$ ,  $f(x, y, t)$  is a distribution of body forces,  $g(x, y, t)$  is the prescribed boundary deflection,  $h(x, y, t)$  the prescribed boundary forces, and  $u_0(x, y)$  and  $v_0(x, y)$  are initial displacements and velocities, respectively.

### 5.3.1 A Transmitting Time-Integration Scheme

A simple extension of the 1D finite-differences scheme presented in Section 5.2 is shown in Fig. 5.12.

The figure specifically depicts the finite-difference stencils that define the scheme, namely:

- (i) Interior point in fine grid,  $\alpha < -1$ ,  $\beta \in \mathbb{Z}$ ,

$$\frac{u_{\alpha,\beta}^{i+1} - 2u_{\alpha,\beta}^i + u_{\alpha,\beta}^{i-1}}{\Delta t^2} - c^2 \left[ \frac{u_{\alpha+1,\beta}^i - 2u_{\alpha,\beta}^i + u_{\alpha-1,\beta}^i}{\Delta x^2} + \frac{u_{\alpha,\beta+1}^i - 2u_{\alpha,\beta}^i + u_{\alpha,\beta-1}^i}{\Delta y^2} \right] = 0 \quad (5.23)$$

- (ii) Interface points in fine grid,  $\alpha = -1$ ,

- (a)  $\beta \in n\mathbb{Z}$ ,

$$\frac{u_{-1,\beta}^{i+1} - 2u_{-1,\beta}^i + u_{-1,\beta}^{i-1}}{\Delta t^2} - c^2 \left[ \frac{u_{0,\beta}^i - 2u_{-1,\beta}^i + u_{-2,\beta}^i}{\Delta x^2} + \frac{u_{-1,\beta+1}^i - 2u_{-1,\beta}^i + u_{-1,\beta-1}^i}{\Delta y^2} \right] = 0 \quad (5.24)$$

(b)  $\beta \in n\mathbb{Z}$ ,  $l = 1, \dots, n-1$ ,

$$\begin{aligned} & \frac{u_{-1,\beta+l}^{i+1} - 2u_{-1,\beta+l}^i + u_{-1,\beta+l}^{i-1}}{\Delta t^2} - c^2 \left[ \frac{2l u_{-1,\beta+n}^i - 2n u_{-1,\beta+l}^i + 2(n-l) u_{-1,\beta}^i}{nl(n-l)\Delta y^2} \right] - \\ & c^2 \left[ \frac{(l u_{0,\beta+n}^i + (n-l) u_{0,\beta}^i) - (l u_{-1,\beta+n}^i + n u_{-1,\beta+l}^i + (n-l) u_{-1,\beta}^i) + n u_{-2,\beta+l}^i}{n\Delta x^2} \right] = 0 \end{aligned} \quad (5.25)$$

(iii) Interface points in coarse grid,  $\alpha = 0$ ,  $\beta \in n\mathbb{Z}$ ,

$$\frac{u_{0,\beta}^{i+n} - 2u_{0,\beta}^i + u_{0,\beta}^{i-n}}{(n\Delta t)^2} - c^2 \left[ \frac{u_{1,\beta}^i - 2u_{0,\beta}^i + u_{-n,\beta}^i}{(n\Delta x)^2} + \frac{u_{0,\beta+n}^i - 2u_{0,\beta}^i + u_{0,\beta-n}^i}{(n\Delta y)^2} \right] = 0 \quad (5.26)$$

(iv) Interior points in coarse grid,  $\alpha > 0$ ,  $\beta \in n\mathbb{Z}$ ,

$$\frac{u_{\alpha,\beta}^{i+n} - 2u_{\alpha,\beta}^i + u_{\alpha,\beta}^{i-n}}{(n\Delta t)^2} - c^2 \left[ \frac{u_{\alpha+1,\beta}^i - 2u_{\alpha,\beta}^i + u_{\alpha-1,\beta}^i}{(n\Delta x)^2} + \frac{u_{\alpha,\beta+n}^i - 2u_{\alpha,\beta}^i + u_{\alpha,\beta-n}^i}{(n\Delta y)^2} \right] = 0 \quad (5.27)$$

where we consider the unforced case  $f = 0$  for simplicity. As in the one-dimensional case,  $u_{\alpha,\beta}^i$  denotes the discrete solution,  $\alpha$  enumerates grid points in the  $x$ -direction,  $\beta$  in the  $y$ -direction and  $i$  in the  $t$ -direction. The coefficients of the scheme are chosen so that plane-wave analogs of the elementary signals of figures 5.1a and b are exact solutions for both normal and tangential incidence in the limit of a CFL number = 1. As in the one-dimensional case, this construction ensures the two-way transmissibility of waves across the mesh interface. However, a critical difference with respect to the one-dimensional case is the presence of a transition or buffer layer disposed along the mesh interface, cf. middle-right stencil in Fig. 5.12.

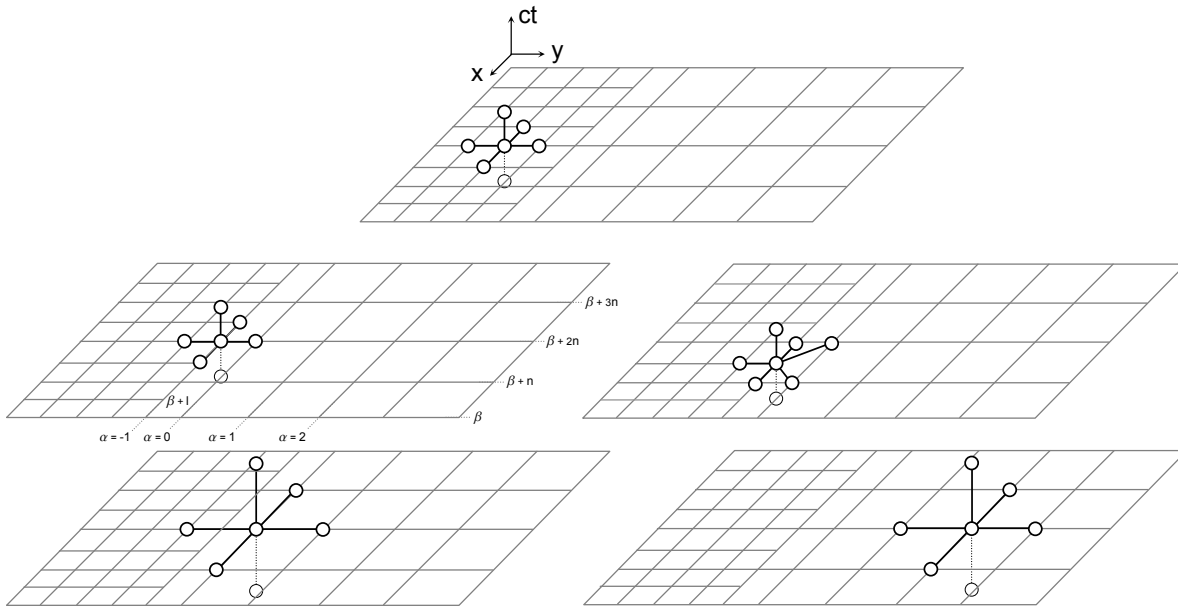


Figure 5.12: Finite-difference stencils defining a finite-difference scheme that transmits elementary signals across a mesh interface in both directions. Coarsening ratio  $n = 2$ .

### 5.3.2 Phase-Error Analysis

We proceed to analyze the dispersion characteristics of the two-dimensional transmitting finite-difference scheme (5.23 - 5.27). To this end, we consider waves of the form

$$w_{\alpha,\beta}^i = \Re \left\{ A_I^- e^{\iota(\omega^- i \Delta t - k^- \alpha \Delta x \cos \theta + k^- \beta \Delta y \sin \theta)} \right\} + \Re \left\{ A_R^- e^{\iota(\omega^- i \Delta t + k^- \alpha \Delta x \cos \theta + k^- \beta \Delta y \sin \theta)} \right\} \quad \alpha \leq -1 \quad (5.28a)$$

$$w_{\alpha,\beta}^i = \Re \left\{ A_T^+ e^{\iota(\omega^+ i \Delta t - k^+ \alpha n \Delta x \cos \theta + k^+ \beta \Delta y \sin \theta)} \right\} \quad \alpha \geq 0 \quad (5.28b)$$

where  $A_I^-$  is the complex amplitude of the incident wave,  $A_R^-$  the complex amplitude of the reflected wave,  $A_T^+$  the complex amplitude of the transmitted wave,  $k^\pm$  are wave numbers,  $\omega^\pm$  frequencies,  $\theta$  is the angle the incident wave subtends to the horizontal axis, and we write  $\iota = \sqrt{-1}$ . Insertion of (5.28a) into (5.23) and of (5.28b) into (5.27) gives

$$(\cos(\omega^- \Delta t) - 1) - \left( \frac{c \Delta t}{\Delta x} \right)^2 (\cos(k^- \Delta x \cos \theta) - 1) - \left( \frac{c \Delta t}{\Delta y} \right)^2 (\cos(k^- \Delta y \sin \theta) - 1) = 0 \quad (5.29)$$

and

$$(\cos(\omega^+ n \Delta t) - 1) - \left(\frac{c \Delta t}{\Delta x}\right)^2 (\cos(k^+ n \Delta x \cos \theta) - 1) - \left(\frac{c \Delta t}{\Delta y}\right)^2 (\cos(k^+ n \Delta y \sin \theta) - 1) = 0 \quad (5.30)$$

These discrete dispersion relations can be solved for the wave numbers  $k^\pm$  provided that the two-dimensional CFL condition

$$\frac{c \Delta t}{\Delta x} \cos \theta + \frac{c \Delta t}{\Delta y} \sin \theta \leq 1 \quad (5.31)$$

is satisfied. For square meshes ( $\Delta x = \Delta y = h$ ), this condition reduces to the simpler form

$$\frac{c \Delta t}{h} (\cos \theta + \sin \theta) \leq 1 \quad (5.32)$$

Insertion of (5.28a) and (5.28b) into (5.24) gives

$$\begin{aligned} & 2 \cos(k^- \Delta x \cos \theta) e^{\iota(k^- \beta \Delta y \sin \theta)} [A_I^- e^{\iota(k^- \Delta x \cos \theta)} + A_R^- e^{-\iota(k^- \Delta x \cos \theta)}] - \\ & A_T^+ e^{\iota(k^+ \beta \Delta y \sin \theta)} - e^{\iota(k^- \beta \Delta y \sin \theta)} [A_I^- e^{2\iota(k^- \Delta x \cos \theta)} + A_R^- e^{-2\iota(k^- \Delta x \cos \theta)}] = 0 \end{aligned} \quad (5.33)$$

whereas insertion into (5.25) gives

$$\begin{aligned} & e^{\iota(k^- (\beta+l) \Delta y \sin \theta)} \left( A_I^- e^{\iota(k^- \Delta x \cos \theta)} + A_R^- e^{-\iota(k^- \Delta x \cos \theta)} \right) \cdot \\ & \left[ \left( \frac{c \Delta t}{\Delta x} \right)^2 \left\{ 2 \cos(k^- \Delta x \cos \theta) - 1 + \frac{l}{n} e^{\iota(k^- (n-l) \Delta y \sin \theta)} + \left( 1 - \frac{l}{n} \right) e^{-\iota(k^- l \Delta y \sin \theta)} \right\} \right] + \\ & e^{\iota(k^- (\beta+l) \Delta y \sin \theta)} \left( A_I^- e^{\iota(k^- \Delta x \cos \theta)} + A_R^- e^{-\iota(k^- \Delta x \cos \theta)} \right) \cdot \\ & \left[ 2 \left( \frac{c \Delta t}{\Delta y} \right)^2 \left\{ (\cos(k^- \Delta y \sin \theta) - 1) - \frac{1}{n(n-l)} e^{\iota(k^- (n-l) \Delta y \sin \theta)} + \frac{1}{l(n-l)} - \frac{1}{nl} e^{-\iota(k^- l \Delta y \sin \theta)} \right\} \right] - \\ & e^{\iota(k^- (\beta+l) \Delta y \sin \theta)} \left( \frac{c \Delta t}{\Delta x} \right)^2 \left( A_I^- e^{2\iota(k^- \Delta x \cos \theta)} + A_R^- e^{-2\iota(k^- \Delta x \cos \theta)} \right) - \\ & e^{\iota(k^+ (\beta+l) \Delta y \sin \theta)} \left( \frac{c \Delta t}{\Delta x} \right)^2 A_T^+ \left( \frac{l}{n} e^{\iota(k^+ (n-l) \Delta y \sin \theta)} + \left( 1 - \frac{l}{n} \right) e^{-\iota(k^+ l \Delta y \sin \theta)} \right) = 0 \end{aligned} \quad (5.34)$$

Finally, from (5.26) we find

$$A_T^+ e^{\iota(k^+ n \Delta x \cos \theta + k^+ \beta \Delta y \sin \theta)} - e^{\iota(k^- \beta \Delta y \sin \theta)} \left( A_T^- e^{\iota(k^- n \Delta x \cos \theta)} + A_R^- e^{-\iota(k^- n \Delta x \cos \theta)} \right) = 0 \quad (5.35)$$

Time-independent reflection coefficients require  $\omega^- = \omega^+ \equiv \omega$ , which yields a complex equation relating the wave numbers  $k^+$  and  $k^-$  from the discrete dispersion relations (5.29 - 5.30). For square meshes ( $\Delta x = \Delta y = h$ ) and incident waves aligned with the horizontal axis ( $\theta = 0$ ), equations (5.33) and (5.34) become redundant. Therefore  $A_R^-$ ,  $A_T^+$  and  $k^+$  can be found from equations (5.33), (5.35) and (5.29-5.30), assuming  $A_T^+ = 1$ . Reflection coefficients for four angles of incidence  $\theta$  and three Courant numbers  $C$  are depicted in Fig. 5.13. For  $\theta = 0$  we verify that the reflection coefficients are identical to those of the one-dimensional RTI scheme, Fig. 5.4. The reflection coefficients for oblique incidence follow similar trends. Thus, the reflection coefficients properly tend to zero as the Courant number tends to one. As expected, the reflection coefficient also reduces to zero for a coarsening ratio  $n = 1$ , corresponding to a uniform grid. Finally, reflection coefficients remain below 0.2 for systems containing up to 5 replicas, even for waves poorly described in the fine region (i. e., those with  $L/h = 15$  point per wavelength) and regardless of the angle of incidence  $\theta$  and the Courant number  $C$  (except for  $\theta = 0$ ,  $C = 0.05$ ). The last statement is encouraging because incidence angles are usually not known *a priori* for unstructured mesh interfaces.

Finally, a straightforward calculation shows that the discrete dispersion relations (5.29) and (5.30) reduce to

$$\omega^- \sim ck^-, \quad \omega^+ \sim ck^+, \quad (5.36)$$

respectively, in the limit of  $\Delta t \rightarrow 0$  and  $h \rightarrow 0$  taken at  $h/\Delta t = \text{constant}$ . Since  $\omega^- = \omega^+ \equiv \omega$ , it further follows that  $\omega \sim ck$ . In addition, we have numerically verified that—in the limit—the reflection coefficient ( $|A_R^+|$ ) goes to zero. Thus, both the continuum dispersion and reflection relations are satisfied in the limit, an indication of the convergence of the scheme.

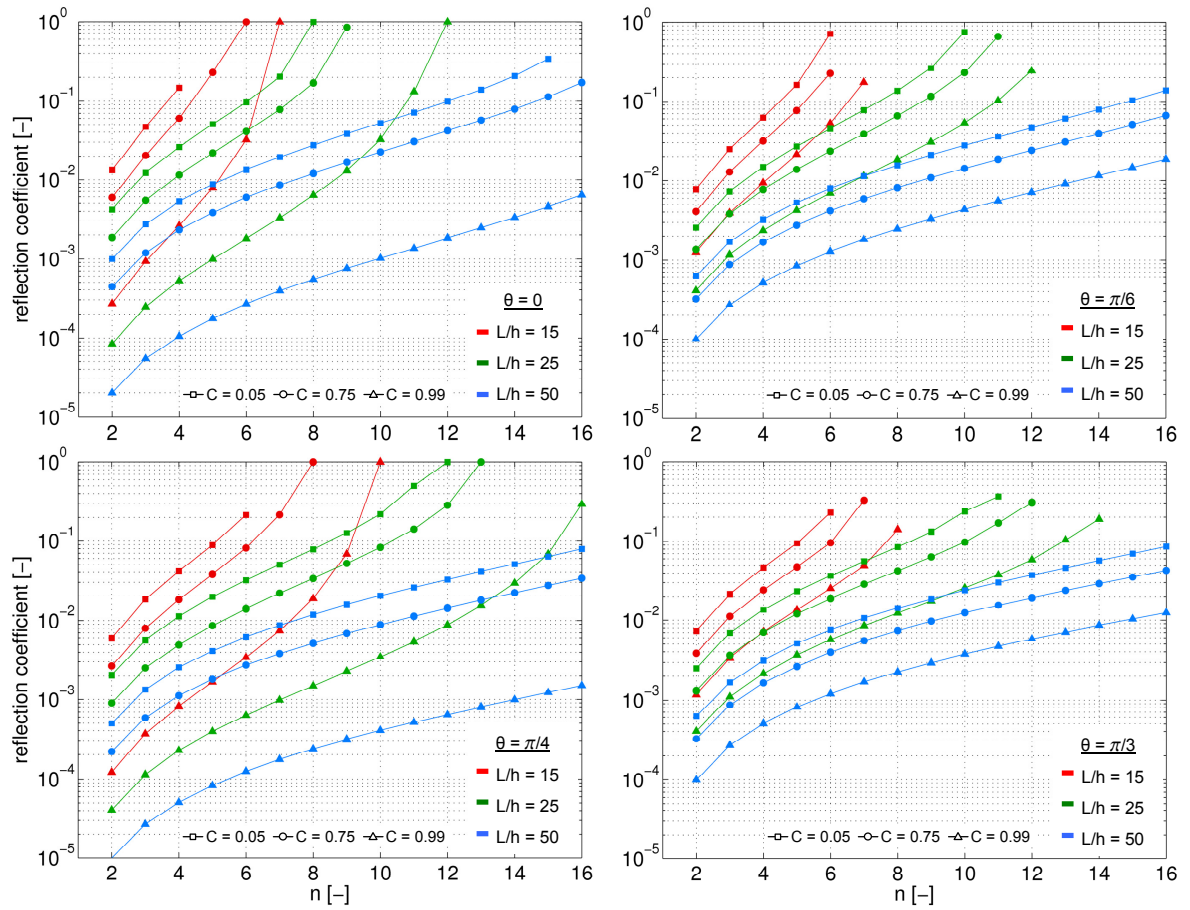


Figure 5.13: Magnitude of the reflected wave amplitude  $|A_R^+|$ , or reflection coefficient, vs. the ratio  $n$  of coarse to fine grid size for three number of points per wavelength,  $L/h = L/\Delta x = 2\pi/\Delta x/k^-$ , and Courant numbers  $C = 0.05$  (squares),  $0.75$  (circles) and  $0.99$  (triangles).

### 5.3.3 Replica Reinterpretation

As in the one-dimensional case, a replica reinterpretation of the finite-difference scheme (5.23-5.27) can be obtained simply by noting it *decouples* into independent central-difference schemes for  $n$  replicas  $\{(\alpha, \beta, jn+k), \alpha \geq 0, j \in \mathbb{Z}, k = 0, \dots, n-1\}$  of a space-time grid of size  $(n\Delta x, n\Delta y, n\Delta t)$ . The  $k$ th replica in the ensemble may be regarded as a *copy* of a space-time grid of size  $(n\Delta x, n\Delta y, n\Delta t)$  shifted in time by  $k\Delta t$ ,  $k = 0, \dots, n-1$ . A general wave exiting the fine grid is distributed over the replicas according to phase, and this distribution may be regarded as a specific realization, or sample, of a *statistical ensemble*. Conversely, a general collection of waves exiting the replica ensemble is synthesized into a general wave in the fine grid. Thus, in multiple dimensions RTIs solve the transmissibility problem between regions of different spatial resolution by setting up replica ensembles on the coarse regions of the grid and by the two-way conversion between short-wavelength phonons and statistical samples.

---

**Algorithm 2:** Replica implementation of the multi-dimensional transmitting scheme.

---

- 1: For given  $i, \beta \in n\mathbb{Z}$ , set  $j = \lfloor i/n \rfloor$ ,  $k = (i \bmod n)$ ,  $u_{0,\beta}^i = u_{0,\beta}^{k,j}$  and  $u_{-1,\beta}^i = u_{-n,\beta}^i$
  - 2: For  $\alpha < -1, \beta \in \mathbb{Z}$ :  

$$u_{\alpha,\beta}^{i+1} = 2u_{\alpha,\beta}^i - u_{\alpha,\beta}^{i-1} + \frac{c^2\Delta t^2}{\Delta x^2}(u_{\alpha+1,\beta}^i - 2u_{\alpha,\beta}^i + u_{\alpha-1,\beta}^i) + \frac{c^2\Delta t^2}{\Delta y^2}(u_{\alpha,\beta+1}^i - 2u_{\alpha,\beta}^i + u_{\alpha,\beta-1}^i)$$
  - 3: For  $\alpha = -1, \beta \in n\mathbb{Z}$ :  

$$u_{-1,\beta}^{i+1} = 2u_{-1,\beta}^i - u_{-1,\beta}^{i-1} + \frac{c^2\Delta t^2}{\Delta x^2}(u_{0,\beta}^i - 2u_{-1,\beta}^i + u_{-2,\beta}^i) + \frac{c^2\Delta t^2}{\Delta y^2}(u_{-1,\beta+1}^i - 2u_{-1,\beta}^i + u_{-1,\beta-1}^i)$$
  - 4: For  $\alpha = -1, \beta \in n\mathbb{Z}, l = 1, \dots, n-1$ :  
    - a)  $\tilde{u}_{0,\beta+l}^i \equiv \frac{l}{n}u_{0,\beta+n}^i + \frac{n-l}{n}u_{0,\beta}^i$
    - b)  $2\tilde{u}_{-1,\beta+l}^i \equiv \frac{l}{n}u_{-1,\beta+n}^i + \frac{n-l}{n}u_{-1,\beta}^i + u_{-1,\beta+l}^i$
    - c)  

$$u_{-1,\beta+l}^{i+1} = 2u_{-1,\beta+l}^i - u_{-1,\beta+l}^{i-1} + \frac{c^2\Delta t^2}{\Delta x^2}(\tilde{u}_{0,\beta+l}^i - 2\tilde{u}_{-1,\beta+l}^i + u_{-2,\beta+l}^i) + \frac{c^2\Delta t^2}{\Delta y^2} \frac{4}{l(n-l)}(\tilde{u}_{-1,\beta+l}^i - u_{-1,\beta+l}^i)$$
  - 5: For  $\alpha = 0, \beta \in n\mathbb{Z}$ ,  

$$u_{0,\beta}^{k,j+1} = 2u_{0,\beta}^{k,j} - u_{0,\beta}^{k,j-1} + \frac{c^2\Delta t^2}{\Delta x^2}(u_{1,\beta}^{k,j} - 2u_{0,\beta}^{k,j} + u_{-1,\beta}^{k,j}) + \frac{c^2\Delta t^2}{\Delta y^2}(u_{0,\beta+n}^{k,j} - 2u_{0,\beta}^{k,j} + u_{0,\beta-n}^{k,j})$$
  - 6: For  $\alpha > 0, \beta \in n\mathbb{Z}$ ,  

$$u_{\alpha,\beta}^{k,j+1} = 2u_{\alpha,\beta}^{k,j} - u_{\alpha,\beta}^{k,j-1} + \frac{c^2\Delta t^2}{\Delta x^2}(u_{\alpha+1,\beta}^{k,j} - 2u_{\alpha,\beta}^{k,j} + u_{\alpha-1,\beta}^{k,j}) + \frac{c^2\Delta t^2}{\Delta y^2}(u_{\alpha,\beta+n}^{k,j} - 2u_{\alpha,\beta}^{k,j} + u_{\alpha,\beta-n}^{k,j})$$
- 

A replica implementation of the multidimensional-dimensional transmitting finite-difference scheme (5.23 - 5.27) is shown in Algorithm 2 in two dimensions ( $d = 2$ ). In this implementation the outcome is composed of the solution  $\{u_{\alpha,\beta}^i, \alpha \geq 0, i, \beta \in \mathbb{Z}\}$  over the fine space-time grid and the transition layer, and the solutions  $\{u_{\alpha,\beta}^{k,j}, \alpha \geq -1, j\beta \in \mathbb{Z}, k = 0, \dots, n-1\}$  over each of the  $n$  replicas of the

coarse space-time grid. As in the one-dimensional case, the fine solution extends up to the interface and the replicas extend beyond the interface over a coarse spatial grid size  $n\Delta x$ . In particular, the replicas and the fine solution overlap over the region  $-n\Delta x \leq x \leq 0$ . Step (i) in Algorithm 2 *activates* the  $k^{\text{th}}$ -replica *in phase* with time  $i$ . For  $\alpha < -1$ , the solution over the fine grid proceeds as in the standard central difference scheme. At  $\alpha = -1$  the transition stencil applies with the value of  $u_{0,\beta}^i$ ,  $\beta \in n\mathbb{Z}$ , at the interface set by the replicas, i. e., set to  $u_{0,\beta}^{k,j}$ . The solution over each of the replicas also proceeds as in the standard central difference scheme with the value of  $u_{-n,\beta}^{k,j}$ ,  $\beta \in n\mathbb{Z}$ , set by the fine solution, i. e., set to  $u_{-n,\beta}^i$ .

### 5.3.4 Complexity of Multi-Dimensional RTIs

As in the one-dimensional case, we note that whereas the  $n$ -fold replication of the coarse grid that is the basis of RTIs increases the computational complexity of the schemes by a factor of  $n$  with respect to central differences on a single coarse grid, a net speed-up factor of  $n^d$  still remains with respect to central differences on the fine grid, where  $d$  is the spatial dimension. However, the processing of the replicas is trivially parallelizable, which may afford a speed-up of  $O(n)$  in execution time. Thus, the execution times for parallel RTIs may be expected to exhibit a speed-up factor of  $O(n^{d+1})$ , i. e., to be comparable to the execution times for sequential central differences on a single coarse space-time grid.

## 5.4 Finite-Element Reformulation

In this section we show how the RTI finite-difference schemes developed in the foregoing can be formally reformulated within a finite-element framework. In particular, this reformulation provides an avenue for extending these schemes to fully nonlinear problems. Whereas the extension is formal, the resulting finite-element RTI may be expected to inherit the convergence and transmission properties of the linear finite-differences RTIs. In subsequent sections, we establish that this is indeed so by means of numerical testing.

The finite-element reformulation of the RTI schemes is shown schematically in Fig. 5.14 for the

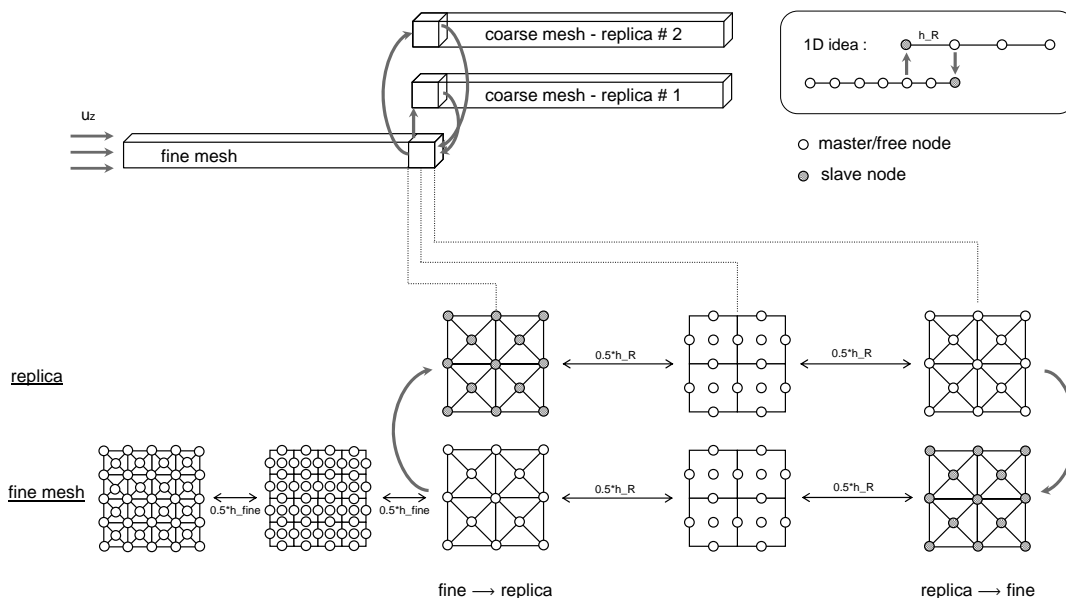


Figure 5.14: Schematics of the RTI implementation using finite elements.  $h_{fine}$  and  $h_R$  refer to the characteristic element size for fine and coarse meshes, respectively ( $n = 2$  for this particular case).

particular case of mesh-size doubling, i. e., for a coarsening ratio  $n = 2$ . The extension proceeds by analogy to the master-slave structure of finite-difference RTIs and their interpretation in terms of an transition region, cf. Fig. 5.6 and Section 5.2.3. We recall that, in this interpretation, the coarse region extends –and covers– by one grid spacing over the fine region, with the end point of the fine grid being constrained by the coarse grid and the end point of the coarse grid being constrained by the fine grid. Equivalently, we may regard Fig. 5.6 as a diagram describing the flow of information, according to which the fine grid *deposits* information in the interior of the coarse grid and the coarse grid *deposits* information in the interior of the fine grid, thus ensuring a two-way flow of information across the interface.

The finite-element implementation shown in Fig. 5.15 simply replicates this coupling and information-flow pattern. Both the fine and coarse meshes are structured according to a hexahedral geometry with additional nodes at the centers of the faces and at the centers of the cubes. This node set is triangulated using tetrahedral elements, Fig. 5.15. The transition region is structured simply through a doubling of the mesh size in the fine mesh, Fig. 5.15. The resulting plane-by-plane coupling avoids dangling or unpaired nodes which, inevitably, result in ringing and instabilities.

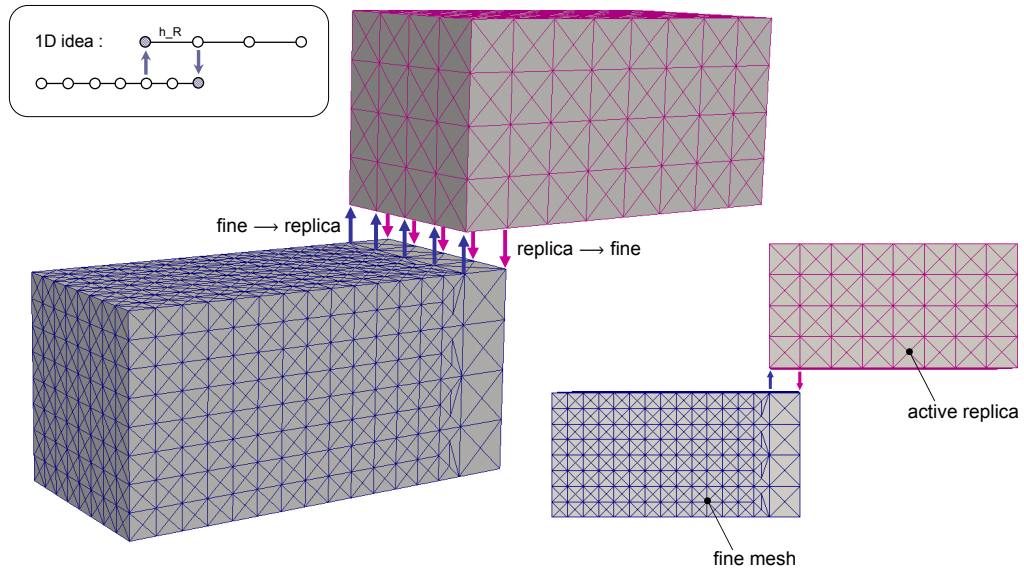


Figure 5.15: Finite element implementation of RTI ( $n = 2$  for this particular case).

## 5.5 Numerical Tests

We proceed to assess the properties of the finite-element RTIs by means of selected numerical tests. Of particular interest are the convergence and transmission properties of the scheme, especially in the nonlinear range.

### 5.5.1 Hookean Material

Our first example concerns the propagation of linear elastic waves through the thickness of an infinite plate. The material is assumed to be Hookean with Lamé constants:  $\lambda = 59.3 \times 10^9$  Pa and  $\mu = 26.5 \times 10^9$  Pa. The mass density is  $\rho = 2700$  kg/m<sup>3</sup>. Sliding boundary conditions are applied to the lateral surfaces of the domain in order to enforce uniaxial-strain conditions, Fig. 5.16. The plate is initially at rest. The right boundary is held fixed and the left boundary is given the following displacement boundary condition for  $t > 0$ ,

$$u_z(t) = u_z(t - \Delta t) + v_o \Delta t \quad (5.37)$$

where  $v_o = 1000$  m/s.

### 5.5.1.1 Normal Fine-Coarse Coupling

We begin by testing the ability of RTI to transmit waves *across* a mesh interface. Owing to the uniaxial-strain character of the problem, the analysis can be restricted to a through-thickness core of the plate of square cross-section. The resulting domain of analysis is split *transversely* into two regions of the same length, one meshed finely and the other coarsely, Fig. 5.16. The coarsening ratio is 2, i. e., the coarse mesh is twice as coarse as the fine mesh, and the fine-coarse overlap region extends over one coarse element, cf. Fig. 5.14, in analogy with the one-dimensional scheme. Table 5.1 collects the mesh sizes and time steps used in calculations. Fig. 5.16 also depicts the time evolution of the displacement field. As may be seen from these plots, the step wave crosses the mesh interface without notable internal reflections.

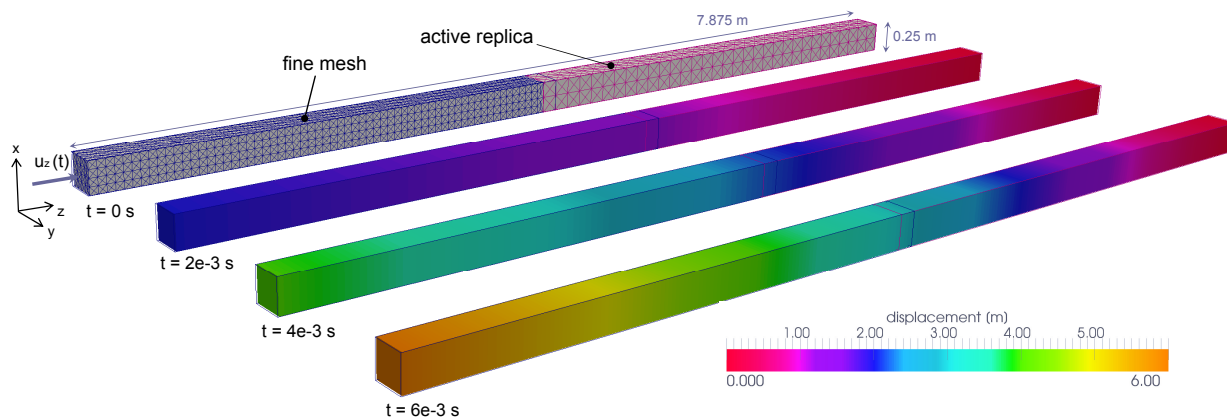


Figure 5.16: Linear elastic step wave propagating through the thickness of an infinite linear-elastic plate. On left, finite-element mesh with transverse mesh-size doubling interface. On right, contour plot of  $z$ -displacements as a function of time.

	UFS	RTI	
Element size [m]	0.0625	0.0625	0.1250
Time step [s]	$5 \times 10^{-7}$	$5 \times 10^{-7}$	$1 \times 10^{-6}$
Courant number [-]	0.05	0.05	0.05

Table 5.1: Step wave through linear-elastic plate, normal fine-coarse coupling. Summary of mesh sizes and time steps used in RTI and uniform-fine scheme (UFS) calculations.

Fig. 5.17a shows the trajectory of material points initially at several locations through the thickness of the plate and over several reverberations of the wave. We note that the step wave crosses the mesh interface at times  $t \approx 0.5, 1.8, 3.0, 4.3$  and  $5.5$  ms. Shown for comparison are the RTI solution

at centerline nodes and the corresponding solution obtained from a uniformly-fine scheme (UFS). Remarkably, the RTI and the UFS solutions remain indistinguishable at all times. In particular, the RTI wave crosses the mesh interface repeatedly and in both directions without any ostensible internal reflections. Fig. 5.17b shows the time evolution of the RTI and UFS total energies. The RTI energy is computed by adding the total energy of the fine mesh and the active replica outside the overlap region and averaging the fine and replica energies over the overlap region. Again we note that the RTI and the UFS solutions are indistinguishable. This agreement in turn shows that the RTI wave crosses the mesh interface *listlessly*, i. e., without appreciable loss or addition of energy.

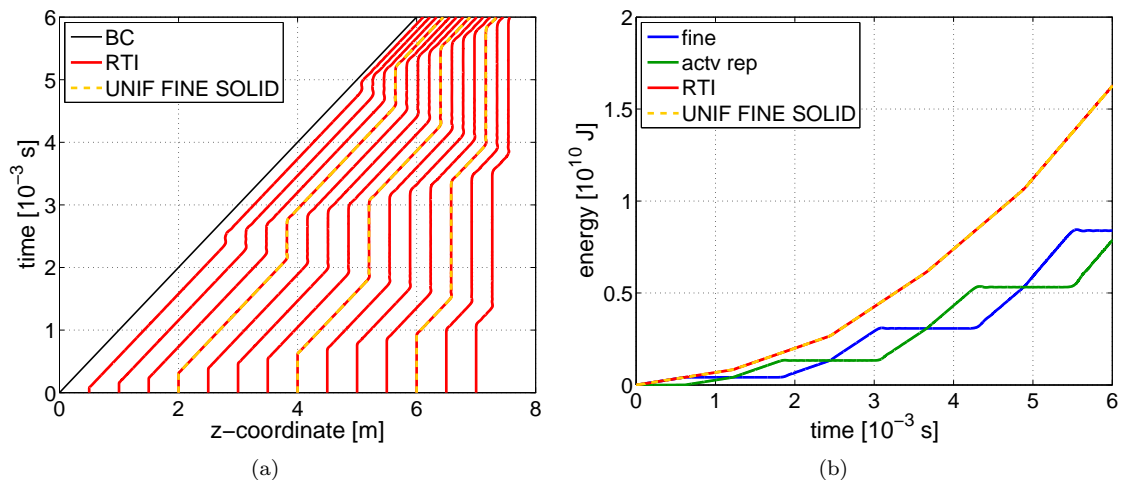


Figure 5.17: Step wave through linear-elastic plate, normal fine-coarse coupling. RTI and uniform-fine scheme (UFS) solutions. a) Material point trajectories through several reverberations of the wave. b) Corresponding time evolution of the total energy.

### 5.5.1.2 Tangential Fine-Coarse Coupling

Next we test the ability of RTI to transmit waves *along* a mesh interface. As before, owing to the uniaxial-strain character of the problem, the analysis can be restricted to a through-thickness core of the plate of rectangular cross section, with sliding boundary conditions prescribed on the lateral surfaces. The resulting domain of analysis is split *longitudinally* into two regions of identical square cross section, one meshed finely and the other coarsely, Fig. 5.18. The coarsening ratio is 2, i. e., the coarse mesh is twice as coarse as the fine mesh, and the fine-coarse overlap region extends over

one coarse element. The mesh sizes and time steps used in calculations are again as tabulated in Table 5.1. We note that this longitudinal mode of wave propagation is strictly multidimensional and cannot be tested in one dimension. We also emphasize that the same RTI scheme is used in both tests, the normal and tangential fine-coarse coupling. Thus the tests assess the ability of the same RTI scheme to transmit waves both across and along mesh interfaces.

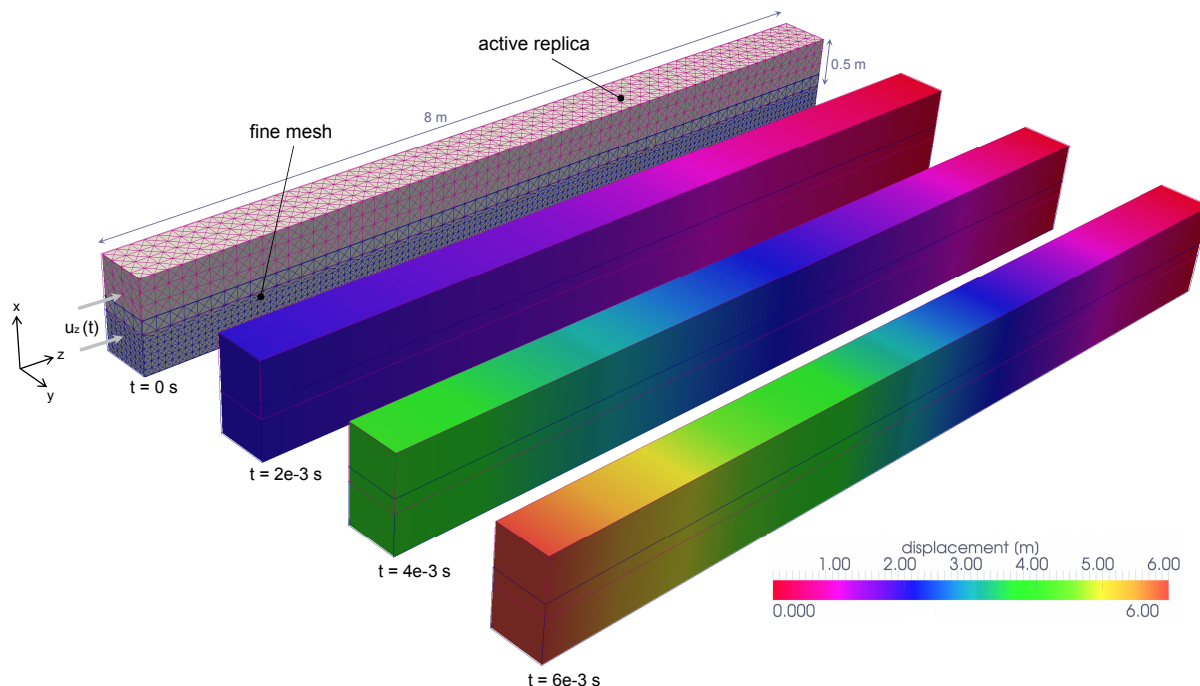


Figure 5.18: Linear elastic step wave propagating through the thickness of an infinite linear-elastic plate. On left, finite-element mesh with longitudinal mesh-size doubling interface. On right, contour plot of  $z$ -displacements as a function of time.

Fig. 5.19a shows the trajectory of material points initially at several locations through the thickness of the plate and over several reverberations of the wave. The step wave now follows the mesh interface as it propagates through the plate. Shown for comparison are the RTI solution at centerline nodes and the corresponding solution obtained from a uniformly-fine scheme (UFS). Remarkably, the RTI and the UFS solutions remain indistinguishable at all times, and ostensibly identical to those obtained in the normal incidence calculations described in the foregoing. Fig. 5.19b shows the time evolution of the RTI and UFS total energies. The RTI energy is again computed by adding the total energy of the fine mesh and the active replica outside the overlap region and averaging the fine

and replica energies over the overlap region. As in the case of normal incidence, the RTI and the UFS solutions are indistinguishable. In particular, the RTI wave follows the mesh interface *listlessly* without appreciable loss or addition of energy.

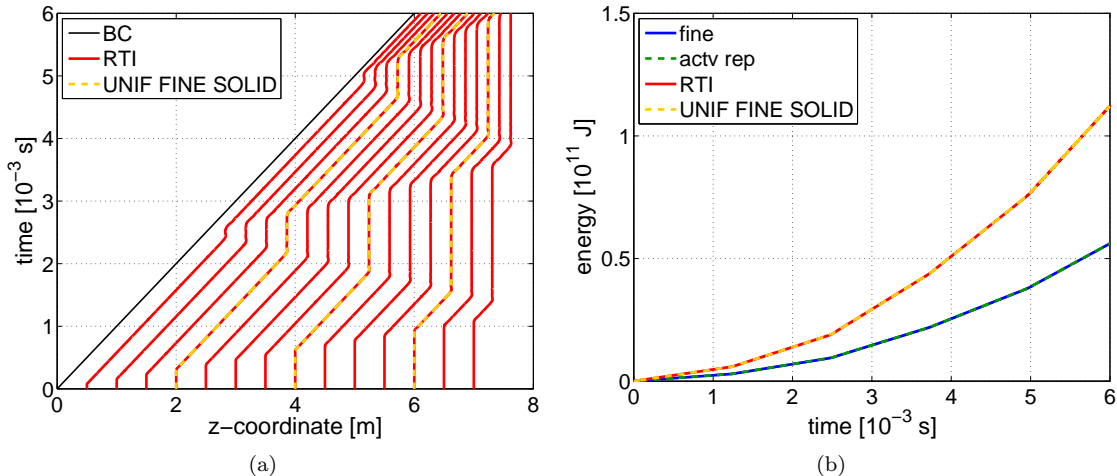


Figure 5.19: Step wave through linear-elastic plate, longitudinal fine-coarse coupling. RTI and uniform-fine scheme (UFS) solutions. a) Material point trajectories through several reverberations of the wave. b) Corresponding time evolution of the total energy.

## 5.5.2 Neo-Hookean Material

As an illustration of the performance of RTIs in the fully nonlinear range, we repeat the test cases described in the foregoing for a finitely-deforming compressible neo-Hookean material, again with Lamé constants  $\lambda = 59.3 \times 10^9$  Pa and  $\mu = 26.5 \times 10^9$  Pa and mass density  $\rho = 2700$  kg/m<sup>3</sup>. In the calculations, the impact velocity  $v_0$  at the left boundary is set to 700 m/s and the time steps are reduced five-fold with respect to those listed in Table 5.1. The initial and three subsequent configurations of the domain of analysis are shown in Figs. 5.20a and 5.20b for the transverse and longitudinal mesh interfaces, respectively. The large deformations undergone by the plate –and the attendant high degree of geometrical nonlinearity of the problems– are noteworthy from the figures.

For the case of a transverse mesh interface, Fig. 5.21a shows the trajectory of material points initially at several locations through the thickness of the plate and over several reverberations of the wave, and Fig. 5.21b shows the time evolution of the RTI and the uniformly-fine scheme (UFS) total

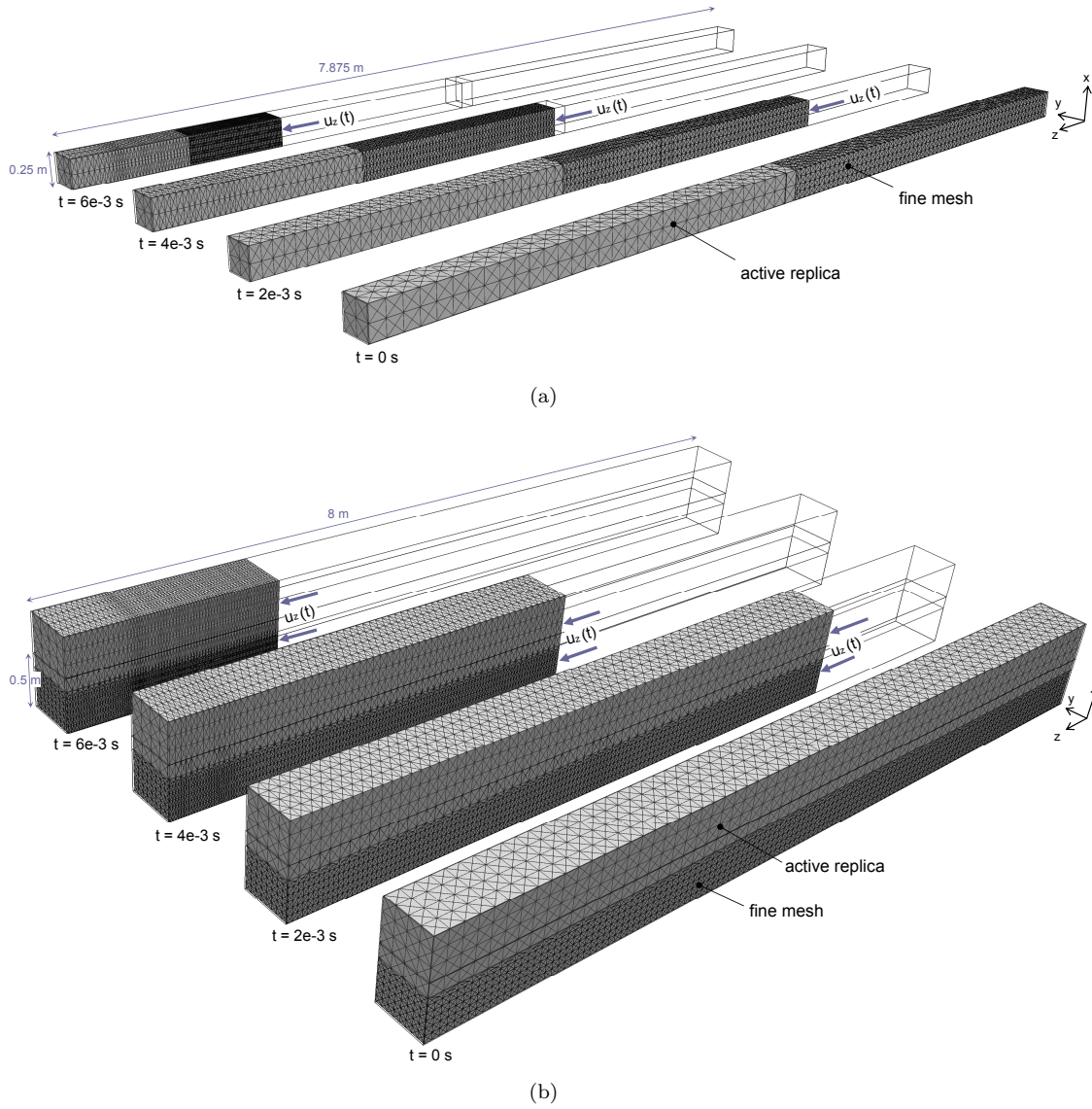


Figure 5.20: Nonlinear elastic step wave propagating through the thickness of an infinite compressible neo-Hookean elastic plate. Initial configuration and three subsequent deformed configurations. Displacements shown to scale. a) Transverse mesh interface. b) Longitudinal mesh interface.

energies. Figs. 5.22a and 5.22b show similar data for the case of a longitudinal mesh interface. As may be seen from the figures, the behavior of RTIs in the nonlinear range is altogether analogous to their behavior in the linear range. In particular, the step wave crosses or propagates along the interface without any ostensible internal reflections and without any appreciable loss or addition of energy.

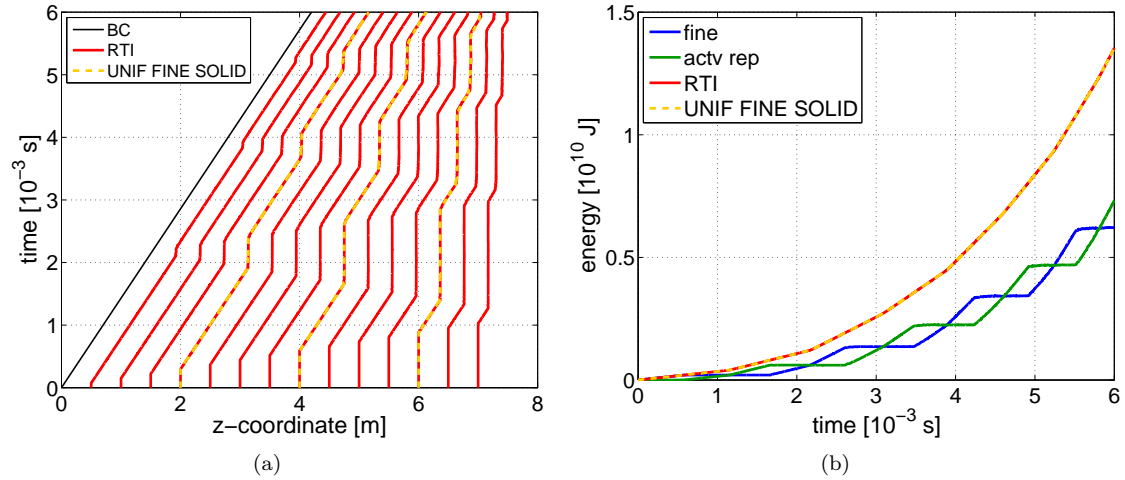


Figure 5.21: Step wave through compressible neo-Hookean elastic plate, normal fine-coarse coupling. RTI and uniform-fine scheme (UFS) solutions. a) Material point trajectories through several reverberations of the wave. b) Corresponding time evolution of the total energy.

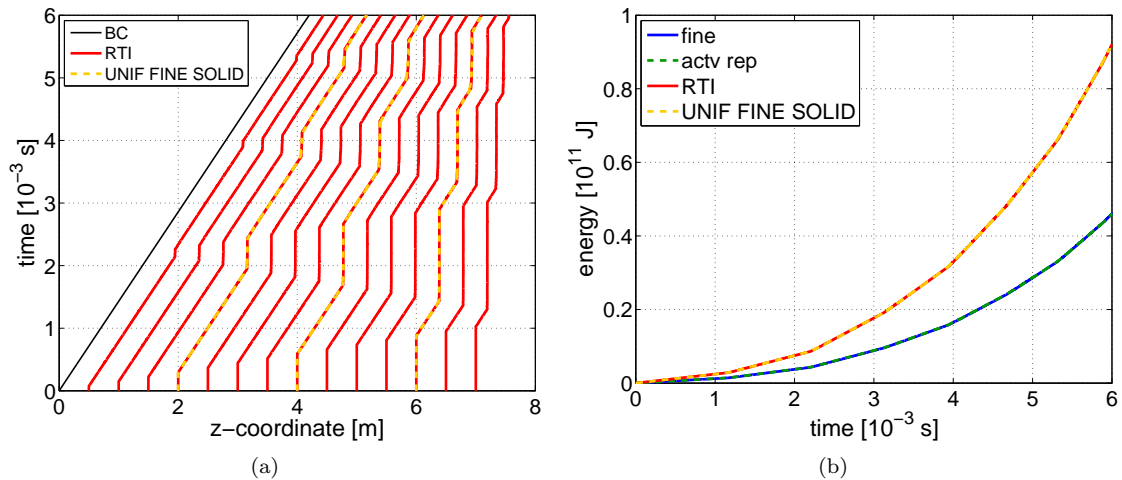


Figure 5.22: Step wave through compressible neo-Hookean elastic plate, longitudinal fine-coarse coupling. RTI and uniform-fine scheme (UFS) solutions. a) Material point trajectories through several reverberations of the wave. b) Corresponding time evolution of the total energy.

## 5.6 Discussion

In this chapter we have addressed the longstanding problem of wave propagation in discrete models of nonuniform spatial resolution and the formulation of time-integration schemes that are capable of listlessly transmitting waves across mesh interfaces. We have formulated a new class of *Replica Time Integrators* (RTIs) that allows for the two-way transmission of thermal phonons across mesh interfaces. This two-way transmission afforded by RTIs is accomplished by representing the state of the coarse regions by means of *replica ensembles*, consisting of collections of identical copies of the coarse regions, and, to the best of our knowledge, this does not appear to have been addressed or attempted in the past. By a combination of phase-error analysis and numerical testing we have shown that RTIs are convergent, result in exact two-way transmissibility at the Courant-Friedrichs-Lewy (CFL) limit for any angle of incidence, and allow step waves and thermal phonons to cross mesh interfaces in both directions listlessly, i. e., without appreciable loss or addition of energy, and without any ostensible internal reflections. In addition, the replica ensemble structure of RTIs render them ideally suited for parallel computing. In dimension  $d$  RTIs afford an  $O(n^d)$  speed-up factor in sequential mode, and  $O(n^{d+1})$  in parallel, over regions that are coarsened  $n$ -fold. In this manner, RTIs simultaneously provide an effective solution to the problem of wave transmission across mesh interfaces as well as supplying a new paradigm for parallel computing in wave propagation problems.

In the work presented in this chapter, RTIs have been couched as discretization schemes for continuum partial-differential equations. However, it is intriguing to digress on possible applications of the approach to problems that are discrete *ab initio*, such as molecular dynamics. A case in point concerns coarse-grained atomistic models, which often contain regions of vastly disparate spatial and temporal resolutions, ranging from atomistic to continuum (e. g., [8, 113–117]). For instance, an efficient discretization for the simulation of dynamic nanoindentation of ductile metals may consist of a fully-atomistic model in the zone immediately under the indenter, where dislocations are punched in, and an increasingly coarse discretization away from the indenter (e. g., [9, 118–120]). Similar schemes suggest themselves –and have been widely used– for the simulation of localized defects in crystals. In the dynamic range, the naïve application of standard time-integration schemes, such

as velocity-Verlet, to such models leads to *phonon trapping* in the atomistic regions. Such phonon trapping in turn results in spuriously high temperatures which may corrupt the simulation and severely detract from its accuracy (e. g., [100, 121]).

In this context, RTIs would appear to have the potential for providing a seamless bridge between *molecular dynamics* in the fully-resolved atomistic regions of the model and *irreversible continuum thermodynamics* in the coarse-grained regions. By irreversible continuum thermodynamics we specifically mean a statistical description of the coarse-grained molecular ensemble that includes macroscopic dynamics and transport phenomena such as heat conduction. By a seamless transition we mean: that a single approximation scheme –as opposed to a heterogenous patchwork of schemes– can be made to behave as closely to either molecular dynamics or irreversible continuum thermodynamics as desired solely by the choice of temporal and spatial resolution; and that all the relevant physics is modeled at the fundamental or atomistic level, without the addition of empirical parameters or assumptions. For RTIs, the representational device enabling this seamless two-way transition is the replica-ensemble description of the coarse regions of the system. A first illustration of how RTIs can potentially bridge molecular dynamics and statistical thermodynamics is provided by the last example of Section 5.2.5, which concerns the transmission of thermal phonons into a 100-fold coarser region, represented using 100 replicas. Given the size of the replica ensemble, every grid point on the coarse grid may be regarded as carrying a statistical distribution of positions and velocities. The mean values of the distribution may then be regarded as defining the *macroscopic motion*, while the corresponding fluctuations about the mean may be regarded as *heat*. However, we note that no assumption of ergodicity, equilibrium or thermodynamic limit is made at any point in the calculations. In particular, the distribution of heat may be transient and spatially inhomogeneous, in which case the transport of heat is accounted for in the calculations. Because no thermodynamic limit is invoked at any time in the formulation, RTIs apply just as well to small and large ensembles, thus providing the desired seamless transition between molecular dynamics and statistical thermodynamics. This potential of RTIs, beyond their role as numerical discretization schemes investigated in this chapter, suggests itself as a fruitful subject for further investigation.



## Chapter 6

# Concluding Remarks and Future Work

The goal of the work presented in this dissertation was to develop methods of multiscale analysis that take atomistic descriptions as their sole input but enable the simulation of slow macroscopic processes. The way in which these goals were met, as well as the avenues for future work, may be summarized as follows.

### Chapter 2

The issue of accounting for finite temperature in coarse grained systems has not been solved entirely. For finite temperature systems at equilibrium, constructing an effective free energy in terms of a reduced set of atomic degrees of freedom is still an open area of research. For dynamic systems driven out-of-equilibrium, the unphysical reflection of waves due to mesh inhomogeneities results in an energy build-up of the atomically refined region, which amounts to a localized, non-physical heating of the crystal.

The objective of this chapter was aligned with the study of non-equilibrium, thermally-activated processes such as heat transfer. To this end, we introduced a framework to simulate (spatially) coarse dynamic systems in the canonical ensemble using the Quasicontinuum method (QC). The equations of motion were strictly derived from dissipative Lagrangian mechanics. This derivation naturally provided a classical Langevin implementation where the timescale is governed by vibrations emanating from the finest length scale in the computational cell.

In order to assess the framework's ability to transmit information across scales, we studied the

phonon impoverish spectra in coarse regions and the resulting underestimation of thermal equilibrium properties. We examined the entropy loss using the thermal expansion coefficients of aluminum and tantalum as metric. For Al (in the atomistic limit) our method recovers the atomistic  $\alpha$ —as given by the interatomic potential employed— and produces coarse thermal expansion coefficients that obey a linear relation with the number of nodes  $N_h$  used to characterize the sample. For Ta, the anomalies of the interatomic potential employed result in negative and zero thermal expansion at low and high temperatures, respectively.

The method reduces to full Molecular Dynamics in the atomistic limit and a system of strongly-coupled oscillators in the coarse limit. Its has two main limitations:

- i. Langevin-QC contains no particular mechanism for suppressing wave reflections at mesh boundaries. The unphysically accumulated heat is dealt with by overdamping to maintain stable dynamics. Therefore, it only allows for the propagation of waves supported by the less compliant of the two meshes across a heterogeneous boundary. In other words, phonons that cannot be represented in the coarser portions of the mesh are filtered out, solving the heat reflection and unwanted energy built-up in the atomistic region. However, given the entropic loss stemming from mesh coarsening, it is not clear how this numerical scheme would perform in transferring heat into the atomistic region.
- ii. The attainable time steps are bounded by the fastest nodal vibration, which for atomistic systems is usually of the order of  $fs$ . Methods to increase the time step in unstructured triangulations have been proposed. For example, Kane et al. [122] and Lew et al. [123] have developed a class of Asynchronous Variational Integrators (AVI) for non-linear dynamics that permit the selection of independent time steps in each element. Coupling AVI to our dynamic QC framework could significantly enhance the extent of time scales probed during simulations. Another alternative would be to use the Replica Time Integrators (developed in Chapter 5) to integrate the equations of motion.

### Chapter 3

Atomistic computer simulations have been employed for the past thirty years to determine structural and thermodynamic (equilibrium) properties of solids and their defects over a wide range of temperature and pressure. The traditional Monte Carlo (MC) and Molecular Dynamics (MD) methods, while ideally suited to these calculations, require appreciable computational resources in order to calculate the long-time averages from which properties are obtained [59, 60].

In order to overcome this disadvantage and thereby permit a reasonably quick, but accurate determination of the equilibrium properties of interest, we obtained effective thermodynamic potentials while avoiding the treatment of all the system's atomic degrees of freedom. By restricting ourselves to the study of multi-species crystalline materials at finite temperature, the idea was to account for the energy contained in thermal oscillations and for the contribution of different components without knowledge of the instantaneous velocity of such vibrations or the specific identity of each atom within the lattice.

To assert the validity of the model, its ability to reproduce experimental measurements was tested. We found that the model predicts (experimental) alloy properties with reasonable accuracy. In addition, since it treats effective rather than instantaneous atomic degrees of freedom, it does so more efficiently than traditional Molecular Dynamics or Monte Carlo methods [59, 60].

The main limitations of this approach are:

- i. We assume no correlation among the atomic identity of different sites, which results in our configurational entropy being that of an ideal (i. e., non-interacting) mixture,  $S_c = -k_b \sum_i x_{A,i} \ln x_{A,i} + (1 - x_{A,i}) \ln(1 - x_{A,i})$ , see eq. (3.23). This is an upper bound because atomic interactions introduce correlations that reduce the configurational entropy.
- ii. The *hybrid* treatment of lattice sites within our mean field approach breaks down when there is extensive relaxation around solute atoms (due to a large size misfit for example) especially in the limit of small concentrations. To illustrate this point consider the evolution of equilibrium vacancy concentration in Cu as a function of temperature. Vacancies constitute the simplest point defects and play an important role in various material properties. Its equilibrium con-

centration results from the competition between the energy cost related to bond breakage and the entropy increase related to a larger number of microscopic configurations available to the system. The numerical results presented in Fig. 6.1 were obtained by finding the vacancy concentration  $x_A$  that minimizes the free energy  $F$  in a system containing a fixed number of host atoms  $(1 - x_A)N$ :

$$\min_{\bar{\mathbf{q}}} \min_{x_A} \min_{\{\omega\}} \frac{F(\bar{\mathbf{q}}, x_A, T, \{\omega\})}{(1 - x_A)N} \quad (6.1)$$

As Fig. 6.1 depicts, the model is able to predict the temperature at which the vacancy concentration becomes non-zero, but is unable to follow the evolution of this concentration with temperature. The method's inability to account for vacancies stems from the improper relaxation around vacant sites, which affects significantly the vacancy formation energy. Indeed, from the slope of a log plot of concentration versus inverse temperature, the vacancy formation energy is  $E_f = 1.584$  eV, roughly 25 percent higher than the experimental value. Thus, the mean field treatment neglects the relaxation energy around vacancies by treating all lattice sites equivalently.

Directions for future work include modeling of interstitial impurities, which could be useful in the study of Hydrogen embrittlement or swelling of structural materials subjected to radiation damage.

## Chapter 4

Based upon the effective potentials derived in Chapter 3, we presented a numerical framework capable of following the time evolution of crystalline systems over time windows currently beyond the scope of traditional atomistic methods such as Molecular Dynamics (MD) or Monte Carlo (MC). This was accomplished while retaining the underlying atomistic description of the material.

We formulated a discrete variational setting in which the simulation of time-dependent phenomena was reduced to a sequence of incremental problems, each characterized by a variational principle. In this fashion we were able to study the interplay between deformation and diffusion using time steps or strain rates that are orders of magnitude larger or smaller than their MD|MC counterparts. This variational structure determined the coupling between mechanics and diffusion in a unique way,

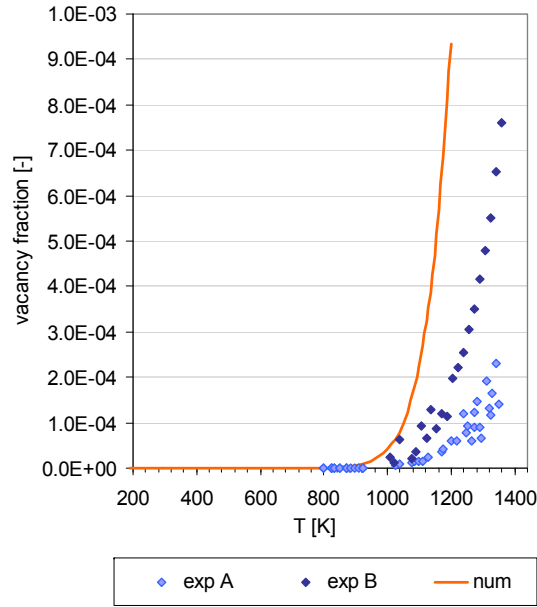


Figure 6.1: Numerical and experimental results (A: [124], B: [125]) of equilibrium vacancy concentration in copper as a function of temperature.

without additional coupling constitutive equations to relate the chemical potential of the impurity with its concentration or the state of stress of the system.

One of the salient features of this method is that it is discrete from the onset. Therefore, instead of discretizing the governing equations describing the behavior of continuum media, we modeled crystalline lattices as inherently discrete objects.

Future areas of application include:

- i. The role of grain boundary structure and orientation on impurity segregation in materials subjected to stress.
- ii. Analysis of phase segregation patterning in binary thin films under applied mechanical fields [126, 127].
- iii. Study of diffusion-induced bending in thin film adhesion [128, 129].

## Chapter 5

We addressed the longstanding problem of wave propagation in discrete models of nonuniform spatial resolution by formulating time-integration schemes capable of transmitting waves across mesh interfaces. To this end, we formulated a new class of *Replica Time Integrators* (RTIs) that allows for the two-way transmission of thermal phonons across mesh interfaces. This two-way transmission was accomplished by representing the state of the coarse region by a collection of identical copies or *replicas* of itself. Each replica runs at its own slow time step and is out-of-phase with respect to the others by one fast time step<sup>1</sup>. Then, each replica is capable of absorbing from the fine region the elementary signal that is in phase with the replica. Conversely, each replica is capable of supporting –and transmitting to the fine region– an elementary signal of a certain phase.

Using a combination of phase-error analysis and numerical testing we found that RTIs are convergent, and allow step waves and thermal phonons to cross mesh interfaces in *both* directions listlessly. In addition, the replica ensemble structure of RTIs render them ideally suited for parallel computing. In dimension  $d$  RTIs afford an  $O(n^d)$  speed-up factor in sequential mode, and  $O(n^{d+1})$  in parallel, over regions that are coarsened  $n$ -fold.

Even though RTIs were presented as discretization schemes for continuum partial-differential equations in this work, they appear to have the potential for providing a seamless bridge between *Molecular Dynamics* in fully-resolved atomistic regions and *irreversible Continuum Thermodynamics* in coarse-grained regions. By irreversible continuum thermodynamics we specifically mean a statistical description of coarse-grained regions that includes macroscopic dynamics and transport phenomena such as heat conduction. By a seamless transition we mean that a single approximation scheme can be made to behave closely to either molecular dynamics or irreversible continuum thermodynamics solely by the choice of temporal and spatial resolution; and that all the relevant physics is modeled at the atomistic level. This potential of RTIs, beyond their role as numerical discretization schemes investigated in this thesis, suggests itself as a fruitful subject for further investigation.

---

<sup>1</sup>Since fine and coarse regions evolve asynchronously in time, RTIs allow both spatial and temporal coarse graining of the system

# Bibliography

- [1] S. Gill. *Nonequilibrium Molecular Dynamics and Multiscale Modeling of Heat Conduction in Solids (Trends in Computational Nanomechanics, v. 9)*. Springer, 2010.
- [2] E. Marquis, J. Hyde, D. Saxey, S. Lozano-Perez, V. de Castro, D. Hudson, C. Williams, S. Humphry-Baker & G. Smith. Nuclear Reactor Materials at the Atomic Scale, *Materials Today*, **12**(11):30-37, 2009.
- [3] A. Voter, F. Montalenti & T. Germann. Extending the Time Scale in Atomistic Simulation of Materials, *Annual Review of Materials Research*, **32**:321-346, 2002.
- [4] Y. Kulkarni. *Coarse-Graining of Atomistic Description at Finite Temperature*. Ph.D. Thesis, California Institute of Technology, 2007.
- [5] Q. Yang, L. Stainier & M. Ortiz. A Variational Formulation of the Coupled Thermo-Mechanical Boundary-Value Problem for General Dissipative Solids, *Journal of the Mechanics and Physics of Solids*, **54**(2):401-424, 2006.
- [6] D. Rodney. Mixed Atomistic/Continuum Methods: Static and Dynamic Quasicontinuum Methods, *NATO Science Series II: Mathematics, Physics and Chemistry*, **108**:265-274, 2003.
- [7] S. Qu, V. Shastry, W. Curtin & R. Miller. A Finite-Temperature Dynamic Coupled Atomistic/Discrete Dislocation Method, *Modelling and Simulation in Materials Science and Engineering*, **13**(7):1101-1118, 2005.
- [8] E. Tadmor, M. Ortiz & R. Phillips. Quasicontinuum Analysis of Defects in Solids, *Philosophical Magazine A*, **73**(6):1529-1563, 1996.

- [9] J. Knap & M. Ortiz. An Analysis of the Quasicontinuum Method, *Journal of the Mechanics and Physics of Solids*, **49**(9):1899-1923, 2001.
- [10] R. Rudd & J. Broughton. Coarse-Grained Molecular Dynamics: Nonlinear Finite Elements and Finite Temperature, *Physical Review B*, **72**(14):144104, 2005.
- [11] W. Cai, M. de Koning, V. Bulatov & S. Yip. Minimizing Boundary Reflections in Coupled-Domain Simulations, *Physical Review Letters*, **85**(15):3213-3216, 2000.
- [12] R. LeSar, R. Najafabadi & D. Srolovitz. Finite-Temperature Defect Properties from Free-Energy Minimization, *Physical Review Letters*, **63**(6):624-627, 1989.
- [13] J. Althoff, D. Morgan, D. De Fontaine, M. Asta, S. Foiles & D. Johnson. Embedded Atom Method Calculations of Vibrational Thermodynamic Properties of Ordered and Disordered Ni<sub>3</sub>Al, *Computational Materials Science*, **10**(1-4):411-415, 1998.
- [14] Z. Tang, H. Zhao, G. Li & N. Aluru. Finite-Temperature Quasicontinuum Method for Multiscale Analysis of Silicon Nanostructures, *Physical Review B*, **74**(6):064110, 2006.
- [15] A. Baranyai & D. Evans. Comments on Thermodynamics Integration Methods for the Determination of Nonequilibrium Entropy, *Molecular Physics*, **74**(2):353-365, 1991.
- [16] M. Ortiz, A. Cuitiño, J. Knap & M. Koslowski. Mixed Atomistic-Continuum Models of Material Behavior: The Art of Transcending Atomistic and Informing Continua, *Material Research Society Bulletin*, **26**:1-6, 2001.
- [17] W. Curtin & R. Miller. Atomistic/Continuum Coupling in Computational Materials Science, *Modelling and Simulation in Materials Science and Engineering*, **11**(3):R33-R68, 2003.
- [18] F. Medina & F. Rosales. Spurious Reflections and Accuracy of Finite Element Models for Unbounded Wave Propagation Problems: the One-Dimensional Case, *Engineering Computations*, **4**(2):139-148, 1987.

- [19] B. Cathers, S. Bates & B. O'Connor. Coarse-Grained Molecular Dynamics: Nonlinear Finite Elements and Finite Temperature, *International Journal for Numerical Methods in Fluids*, **9**(7):783-810, 1989.
- [20] L. Jiang & R. Rogers. Spurious Wave Reflections at an Interface of Different Physical Properties in Finite-Element Wave Solutions, *Communications in Applied Numerical Methods*, **7**(8):595-602, 1991.
- [21] J. Von Neumann & R. Richtmyer. A Method for the Numerical Calculation of Hydrodynamic Shocks, *Journal of Applied Physics*, **21**(3):232-243, 1950.
- [22] W. E & H. Zhongyi. Matching Conditions in Atomistic-Continuum Modeling of Materials, *Physical Review Letters*, **87**(13):135501, 2001.
- [23] H. Park, E. Karpov, W. Liu & P. Klein. The Bridging Scale for Two-Dimensional Atomistic/Continuum Coupling, *Philosophical Magazine*, **85**(1):79-113, 2005.
- [24] S. Curtarolo & G. Ceder. Dynamics of an Inhomogeneously Coarse Grained Multiscale System, *Physical Review Letters*, **88**(25):255504, 2002.
- [25] G. Wagner, R. Jones, J. Templeton & M. Parks. An Atomistic-to-Continuum Coupling Method for Heat Transfer in Solids, *Computer Methods in Applied Mechanics and Engineering*, **197**(41-42):3351-3365, 2008.
- [26] V. Shenoy, V. Shenoy & R. Phillips. Finite Temperature Quasicontinuum Methods, *Materials Research Society Symposium Proceedings*, **538**:465-471, 1999.
- [27] Z. Wu, D. Diestler, R. Feng & X. Zeng. Coarse-Graining Description of Solid Systems at Nonzero Temperature, *Journal of Chemical Physics*, **119**(15):8013-8023, 2003.
- [28] L. Dupuy, E. Tadmor, R. Miller & R. Phillips. Finite-Temperature Quasicontinuum: Molecular Dynamics Without all the Atoms, *Physical Review Letters*, **95**(6):060202, 2005.

- [29] Y. Kulkarni, J. Knap & M. Ortiz. A Variational Approach to Coarse Graining of Equilibrium and Non-Equilibrium Atomistic Description at Finite Temperature, *Journal of the Mechanics and Physics of Solids*, **56**(4):1417-1449, 2008.
- [30] J. Knap & M. Ortiz. Effect of Indenter-Radius Size on Au(001) Nanoindentation, *Physical Review Letters*, **90**(22):226102, 2003.
- [31] J. Marian, J. Knap & M. Ortiz. Nanovoid Cavitation by Dislocation Emission in Aluminum, *Physical Review Letters*, **93**:165503, 2004.
- [32] J. Marian, J. Knap & G. Campbell. A Quasicontinuum Study of Nanovoid Collapse under Uniaxial Loading in Ta, *Acta Materialia*, **56**(10):2389-2399, 2008.
- [33] J. Marian & J. Knap. Breakdown of Self-Similar Hardening Behavior in Au Nanopillar Microplasticity, *International Journal for Multiscale Computational Engineering*, **5**(3-4):287-294, 2007.
- [34] B. Vujanovic & S. Jones. *Variational Methods in Nonconservative Phenomena (Mathematics in Science and Engineering, v. 182)*. Academic Press, 1989.
- [35] C. Gardiner. *Handbook of Stochastic Methods*. Springer, 2003.
- [36] R. Biswas & D. Hamann. Simulated Annealing of Silicon Atom Clusters in Langevin Molecular-Dynamics, *Physical Review B*, **34**(2):895-901, 1986.
- [37] G. Box & M. Muller. A Note on the Generation of Random Normal Deviates, *The Annals of Mathematical Statistics*, **29**(2):610-611, 1958.
- [38] J. Marian, G. Venturini, B. Hansen, J. Knap, M. Ortiz & G. Campbell. Finite-Temperature Extension of the Quasicontinuum Method Using Langevin Dynamics: Entropy Losses and Analysis of Errors, *Modelling and Simulation in Materials Science and Engineering*, **18**(1):015003, 2010.
- [39] A. Maradudin, E. Montroll & G. Weiss. *Theory of Lattice Dynamics in the Harmonic Approximation (Solid State Physics, Suppl. 3)*. Academic Press, 1963.

- [40] T. Hill. *Introduction to Statistical Thermodynamics*. Addison Wesley, 1962.
- [41] E. Wohlfarth (ed). *Thermophysical Properties of Materials (Selected Topics in Solid State Physics, vol. XVIII)*. North-Holland, 1986.
- [42] A. Authier (ed). *International Tables for Crystallography (vol. D: Physical Properties of Crystals)*. International Union of Crystallography, 2006.
- [43] G. Srivastava. *The Physics of Phonons*. Taylor & Francis, 1990.
- [44] Y. Touloukian, R. Kirby, R. Taylor & T. Lee. *Thermal Expansion of Non-metallic Solids (Thermophysical Properties Matter, vol. 13)*. Plenum Publishing Co., 1977.
- [45] C. Ho & R. Taylor. *Thermal Expansion of Solids*. ASM International, 1998.
- [46] M. Biegalski, J. Haeni, S. Trolier-McKinstry & D. Schlom. Thermal Expansion of the New Perovskite Substrates DySCO3 and GdSCO3, *Journal of Materials Research*, **20**(4):952-958, 2005.
- [47] F. Ercolessi & J. Adams. Interatomic Potentials from 1st-Principles Calculations - The Force-Matching Method, *Europhysics Letters*, **26**(8):583-588, 1994.
- [48] X. Liu, F. Ercolessi & J. Adams. Aluminium Interatomic Potential from Density Functional Theory Calculations with Improved Stacking Fault Energy, *Modelling and Simulations in Materials Science and Engineering*, **12**(4):665-670, 2004.
- [49] W. Pearson, *A Handbook of Lattice Spacings and Structures of Metals and Alloys*. Pergamon, 1958.
- [50] Y. Li, D. Siegel, J. Adams & X. Liu. Surface Phonon-Dispersion, Using Electron-Energy Loss Spectroscopy, *Physical Review B*, **67**(12):125101, 2003.
- [51] R. MacDonald & R. Shukla. Thermodynamic Properties of BCC Crystals at High-Temperatures - The Transition-Metals, *Physical Review B*, **32**(8):4961-4968, 1985.

- [52] Y. Mishin & A. Lozovoy. Angular-Dependent Interatomic Potential for Tantalum, *Acta Materialia*, **54**(19):5013-5026, 2006.
- [53] K. Ozaki, A. Fukutani & K. Honda. Effect of Interatomic Potential on Melting Point and Thermal Expansion of a Transition Metal, *JSME International Journal Series A - Solid Mechanics and Material Engineering*, **44**(2):199-206, 2001.
- [54] S. Foiles. Evaluation of Harmonic Methods for Calculating the Free-Energy of Defects in Solids, *Physical Review B*, **49**(21):14930-14938, 1994.
- [55] G. Ackland & V. Vitek. Many-Body Potentials and Atomic Scale Relaxations in Noble-Metal Alloys, *Physical Review B*, **41**(15):10324-10333, 1990.
- [56] R. Johnson. Alloy Models with the Embedded Atom Method, *Physical Review B*, **39**(17):12554-12559, 1989.
- [57] G. Bozzolo, R. Noebe & P. Abel (eds). *Applied Computational Material Modeling. Theory, Simulation and Experiments*. Springer, 2007.
- [58] J. Rose, J. Smith, F. Guinea & J. Ferrante. Universal Features of the Equation of State of Metals, *Physical Review B*, **29**(6):2963-2969, 1984.
- [59] A. Sutton, P. Mulheran & A. Stoneham. Direct Free Energy Minimization Methods: Application to Grain Boundaries, *Philosophical Transactions: Physical Sciences and Engineering*, **341**(1661):233-245, 1992.
- [60] H. Wang, R. Najafabadi & D. Srolovitz. (100) Surface Segregation in Cu-Ni Alloys, *Physical Review B*, **45**(20):12028-12042, 1992.
- [61] R. LeSar, R. Najafabadi & D. Srolovitz. Finite Temperature Defect properties from Free-Energy minimization, *Physical Review Letters*, **63**(6):624-627, 1989.
- [62] L. Zhao, R. Najafabadi & D. Srolovitz. Statistical Mechanical-Atomistic Determination of Vacancy Formation Free Energies in Cu-Ni Alloys, *Philosophical Magazine A*, **70**(3):519-529, 1994.

- [63] R. Najafabadi & D. Srolovitz. Evaluation of the Accuracy of the Free-Energy-Minimization Method, *Physical Review B*, **52**(13):9229-9241, 1995.
- [64] L. Girifalco. *Statistical Mechanics of Solids*. Oxford University Press, 2000.
- [65] H. Callen. *Thermodynamics and an Introduction to Thermostatistics*. John Wiley & Sons, 1985.
- [66] D. Zubarev. *Nonequilibrium Statistical Thermodynamics*. Consultants Bureau, 1974.
- [67] M. Allen & D. Tildesley. *Computer Simulation of Liquids*. Oxford University Press, 1989.
- [68] J. Weiner. *Statistical Mechanics of Elasticity*. Dover Publications, 2002.
- [69] S. Foiles, M. Baskes & M. Daw. Embedded Atom Method Functions for the FCC Metals Cu, Ag, Au, Ni, Pd, Pt and their Alloys, *Physical Review B*, **33**(12):7983-7991, 1986.
- [70] L. Bidwell. Unit-Cell Dimensions of Ni-Pd alloys at 25 and 900 C, *Acta Crystallographica*, **17**:1473-1474, 1964.
- [71] R. Toloukian. *Physical Properties of Matter, Thermal Expansion - Metallic Elements & Alloys - vol 12*. The TPRC Data Series, 1975.
- [72] R. Simmons & R. Balluffi. Measurement of Equilibrium Concentration of Vacancies in Copper, *Physical Review*, **129**(4):1533, 1963.
- [73] R. Phillips. *Crystals, Defects and Microstructures - Modeling Across Scales*. Cambridge University Press, 2001.
- [74] D. Wallace. *Thermodynamics of Crystals*. John Wiley & Sons, 1972.
- [75] M. Finnis. *Interatomic Forces in Condensed Matter*. Oxford Series on Material Modeling, 2003.
- [76] R. Johnson. Analytic Nearest Neighbor Model for fcc Metals, *Physical Review B*, **37**(8):3924-3931, 1988.
- [77] R. Najafabadi, H. Wang, D. Srolovitz & R. LeSar. A new Method for the Simulation of Alloys: Application to Interfacial Segregation, *Acta Metallurgica et Materialia*, **39**(12):3071-3082, 1991.

- [78] C. Helms & K. Yu. Determination of the Surface Composition of the Cu-Ni alloys for Clean and Adsorbate-Covered Surfaces, *Journal of Vacuum Science and Technology*, **12**(1):276-278, 1975.
- [79] T. Sakurai, T. Hashizume, A. Jimbo & A. Sakai. New Results in Surface Segregation of NiCu Binary Alloys, *Physical Review Letters*, **55**(5):514-517, 1985.
- [80] K. Wandelt & C. Brundle. Evidence for Crystal-Face Specificity in Surface Segregation of CuNi Alloys, *Physical Review Letters*, **46**(23):1529-1532, 1981.
- [81] T. King & R. Donnelly. Surface Compositions and Composition Profiles of AgAu (100), (110) and (111) Surfaces Determined Quantitatively by Auger Electron Spectroscopy, *Surface Science*, **151**:374-399, 1985.
- [82] G. Derry & R. Wan. Comparison of Surface Structure and Segregation in AgAu and NiPd Alloys, *Surface Science*, **566-568**:862-868, 2004.
- [83] A. Stroud. *Approximate Calculation of Multiple Integrals*. Prentice Hall, 1971.
- [84] M. Desbrun, A. Hirani, M. Leok & J. Marsden. Discrete Exterior Calculus, available from [arXiv.org/math.DG/0508341](https://arxiv.org/math.DG/0508341).
- [85] F. Larché. What Can the Concept of a Perfect Chemoelastic Solid Tell us about the Mechanical and Thermodynamic Behavior of a Solid?, *Journal de Physique IV*, **6**(C1):3-9, 1996.
- [86] M. Ariza & M. Ortiz. Discrete Crystal Elasticity and Discrete Dislocations in Crystals, *Archive for Rational Mechanics and Analysis*, **178**(2):149-226, 2005.
- [87] C. Flynn. *Point Defects and Diffusion*. Oxford University Press, 1972.
- [88] H. Helfmeier & M. Feller-Kniepmeier. Diffusion of Copper in Nickel Single Crystals, *Journal of Applied Physics*, **41**(8):3202-3205, 1970.
- [89] P. Shewmon. *Diffusion in Solids*. The Minerals, Metals and Material Society, 1989.

- [90] T. Lau, A. Kushima & S. Yip. Atomistic Simulation of Creep in a Nanocrystal, *Physical Review Letters*, **104**:175501, 2010.
- [91] M. Xu & T. Belytschko. Conservation Properties of the Bridging Domain Method for Coupled Molecular/Continuum Mechanics, *International Journal of Numerical Methods in Engineering*, **76**:278-298, 2008.
- [92] G. Parisi. *Field Theory, Disorder, Simulation (World Scientific Lecture Notes in Physics, vol. 45)*. World Scientific, 1992.
- [93] E. Karpov, G. Wagner & W. Liu. A Green's Function Approach to Deriving Non-Reflecting Boundary Conditions in Molecular Dynamics, *International Journal of Numerical Methods in Engineering*, **62**(9):1250-1262, 2005.
- [94] W. E & Z. Huang. Matching Conditions in Atomistic-Continuum Modeling of Materials, *Physical Review Letters*, **87**(13):135501, 2001.
- [95] X. Li & W. E. Variational Boundary Conditions for Molecular Dynamics Simulations of Solids at Low Temperature, *Communications in Computational Physics*, **1**:135-175, 2006.
- [96] B. Engquist & A. Majda. Absorbing Boundary Conditions for the Numerical Simulation of Waves, *Mathematics of Computation*, **31**:629-651, 1977.
- [97] B. Engquist & A. Majda. Radiation Boundary Conditions for Acoustic and Elastic Wave Calculations, *Communications On Pure & Applied Mathematics*, **32**(3):314-358, 1979.
- [98] S. Adelman & J. Doll. Generalized (Langevin) Equation Approach for Atom/Solid-Surface Scattering: Collinear Atom/Harmonic Chain Model, *Journal of Chemical Physics*, **61**:4242-4245, 1974.
- [99] S. Adelman & J. Doll. Generalized (Langevin) Equation Approach for Atom/Solid-Surface Scattering: General Formulation for Classical Scattering off Harmonic Solids, *Journal of Chemical Physics*, **64**:2375-2388, 1976.

- [100] T. Colonius & S. Lele. Computational Aeroacoustics: Progress on Nonlinear Problems of Sound Generation, *Progress in Aerospace Sciences*, **40**:345-416, 2004.
- [101] J. Berenger. A Perfectly Matched Layer for the Absorption of Electromagnetic Waves, *Journal of Computational Physics*, **114**:185-200, 1994.
- [102] J. Berenger. Three-Dimensional Perfectly Matched Layer for the Absorption of Electromagnetic Waves, *Journal of Computational Physics*, **127**:363-379, 1996.
- [103] A. To & S. Li. Perfectly Matched Multiscale Simulations, *Physical Review B*, **72**(3):035414, 2005.
- [104] D. Appelo & T. Colonius. A High-Order Super-Grid-Scale Absorbing Layer and its Application to Linear Hyperbolic Systems, *Journal of Computational Physics*, **228**(11):4200-4217, 2009.
- [105] D. Appelo & G. Kreiss. A New Absorbing Layer for Elastic Waves, *Journal of Computational Physics*, **215**:642-660, 2006.
- [106] D. Komatitsch & J. Tromp. A Perfectly Matched Layer Absorbing Boundary Condition for the Second-Order Seismic Wave Equation, *Geophysical Journal International*, **154**:146-153, 2003.
- [107] B. Holian & R. Ravelo. Fracture Simulations using Large-Scale Molecular Dynamics, *Physical Review B*, **51**(17):11275-11288, 1995.
- [108] S. Xiao & T. Belytschko. A Bridging Domain Method for Coupling Continua with MD, *Computer Methods in Applied Mechanics and Engineering*, **193**:1645-1669, 2004.
- [109] T. Belytschko & R. Mullen. *Formulations and Computational Algorithms in Finite Element Analysis (in Mesh Partitions of Explicit-Implicit Time Integrators)*. MIT Press, 1976.
- [110] T. Hughes. *The Finite Element Method : Linear Static and Dynamic Finite Element Analysis*. Prentice-Hall, 1987.
- [111] S. Muller & M. Ortiz. On the Gamma-Convergence of Discrete Dynamics and Variational Integrators, *Journal of Nonlinear Science*, **14**:279-296, 2004.

- [112] Z. Bazant & Z. Celep. Spurious Reflection of Elastic Waves in Nonuniform Meshes of Constant and Linear Strain Finite Elements, *Computer & Structures*, **15**(4):451-459, 1982.
- [113] R. Rudd & J. Broughton. Coarse-Grained Molecular Dynamics and the Atomic limit of Finite Elements, *Physical Review B*, **58**(10):5893-5896, 1998.
- [114] F. Abraham, J. Broughton, N. Bernstein & E. Kaxiras. Spanning the Continuum to Quantum Length Scales in a Dynamic Simulation of Brittle Fracture, *Europhysic Letters*, **44**:783-787, 1998.
- [115] G. Wagner & W. Liu. Coupling of Atomistic and Continuum Simulations using a Bridging Scale Decomposition, *Journal of Computational Physics*, **190**:249-274, 2003.
- [116] H. Park & W. Liu. An Introduction and Tutorial on Multiple-Scale Analysis in Solids, *Computer Methods in Applied Mechanics and Engineering*, **193**:1733-1772, 2004.
- [117] E. Karpov, G. Wagner & W. Liu. A Green's Function Approach to Deriving Non-Reflecting Boundary Conditions in Molecular Dynamics Simulations, *International Journal for Numerical Methods in Engineering*, **62**(9):1250-1262, 2005.
- [118] E. Tadmor, R. Miller, R. Phillips & M. Ortiz. Nanoindentation and Incipient Plasticity, *Journal of Materials Research*, **14**:2233-2250, 1999.
- [119] G. Smith, E. Tadmor & E. Kaxiras. Multiscale Simulation of Loading and Electrical Resistance in Silicon Nanoindentation, *Physical Review Letters*, **84**(6):1260-1263, 2000.
- [120] R. Miller, E. Tadmor, R. Phillips & M. Ortiz. Quasicontinuum Simulation of Fracture at the Atomic Scale, *Modelling and Simulation in Materials Science and Engineering*, **6**:607-638, 1998.
- [121] J. Yang & X. Li. Comparative Study of Boundary Conditions for Molecular Dynamics Simulations of Solids at Low Temperature, *Physical Review B*, **73**(22):224111, 2006.
- [122] C. Kane, J. Marsden, M. Ortiz & M. West. Variational Integrators and the Newmark Algorithm for Conservative and Dissipative Mechanical Systems, *International Journal for Numerical Methods in Engineering*, **49**(10):1295-1325, 2000.

- [123] A. Lew, J. Marsden, M. Ortiz & M. West. Asynchronous Variational Integrators, *Archive for Rational Mechanics and Analysis*, **167**(2):85-146, 2003.
- [124] A. Berger, S. Ockers & R. Siegel. Measurement of the Monovacancy Formation Enthalpy in Copper, *Journal of Physics F: Metal Physics*, **9**(6):1023-1033, 1979.
- [125] T. Hehenkamp, W. Berger, J. Kluin, C. Ludecke & J. Wolff. Equilibrium Vacancy Concentration in Copper investigated with the Absolute Technique, *Physical Review B*, **45**(5):1998-2003, 1992.
- [126] A. Nieves, V. Vitek & T. Sinno. Atomistic Analysis of Phase Segregation Patterning in Binary Thin Films Under Applied Mechanical Fields, *Journal of Applied Physics*, **107**:054303, 2010.
- [127] F. Leroy, G. Renaud, A. Letoublon, R. Lazzari, C. Mottet & J. Goniakowski. Self-Organized Growth of Nanoparticles on a Surface Patterned by a Buried Dislocation Network, *Physical Review Letters*, **95**:185501, 2005.
- [128] D. Stevens & G. Powell. Diffusion-Induced Stress and Plastic Deformation, *Metallurgical and Materials Transactions A*, **8**:1531-1541, 1977.
- [129] I. Daruka, I. Szabo, D. Beke, C. Cserhati, A. Kodentsov & F. van Loo. Diffusion-induced Bending of Thin Sheet Couples: Theory and Experiments in Ti-Zr System, *Acta Materialia*, **44**:4981-4993, 1996.